

ABSTRACT

PIEZOCERAMIC ACTUATOR PLACEMENT FOR ACOUSTIC CONTROL OF PANELS

Jeffrey S. Bevan
Old Dominion University, 2000
Director: Dr. Chuh Mei

Optimum placement of multiple traditional piezoceramic actuators is determined for active structural acoustic control of flat panels. The structural acoustic response is determined using acoustic radiation filters and structural surface vibration characteristics. Linear Quadratic Regulator (LQR) control is utilized to determine the optimum state feedback gain for active structural acoustic control. The optimum actuator location is determined by minimizing the structural acoustic radiated noise using a modified genetic algorithm. Experimental tests are conducted and compared to analytical results.

Anisotropic piezoceramic actuators exhibit enhanced performance when compared to traditional isotropic piezoceramic actuators. As a result of the inherent isotropy, these advanced actuators develop strain along the principal material axis. The orientation of anisotropic actuators is investigated on the effect of structural vibration and acoustic control of curved and flat panels. A fully coupled shallow shell finite element formulation is developed to include anisotropic piezoceramic actuators for shell structures.

FOREWORD

The research results presented herein fulfill the requirements of NASA research grant NAG-1-2141, entitled “Experimental and Numerical Analysis of Structural Acoustic Control for Interior Noise Reduction.” The research results contained herein constitute a dissertation prepared by Jeffrey S. Bevan under the guidance of Professor Chuh Mei of the OLD Dominion University, Department of Aerospace Engineering. The technical monitor is Mr. Travis L. Turner of NASA Langley Research Center, Structural Acoustic Branch.

ACKNOWLEDGMENTS

I would like to extend my sincere gratitude and appreciation to my advisor Professor Chuh Mei and dissertation committee members Professors Thomas E. Alberts, Donald L. Kunz, Brett A. Newman, and Dr. Gary P. Gibbs for providing invaluable assistance and guidance. Special thanks are extended to PCB Piezotronics, Inc. and Mr. Lou Zagst for supplying instrumentation to support the experimental test. I would like to thank Dr. Richard J. Silcox and Mr. Travis L. Turner of NASA Langley Research Center for their support pursuant to NAG1-2141. Special thanks go to Dr. Randolph H Cabel of NASA Langley Research Center for his invaluable assistance and support in developing the DSP data acquisition system. In addition, special thanks go to Mr. David Chestnut and Ms. Rita Aguillard of the Virginia Consortium of Engineering Science Universities for providing an environment to facilitate quality research. I am grateful for the support and assistance provide by Mr. Jay Moen and Mr. Carlton Pike of NASA Langley Research Center and Mr. Donald E. Brown of Lockheed Martin Engineering.

TABLE OF CONTENTS

	Page
LIST OF TABLES	vii
LIST OF FIGURES	viii
NOMENCLATURE	xii
 Chapter	
I. INTRODUCTION	1
Background	1
Literature Survey	2
Outline	8
II. PIEZOELECTRICITY	10
Introduction	10
Piezoelectricity and Electric Polarization	10
Piezoceramics	17
Anisotropic Piezoceramics	18
III. FINITE ELEMENT FORMULATION	25
Introduction	25
Element Displacement Functions	25
Strain Displacement Functions	29
Constitutive Relations	32
Force and Moment Resultant	33
Equations of Motion	34
Global Equations of Motion	43

Finite Element Validation	45
Numerical Example of a Curved Panel with MFC	46
IV. STRUCTURAL ACOUSTICS.....	53
Introduction	53
Acoustic Radiation Filters	55
Planar Radiation Resistance	59
Curved Panel Radiation Operator	60
V. FEEDBACK CONTROL AND PIEZOCERAMIC ACTUATOR	
PLACEMENT	69
Introduction	69
Finite Element State-Space Representation	69
Radiation Filter State-Space Representation	70
Structural Acoustic State-Space Representation	72
Genetic Algorithm Optimization.....	74
VI. EXPERIMENTAL AND NUMERICAL RESULTS.....	80
Introduction	80
Data Acquisition and Control.....	83
Experimental Results	85
Analytical Results.....	91
VII. CONCLUSIONS	100
REFERENCES.....	105
APPENDICES.....	110
A. APPENDIX	110

MFC Structural Acoustic Simulation.....	110
Introduction	110
Curved Panel Simulation.....	110
Flat Panel Simulation	118
B. APPENDIX	124
Test Instrumentation.....	124

LIST OF TABLES

Table	Page
3.1 Finite Element Convergence	45
3.2 Piezoceramic Properties	47
6.1 Open and Closed Loop Sound Power Attenuation	89
6.2 Open and Close Loop Predicted Sound Power Attenuation	92
6.3 Piezoelectric Modal Participation	99
B.1 Accelerometer List	124
B.2 Microphone List	124

LIST OF FIGURES

Figure	Page
2.1 Parallel Plate Capacitor	11
2.2 Parallel Plate Capacitor with Dielectric	12
2.3 Effective Electric Field.....	14
2.4 Electric Polarization Hysteresis	15
2.5 Traditional Piezoceramic Wafer.....	17
2.6 AFC Package.....	19
2.7 MFC Transducer	19
2.8 Equivalent MFC Interdigital Electrode Model.....	20
2.9 Electric Field Potential Gradient.....	22
2.10 Non-uniform Electric Field Distribution of MFC	23
2.11 Principal and Global Coordinate Relation	24
3.1 Shell Element Geometry	26
3.2 Element Area Coordinates	28
3.3 Shell Curvature Geometry.....	31
3.4 MFC Finite Element Mesh.....	46
3.5 MFC Curved Finite Element Mesh	47
3.6 MFC and PZT for 5°	48
3.7 MFC and PZT for 15°	49
3.8 MFC and PZT for 25°	49
3.9 MFC and PZT for 35°	50
3.10 MFC and PZT for 45°	50

3.11	MFC and PZT for 55^0	51
3.12	MFC and PZT for 65^0	51
3.13	MFC and PZT for 75^0	52
4.1	Vibrating Surface Geometry	61
4.2	Curved Panel Finite Element Geometry.....	64
4.3	Curved Panel Using Triangular Acoustic Radiators	65
4.4	Flat Panel Using Triangular Acoustic Radiators.....	66
4.5	Flat Panel Using Rectangular Acoustic Radiators	66
4.6	Curved Panel With Triangular Acoustic Radiators.....	67
4.7	Flat Panel With Triangular Acoustic Radiators	68
5.1	Approximate and Exact Radiation Efficiency.....	71
5.2	Genetic Algorithm Output.....	77
5.3	GA Actuator Placement	78
5.4	Refined Optimum Actuator Locations	79
6.1	STL Instrumentation Layout	81
6.2	Source and Receiving Room Sound Power.....	82
6.3	Accelerometer Locations.....	84
6.4	Panel A Actuator Placement	86
6.5	Panel B Actuator Placement.....	86
6.6	Panel C Actuator Placement.....	87
6.7	Open and Closed Loop Performance of Panel A	90
6.8	Open and Closed Loop Performance of Panel B.....	90
6.9	Open and Closed Loop Performance of Panel C.....	91

6.10	Panel A Singular Values	93
6.11	Panel B Singular Values.....	93
6.12	Panel C Singular Values.....	94
6.13	Uniform Random Simulation Acoustic Disturbance PSD	95
6.14	Predicted Open and Closed Loop Radiated Power for Panel B	96
6.15	Predicted Open and Closed Loop Radiated Power for Panel C	96
6.16	Revised Optimum Actuator Locations.....	97
6.17	Predicted Open and Closed Loop Radiated Power for the Revised Optimum Panel	98
A.1	Predicted Open and Closed Loop Radiate Power for 20° MFC	111
A.2	Predicted Open and Closed Loop Radiate Power for 20° PZT	112
A.3	Predicted Open and Closed Loop Radiate Power for 35° MFC	112
A.4	Predicted Open and Closed Loop Radiate Power for 35° PZT	113
A.5	Predicted Open and Closed Loop Radiate Power for 45° MFC	113
A.6	Predicted Open and Closed Loop Radiate Power for 45° PZT	114
A.7	Predicted Open and Closed Loop Radiate Power for 50° MFC	115
A.8	Predicted Open and Closed Loop Radiate Power for 50° PZT	115
A.9	Predicted Open and Closed Loop Radiate Power for 60° MFC	116
A.10	Predicted Open and Closed Loop Radiate Power for 60° PZT	116
A.11	Predicted Open and Closed Loop Radiate Power for 70° MFC	117
A.12	Predicted Open and Closed Loop Radiate Power for 70° PZT	117
A.13	Panel B MFC Orientation.....	119
A.14	Panel E MFC Orientation.....	119

A.15	Open and Closed Loop Sound Power of Panel B with MFC	120
A.16	Open and Closed Loop Sound Power of Panel B with PZT	121
A.17	Open and Closed Loop Sound Power of Panel E with MFC	122
A.18	Open and Closed Loop Sound Power of Panel E with PZT.....	122

NOMENCLATURE

A	area, (m^2)
a_i	elemental acoustic radiator area, (m^2)
$[A],[B],[D]$	extension, coupling, and bending stiffness matrices, ($\text{Pa}\cdot\text{m}$, $\text{Pa}\cdot\text{m}^2$, $\text{Pa}\cdot\text{m}^3$)
$[A_s]$	shear stiffness matrix
$[\mathcal{A}],[\mathcal{B}],$ $[C],[D]$	structural state-space matrices
$[A_f],[B_f],$ $[C_f],[D_f]$	radiation filter state-space matrices
$[\bar{D}_f]$	modal radiation filter state-space matrix
$[\bar{B}_f]$	modal radiation filter state-space feedback matrix
$[B_\phi]$	electric field distance, (m^{-1})
C	electric capacity, (Farad)
c	speed of sound, (m/s)
$[C_i]$	strain interpolation matrices
$[c]$	element structural damping matrix, (kg/s)
\mathcal{D}_i	electric displacement density, ($\text{Coulomb}/\text{m}^2$)
D_{ij}	dipole coefficients, ($\text{kg}/\text{m}^2\cdot\text{s}$)
d_{ij}	piezoelectric coefficients, (m/Volt)
\mathcal{E}_i	electric field, (Volt/m)

E_i	Young's Modulus, (Pa)
$\{F_i\}$	body force or surface traction, (N, N/m ²)
G_y	shear modulus, (Pa)
$[G]$	shear lamina stiffness, (N/m)
$[H_i]$	displacement interpolation functions
h_o	initial shell deformation, (m)
h_i	piezoceramic thickness, (m)
I	acoustic intensity, (W/m ²)
j	imaginary operator
J_{rad}	acoustic radiated power cost function
J	linear quadratic state-based cost function
k	acoustic wavenumber, (rad/m)
$[K], [k]$	system and element stiffness matrices, (N/m)
\mathcal{L}	acoustic radiator length, (m)
Li, M_i	quadratic interpolation polynomials
$[M], [m]$	system and element mass matrices, (Kg)
M_y	monopole coefficients, (kg/m ² -s)
$\{N\}$	force resultant, (force per unit length)
$\{M\}$	moment resultant, (moment per unit length)
$\{N_\phi\}, \{M_\phi\}$	electric force and moment resultant, (N/m, N)
\mathcal{P}	electric polarization, (Coulomb/m ²)

P	acoustic power, (W)
p	acoustic pressure, (Pa)
$\{p_i\}$	element nodal loading, (N)
$\{P_i\}$	global nodal load, (N)
$[Q]$	lamina reduced stiffness matrix, (N/m ²)
\mathcal{Q}	electric surface charge, (Coulombs/m ²)
$[Q]$	state weighting matrix
q	total charge, (Coulombs)
q_r	r^{th} modal coordinate
\bar{r}	acoustic pressure vector, (m)
$\{r\}$	radiation state vector
\bar{R}_o	acoustic receiver vector, (m)
$\{R\}$	shear stress resultant, (force per unit length)
S	total acoustic radiating area, (m ²)
T	kinetic energy, (kg-m/s ²)
U	strain energy, (N-m)
$\{u\}$	input actuator vector
V	electric voltage, (Volts)
∇	volume, (m ³)
u, v	membrane displacement, (m)
W	external work, (N-m)
w	transverse displacement, (m)

$\{w\}$	nodal DOF
$\{w_b\}$	transverse nodal DOF, (m)
$\{w_m\}$	membrane nodal DOF, (m)
$\{w_\phi\}$	electrical nodal DOF, (V)
$\{x\}$	state vector
x, y, z	cartesian coordinates
Z	acoustic transfer impedance, (kg/(m ⁴ s))
Greek Symbols	
α	orientation angle, (degrees)
δ	dipole separation, (m)
ε	strain
$\{\varphi\}$	mode shape
$\{\varepsilon\}$	total strain vector
$\epsilon, \epsilon_o, \epsilon_r$	dielectric permittivity, (Farad/m)
ϵ_o	dielectric permittivity of free space, (Farad/m)
ϵ_r	relative dielectric permittivity
κ	curvature, (1/m)
γ	shear strain
γ_{ij}	angle between acoustic radiator elements, (degrees)
μ	dipole moment, (N-m)

$\{\theta\}$	nodal rotational DOF
τ	shear stress, (N/m ²)
ν_{ij}	Poisson's ratio
$\{v\}$	normal surface velocity, (m/s)
σ	stress, (N/m ²)
$\hat{\sigma}$	acoustic impedance, (kg/m ² -s)
ω	circular frequency, (rad/s)
ω_r	r^{th} natural frequency, (rad/s)
ρ	equivalent mass density per length, (kg/m ²)
ρ_o	acoustic fluid density, (kg/m ³)
θ_x, θ_y	rotation about x and y axis
ξ_i	natural coordinates
$[\psi]$	approximate radiation efficiency, (kg-m ² /s ²)
$[\Phi]$	normal structural mode shape matrix
$[\hat{\Phi}]$	interpolated structural mode shape matrix
χ	dielectric susceptibility
ζ	damping ratio

CHAPTER I

INTRODUCTION

Background

The primary objective of this research is to determine the optimum placement of traditional piezoceramic actuators to minimize acoustical radiated noise of vibrating flat rectangular panels utilizing active structural acoustic control (ASAC). However, this research is based, in part, on contributing to the reduction of interior noise of subsonic aircraft. Therefore, secondary research objectives include active vibration and acoustic control of curved panels, radiation filters for curved panels, and advanced actuator concepts based on anisotropic piezoceramic materials. However, active structural acoustic control using anisotropic piezoceramic has not been addressed in the literature. Therefore, this research develops a coupled finite element shell formulation to evaluate the performance of anisotropic piezoceramic actuators for structural acoustic and vibration control of curved panels.

Structurally radiated noise of a flat rectangular panel is dominated by the first structural vibration mode which inherently possesses poor coupling to piezoceramic actuators. Therefore, to achieve the maximum benefit of ASAC, optimum piezoceramic actuator locations becomes an important factor. Pursuing this objective entails a multi-disciplinary approach encompassing several aspects of active control of structural vibrations and structure-borne radiated noise of flat and curved panels. To this end, items investigated include incorporating advanced anisotropic piezoceramic transducers, development of a coupled mixed field finite element formulation of a triangular shallow

The journal model used for this dissertation is *AIAA Journal*.

shell element with integral piezoceramic material, development of structural acoustic radiation filter design for curved panels, and implementation of a genetic algorithm to determine ideal locations of multiple piezoceramic actuators.

Literature Survey

Anisotropic piezoceramic transducers recently appeared in the literature as a method of increasing the overall actuator performance of piezoceramic material.¹ Furthermore, the anisotropic design also provides convenient twist actuation control of structures not obtainable with traditional isotropic piezoceramic.² The research in the literature primarily investigates design and manufacturing aspects of active-fiber composites (AFC) and macro-fiber composites (MFC) targeting maximum performance. However, applications of AFC and MFC found in the literature have been limited to global torsional control of structures utilizing placement of the actuators.² Smart structure technology utilizing AFC or MFC concepts for active vibration control (AVC) and active structural acoustic control (ASAC) have not been investigated in the literature. The general anisotropy of polyvinylidene fluoride (PVF2) was considered for active control of plates by Miller *et al*;³ however, his solution relies on classical plate theory and the coupled charge equation developed by Lee⁴, thereby requiring knowledge of the displacement field of the PVF2 lamina.

The objective of this research is to provide methodologies for transducer placement for smart structures during the design stage for ASAC implementation. ASAC requires a robust and accurate structural dynamic plant model suitable for candidate control strategy that may be applied. If a physical structure exists, system identification is often performed to estimate the structural dynamic characteristics, which supports

physical realization of the control implementation. Typically, however, the physical structure does not exist during the design stage; hence, the finite element method affords an efficient and flexible approach to obtain a structural dynamic plant model. The finite element model can also readily support additional structural modifications and subsequent plant dynamics.

Many finite element formulations incorporating the piezoelectric effect appear in the literature since its introduction in 1970.⁵ Initial modeling of piezoceramic structures utilized hexahedral (solid) finite elements thereby treating the piezoceramic as a complete structure in and of itself. Tzou describes this approach in great detail for plates, shells, and spherical geometries.⁶ Given the computational effort and modeling difficulties of implementing hexahedral elements for smart structures, where piezoceramic transducers represent a relatively small portion of the structure, Tseng introduced Guyan reduction to reduce the total degrees of freedom (DOF) of a solid piezoceramic element.⁷ Hwang and Park⁸ developed a modified piezoelectric plate element with one electric DOF per element further increasing computational efficiency. A modified, high precision composite, fully coupled rectangular plate element was used by Zhou⁹ to suppress nonlinear panel flutter using piezoceramic transducers. The same element was further developed and experimentally validated by Bevan¹⁰ to include piezoelectric coupling due to moderately large structural displacements.

Researchers successfully applied finite element analysis of smart structures with piezoceramic transducers for flat surfaces, though literature results for curved or shell structures remain limited in number. Tzou and Ye developed a laminated quadratic C^0 piezo-elastic six-node triangular shell finite element.¹¹ This formulation, based on a

layerwise constant shear angle theory, applies to shell structures in which the piezoceramic lamina remains continuous and not segmented. Tzou *et al.* investigates segmented piezoceramic transducers applied to laminated cylindrical shells; however, this formulation is based on piezo-elastic shell lamination theory.¹² Saravanos developed a new theory for piezoelectric laminates that combines linear displacement fields through the thickness of the laminate for inplane displacements with layer-wise electric potential field through the laminate.¹³ By combining, or mixing, layer-wise potential and first-order shear theory, Saravanos accurately and efficiently models both thin and moderately thick laminated piezoelectric shells. However, since Saravanos uses an eight-node element with bi-quadratic shape functions, this element will not support the anisotropic requirements of arbitrarily placement of AFC or MFC transducers on a curved panel.

Since this research is concerned with the reduction of acoustic radiation of vibrating structures, the physics of the radiated acoustic field must also be modeled. Sound and structural vibration encompasses a broad and complex discipline. In general, the vibrating structure and surrounding medium behave as a coupled system. More specifically, the properties of the surrounding medium can affect the dynamic behavior of the structure by adding mass, damping, and stiffness. Furthermore, the audible sound spectrum perceivable by humans extends from 20 Hz to 20 kHz, which corresponds to acoustic wavelengths in air from 17 m to 17 mm respectively. Hence, the physical dimensions of the corresponding structural system dictates the choice of the mathematical model used to characterize the associated acoustics, since resonances occur when dynamic wavelengths and physical structural dimensions coincide. For example, if the

structural dimensions are much less than the maximum acoustic wavelength, then it is common to use approximations that greatly simplify the governing equations.

Another geometric consideration when formulating the structural acoustic problem entails modeling of the prescribed radiation field. For example, radiation into free space requires a different model than radiation within an enclosed volume. This research considers the free space, far field radiation of a vibrating structure for frequencies no greater than 500 Hz.

To characterize the corresponding acoustic radiation of a vibrating structure, this research utilizes the concept of acoustic radiation filters. The radiation filter provides an estimate of radiated acoustic power derived from structural vibration characteristics such as discrete surface velocities. The modal approach, or spatial filtering, for analysis of exterior radiation problems have been recently developed by Borgiotti,^{14,15,16} Photiadis,¹⁷ Sarkissian,¹⁸ Cunefare,^{19,20,21} Cunefare and Currey,²² and Elliott and Johnson.⁴⁹ This approach exploits the inherent structural modal interaction that produces the acoustic radiation. Researchers have determined that the structural vibration modes do not radiate independently; in fact, a strong coupling exists between the structural vibration modes and the radiated acoustic field. Due to this strong dependence, it is possible to reduce the vibration of a dominant vibration mode while having little or no effect on the overall radiated sound. Formulation of the radiation filter requires a radiation operator dependent on frequency and structural geometry. The radiation operator characterizes the coupling of structural and acoustic modes and can be derived to incorporate desired pertinent acoustic properties. For example, a radiation operator for three-dimensional structures requires the use of Helmholtz integral while for planar structures the use of

Rayleigh's integral is required to develop a radiation operator. Researchers have applied several techniques to extract radiation information from the radiation operator including singular value decomposition¹⁴ and wave-vector filtering.¹⁷ Eigenvalue decomposition of the radiation, or coupling operator, yields a set of frequency dependent orthogonal eigenvectors, which represent acoustic radiation modes and corresponding eigenvalues proportional to their radiation efficiencies. The acoustic radiation modes should not be confused with either structural vibration modes or acoustic modes of enclosed volumes. The radiation modes can be considered as orthogonal basis functions spanning the radiation domain space. The associated radiation efficiencies provide a means of ranking the dominant radiation modes, thus indicating significant offending radiation modes that can be targeted utilizing ASAC for noise reduction.

Baumann *et al.*²³ implemented linear quadratic regulator (LQR) feedback control to minimize the radiated power of a vibrating beam by augmenting the state space system with radiation filters. Hence, he achieved structural acoustic control by targeting offending radiation modes for the vibrating beam. Recently, Gibbs *et al.*²⁴ developed the radiation modal expansion (RME) method to efficiently approximate radiation filters for real time digital signal processing applications.

As previously discussed the objective of this research involves determining the best piezoceramic actuator locations for the reduction of radiated noise during the design process of a typical smart structure. Not only does the finite element method provide accuracy and modeling flexibility, it also provides element nodal sensor information that can be utilized in full state feedback control. One disadvantage of full state feedback control is that all states must be available. Due to physical constraints and practical

limitations on the number of sensors available, full state feedback may not be achievable for real structures. In practice, this leads to implementing state estimators, which provides the requisite feedback information. Furthermore, real control applications contain inherent noise contamination from sensors that limit control performance. In effect, the controller is unable to distinguish between erroneous noise and the desired sensor signal. One application used frequently for reasonable modal density is the linear quadratic gaussian (LQG) control law, which includes a state estimator and exogenous noise contribution to both sensors and actuators. Implementing LQR requires full state feedback and provides optimal gains that prescribe an upper bound, or limit, to achievable performance.²⁵ Thus, this research implements LQR control to determine the best location of piezoceramic actuators to achieve the theoretical upper limit of ASAC performance. Furthermore, since prediction of the absolute noise reduction is not an objective, the optimum actuator locations are validated by experiments and compared to the upper bound predictions.

Piezoceramic actuator placement is determined by prescribing an actuator size that is commonly available and applying a genetic algorithm based search method to evaluate the best locations. The goal of this research is not to develop an optimization method but to implement a proven method. The genetic algorithm (GA), or evolutionary algorithm (EA), is a search method derived from the mechanics of natural selection and genetics. The algorithm is a structured random search method utilizing survival of the fittest information of previous iterations. Hence, they exploit historic information to speculate on potential search points. Salient GA characteristics that distinguish them from traditional optimization techniques include²⁶

- GAs work with a coding of the parameter set, not the parameters themselves.
- GAs search from a population of points, not a single point.
- GAs use payoff (objective function) information, not derivatives or other auxiliary knowledge.
- GAs use probabilistic transition rules, not deterministic rules.

Many optimization problems have been successfully solved using the GA. Ryou *et al.*²⁷ determined the piezoelectric electrode shape for modal control of a cantilevered beam using a genetic algorithm. Simpson and Hansen²⁸ implemented GA to determine optimum actuator locations for active noise control (ANC) for enclosed spaces. Yao *et al.* implemented GA to determine sensor locations of large space structures for modal identification.²⁹ Tsao³⁰ determined sacrificial anode locations for optimum cathodic protection of submerged structures using the GA. The above references indicate research that is closely related to the work described herein, thereby demonstrating the ability of GA to be applied to this current research.

The GA was selected since the literature demonstrated its ability to successfully handle similar optimization problems and that it is applicable to many problems with little or no modifications. This research utilizes the reduction in overall structural radiated power as the GA performance index, or cost function, to search for the optimum actuator locations. The LQR feedback control determines the theoretical maximum achievable reduction in sound power for the given actuator location.

Outline

Considerable research for each of the individual topics discussed herein can be found in the literature, so this research applies a multi-disciplinary approach to achieve maximum benefits of ASAC from optimum piezoceramic transducer placement. This dissertation is organized as follows. Chapter II introduces the piezoceramic phenomena

including anisotropic piezoceramics. Chapter III presents a triangular shell finite element formulation that includes anisotropic piezoceramic lamina. An effort has been made to develop a generalized formulation to handle arbitrary double curved shallow shell geometry applicable to laminated composites. Chapter IV pertains to structural acoustics aspects using the radiation filter concept, including the formulation of radiation filters for curved panels. The resulting radiation filters are amenable to ASAC methodologies. Chapter V discusses feedback control and genetic algorithm optimization techniques. Combining finite element analysis, acoustic radiation filters, LQR feedback control, and a genetic algorithm yields a complete analytical model. Chapter VI discusses experimental test results compared to numerical analysis for actuator placement. Several test panels with various actuator locations are tested and modeled and their results are compared. The test panels are subjected to an acoustic disturbance and the acoustic reduction of acoustic radiated noise is used as a measure of actuator performance. Chapter VII provides concluding remarks and future recommendations.

CHAPTER II

PIEZOELECTRICITY

Introduction

The phenomena of piezoelectricity describes a material that generates electrical charge due to applied mechanical stress or conversely, one that undergoes deformation due to an induced strain when subjected to an external electric field. Literature indicates that researchers have studied piezoelectric materials since their discovery by Pierre and Jacques Curie circa 1880. The piezoelectric discovery directly resulted from Pierre Curie's research between crystal symmetry and so-called pyroelectricity.³¹ The term piezoelectricity, proposed by Hankel, describes the well-known interaction between electrical and mechanical systems.

Piezoelectricity and Electric Polarization

To understand piezoelectricity, first consider the concept of dielectric polarization. A dielectric, or insulator, describes a material that does not support electrical conduction and restricts or completely impedes charge motion within the material when subjected to an external electric field. This class of materials is in contrast to electrical conductors where charges migrate freely when exposed to a similar electric field yielding electric current. An important distinction between these two materials is the presence of an internal electric field within the dielectric and the absence of an electric field within the conductor. The presence of this internal electric field results in an electrical polarization of the dielectric. The phenomenon of polarization describes the net, or macroscopic, electric field resulting from deformed, or altered, microscopic

electric fields of individual atoms or molecules. The linear artificial dielectric model helps illustrate the polarization phenomena.

Before examining dielectrics a review of free space electrostatics is beneficial.

Figure 2.1 shows two parallel conductors in free space with a constant voltage source.

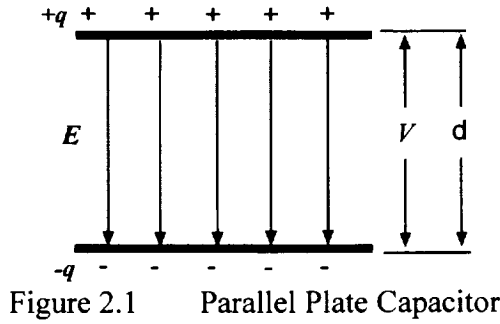


Figure 2.1 Parallel Plate Capacitor

The electric field between the conductors is simply

$$\mathcal{E} = \frac{V}{d} \quad (2.1)$$

The total charge on the upper conductor, obtained from Gauss' law, is

$$q = \int_A \mathcal{D} dA = \epsilon_0 \mathcal{E} A \quad (2.2)$$

The capacitance describes a linear relation between the charge and voltage as

$$q = \frac{\epsilon_0 A}{d} V \equiv CV \quad (2.3)$$

where ϵ_0 is the free space permittivity. In terms of field quantities, a linear constitutive relation is defined for the electric flux density as

$$\mathcal{D} = \epsilon_0 \mathcal{E} \quad (2.4)$$

These relations are restricted to free space, and if any other dielectric material is placed between the conductors both the charge and field will differ from the above results.

For example, inserting a dielectric material between the conductors as shown in Figure 2.2 produces interesting results.

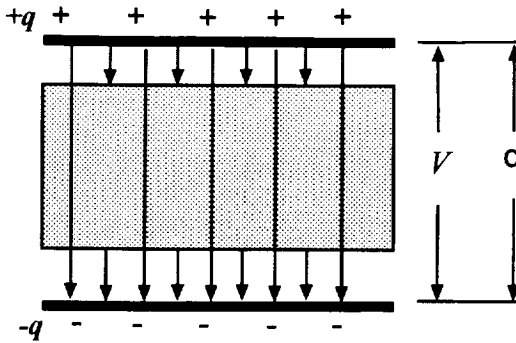


Figure 2.2 Parallel Plate Capacitor with Dielectric

The charge per unit area of the conductors in free space becomes

$$Q = \frac{q}{A} = \epsilon_0 \frac{V}{d} \quad (2.5)$$

While maintaining a constant voltage the surface charge increases due to the inclusion of the dielectric and becomes

$$Q' = \epsilon_0 \epsilon_r \frac{V}{d} \quad (2.6)$$

Thus, the increase in charge due to polarization becomes

$$\begin{aligned} P &= Q' - Q \\ &= \epsilon_0 \epsilon_r \frac{V}{d} - \epsilon_0 \frac{V}{d} \end{aligned} \quad (2.7)$$

resulting in the following normalized charge distribution

$$\mathcal{D} = \epsilon_0 \mathcal{E} + \mathcal{P} \quad (2.8)$$

where

$$\begin{aligned} \mathcal{P} &= \epsilon_0 (\epsilon_r - 1) \mathcal{E} \\ &= \epsilon_0 \chi \mathcal{E} \end{aligned} \quad (2.9)$$

and the dielectric susceptibility is defined as $\chi = \epsilon_r - 1$.

The electromagnetic constitutive relation indicated in Eq. (2.4) is applicable to free-space only. However, substituting Eq. (2.9) into Eq.(2.8), yields the following linear dielectric constitutive relation

$$\mathcal{D} = \epsilon \mathcal{E} \quad (2.10)$$

where the dielectric permittivity is defined as $\epsilon = \epsilon_0 \epsilon_r$, ϵ_r denotes the relative permittivity of the material and describes the charge storage capability of the material through polarization.

Linear dielectric polarization characterized by electromagnetic field theory as described above, is based on macroscopic observations and does not provide any insight to the mechanism responsible for the polarization. Further insight to polarization necessitates a microscopic approach at the molecular, or atomic level. Specifically, atomic reaction external electric fields must be examined. Atoms have a positive charged nucleus surrounded by a cloud of electrons that statistically remain electrically neutral. When an atom is subjected to an electric field the equilibrium charge distribution is shifted resulting in a dipole moment as

$$\mu = q\delta \quad (2.11)$$

where q is the total charge and δ is the separation distance. Since the centroid of electron charge volume moves a distance δ , the total charge volume becomes $S\delta$ for area S . The surface charge per unit area of the macroscopic dielectric becomes

$$\mathcal{Q} = Nq\delta \quad (2.12)$$

for N molecules per unit volume. Substituting Eq.(2.11) into Eq.(2.12) yields

$$\mathcal{Q} = N\mu \quad (2.13)$$

which describes the polarized surface charge density and is equivalent to \mathcal{P} derived under the macroscopic electromagnetic field theory.

The macroscopic theory identifies the external field sufficiently for analysis; however, it is unable to characterize the internal, or effective, field behavior. To examine the internal field of a polarized dielectric in a uniform field, a simplified method used by Lorentz is very useful.³² Consider an infinitesimal volume described by surface A within the dielectric shown in Figure 2.3.

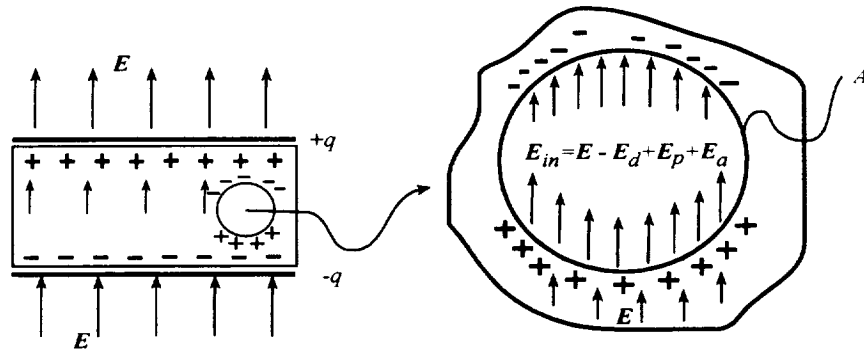


Figure 2.3 Effective Electric Field

The dielectric external to A is considered as a continuum while inside A is assumed to be on an atomic scale. The internal field can be expressed as the sum of the following fields:

$$\mathcal{E}_{in} = \mathcal{E} - \mathcal{E}_d + \mathcal{E}_p + \mathcal{E}_a \quad (2.14)$$

where \mathcal{E} is the external field, \mathcal{E}_d the depolarizing field on the external surface of the dielectric, \mathcal{E}_p the polarizing field of the charges on surface A , and \mathcal{E}_a is the field of the dipoles enclosed in surface A . The internal field is a manifestation of the interaction of physical lattice structure of the material and will be discussed subsequently. Although internal fields cannot be readily measured, they are important for understanding nonlinear

ferroelectric behavior. The internal and total field effects of piezoelectric materials were investigated by Main *et al.* to develop high precision position actuators.³³

Dielectric polarization results from the formation of dipoles, however various mechanism are responsible for several types of polarization. Electronic polarization results from the formation of dipoles due to an electron cloud. Molecular polarization stems from dipoles resulting from the deformation of ionic molecular bonds. Polar fluids exhibit orientational polarization when the polar molecules align in a field.

Dielectrics exhibiting spontaneous electric polarization are categorized as pyroelectric. The term 'spontaneous' implies polarization exist in the absence of an external field and is sometimes called remnant polarization. Furthermore, linear polarization theory fails to describe materials that exhibit hysteresis between the electric field (E) and the electric flux density (D), as shown in Figure 2.4, which are referred to as ferroelectric materials in the literature.

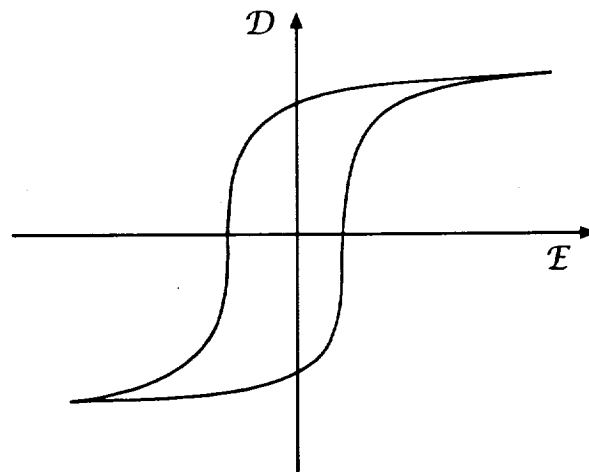


Figure 2.4 Electric Polarization Hysteresis

All ferroelectric material exhibits this nonlinear behavior and most dielectrics are ferroelectric. However, in solving field problems small variations about a quiescent point

suffices, thus any point on the hysteresis loop can be assumed linear.³⁴ A ferroelectric material refers to a sub-class of pyroelectrics and is characterized by their mobility of the spontaneous electric polarization. Hence, the physical direction of the polarization can be manipulated, or oriented, by applying an external field of sufficient strength. Since ferroelectric is a sub-class of pyroelectric they also follow temperature dependency. The most significant of which is a temperature where polarization ceases and the material is said to be paraelectric. The Curie point defines the temperature at which the spontaneous polarization ceases.

Piezoelectric is a sub-class of ferroelectric and is characterized by deformation yielding a change in polarization. Hence, piezoelectric material is a ferroelectric characterized by an electric polarization that can be altered by an external field of sufficient strength. Furthermore, they also possess temperature dependant properties. Hence, piezoelectric materials can be manufactured using ferroelectric ceramics and their polarization can be manipulated through poling. The poling process establishes the ferroelectric axis by aligning the dipoles between electrodes that apply a field of sufficient strength. It is common that during the manufacturing process of advanced transducers the piezoceramic may be exposed to temperatures exceeding the Curie point thus destroying any polarization. However, the specimen can be re-poled to create the desired polarization. The piezoelectric phenomenon is observed in many materials such as natural quartz and Rochelle salt, polycrystalline ceramic, and semi-crystalline polymer.

Piezoceramics

Piezoelectric crystals proved ideal for certain transducer designs and discrete circuit devices operating in both on and off resonant conditions. However, crystallography dictates the polarization axes and thus limits selected applications. These restrictions are greatly relaxed due to manufacturing of piezoceramic. The manufacturing process for piezoceramic consists of combining a mixture of oxides with a binder that can be formed into the desired geometric shape. For example, readily available piezoceramic devices include planar monolithic wafers, disks, rings, rods, and shells. This “green” specimen is then sintered, yielding a polycrystalline ceramic with inter-granular bonds sufficient to facilitate the polling process.

The most common piezoceramic shape utilized in smart structure technology is the thin planar monolithic wafer shown in Figure 2.5.

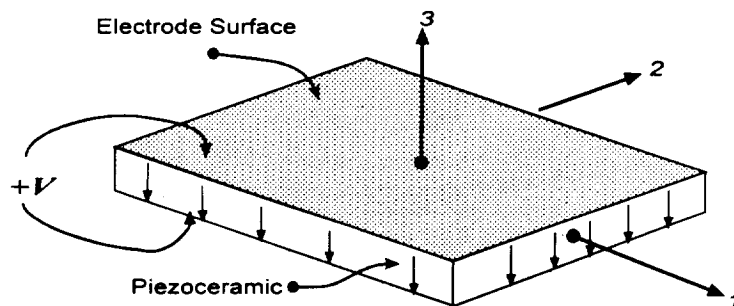


Figure 2.5 Traditional Piezoceramic Wafer

The planar surface area consists of plated electrodes that facilitate uniform poling through the piezoceramic thickness. The poling process establishes domain structure realignment resulting in the prescribed piezoelectric effect. The resulting wafer exhibits plane strain when subjected to an electric potential across the electrodes. Since the electrode ensures an equipotential surface and the ceramic is homogeneous in both the 1 and 2 directions

the induced strain is equal along the 1 and 2 directions. The piezoelectric charge coefficients describe the resulting induced strain, or the applied stress and the charge applied or charge generated, respectively. The piezoelectric charge coefficients for a general wafer is denoted as

$$[d] = \begin{bmatrix} 0 & 0 & 0 & 0 & d_{15} & 0 \\ 0 & 0 & 0 & d_{15} & 0 & 0 \\ d_{31} & d_{32} & d_{33} & 0 & 0 & 0 \end{bmatrix} \quad (2.15)$$

where subscript ij indicates the poling direction is along the i axis yielding strain along the j axis. For the thin monolithic wafer, $d_{31}=d_{32}$ and $d_{33}=d_{15}=0$. The piezoelectric charge constants $[d]$ describe the effectiveness of the piezoelectric performance. For example, if sensing is desirable, piezoceramics characterized by large d_{ij} constants exhibit increased sensitivity to the applied state of stress, thus generating sufficient charge to enhance the signal-to-noise ratio. Such piezoceramics are referred to as high sensitivity ‘soft’ materials and include lead zirconate titanate (PZT) -5A, -5B, and -5H among others. Conversely, high power ‘hard’ materials, such as PZT-4, -4D, and -8 can withstand substantial electrical excitation while producing large strains. Hard piezoceramics typically have smaller d_{ij} constants to maximize larger applied fields.

Anisotropic Piezoceramics

Traditional piezoceramic devices are homogeneous and isotropic resulting in a uniform electric field distribution as previously described. Recently, advanced anisotropic piezoceramic transducer concepts have appeared in the literature. For example, Active Fiber Composites (AFC) introduced by Bent and Hagood¹ and Macro Fiber Composites (MFC) introduced by Wilkie³⁵ are two such examples of anisotropic

piezoceramic materials. A typical AFC package with interdigital electrodes is shown in Figure 2.6.

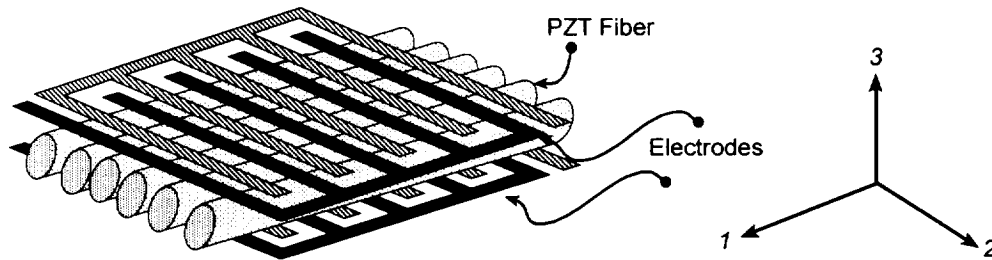


Figure 2.6 AFC Package

The MFC transducer concept is similar to the AFC transducer except that the fibers are rectangular and have a much greater cross section. For example, the AFC transducer constructed by Bent uses circular fibers with a diameter of $129\mu m$,¹ whereas the MFC transducer produced by Wilkie has rectangular fibers with a thickness $254.07\mu m$.³⁵ A typical MFC transducer is shown in Figure 2.7.

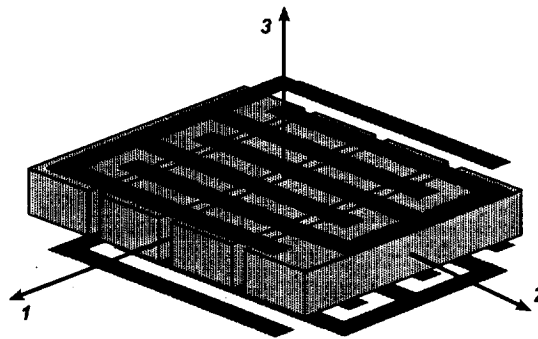


Figure 2.7 MFC Transducer

The research presented herein utilizes the MFC concept. However, the formulation presented is equally applicable to both AFC and MFC concepts. For clarity the acronym MFC will be used to describe general anisotropic piezoceramic actuators.

The obvious benefit of MFC is an additional geometric design parameter allowing actuation authority along a preferred direction. Although the MFC package resembles the

conventional monolithic wafer, the applied field delivered by the interdigital electrode is along the 1 direction as opposed to the 3 direction. The electric field established in the MFC by the interdigital electrodes yields a comparable effect of a rod with end cap electrodes characterized by the d_{33} charge constant as shown in Figure 2.8. Thus, when referring to MFC transducers, d_{11} and d_{12} are synonymous to d_{31} and d_{32} of traditional monolithic configurations.

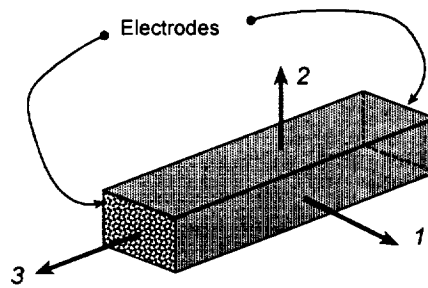


Figure 2.8 Equivalent MFC Interdigital Electrode Model

Readily available piezoceramic materials exhibit a larger piezoelectric constant if the strain and polarization axis coincide, compared to the condition when the strain is transverse to the polarization axis or applied field. Hence, traditional monolithic piezoceramic patches have inherently lower performance operating in plane strain since d_{31} is less than d_{33} . However, the MFC concept yields plane strain while exploiting the d_{33} polarization along the principal strain direction. Hence, the intrinsic benefit of the anisotropic design. Furthermore, each piezoceramic layer may have an arbitrary orientation angle producing inplane shear strains capable of inducing complex traction forces. Hence, the host structure now may experience twisting as opposed to pure

bending and membrane strain commonly associated with traditional piezoelectric actuators.

The inherent electrical and mechanical anisotropy of MFC transducers requires a more complex model than traditional PZT to accurately characterize its behavior. The difficulty arises since the applied field is no longer uniform throughout the ceramic as in the conventional monolithic wafer. The field established by the interdigital electrode is piece-wise continuous along the 1 principal direction as shown in Figure 2.6. The field non-uniformity along the 2 direction results from anisotropy characterized by matrix dielectric. For example, the fiber may be circular or rectangular, thereby producing a non-uniform field in the piezoceramic. Bent developed macroscopic property models along with detailed finite element analyses of the AFC transducer and concluded that field non-uniformity effects are negligible.³⁶ The inherent anisotropy further complicates the model since the matrix permittivity differs from that of the PZT ceramic. This dielectric mismatch can impede the applied electric field from reaching the PZT. A large dielectric mismatch can lead to a complete dielectric breakdown. This phenomenon results in a large electric field gradient producing a fault current between electrodes, thus completely diverting the electric field away from the ceramic, which renders the actuator ineffective. This effect was observed mainly when the matrix was doped to enhance dielectric performance. Recently, Janos and Hagood achieved improved dielectric performance by including magnetic particles within the matrix.³⁷

Furthermore, the geometry of the MFC device provides some interesting observations. Recall that traditional piezoceramics maintained isotropy and a uniform electric field, which followed the linear piezoelectric theory.³⁸ The first feature of the

MFC concept is the electric field distribution due to the interdigital electrodes and fibers. The MFC device is symmetric along the mid-plane axis thus the top and bottom interdigital electrode establishes a symmetric field distribution. Recall that the traditional PZT wafer yields a uniform field distribution. This uniform field distribution conveniently defines the field strength as the applied voltage per distance between the opposing electrodes. However, if we refer to electromagnetic field theory, the electric field strength is defined as the negative gradient of the applied electric potential, for example

$$\{\mathcal{E}\} = -\nabla V \quad (2.16)$$

Thus, the electric field is a function of the geometry of the given potential difference. Furthermore, the boundary condition of a conductor specifies that the tangential electric field must be zero and only a normal field component exists. Therefore, the geometry of parallel conducting plates, analogous to a traditional PZT wafer, yields a uniform field normal to the conductors as shown in Figure 2.9(a). However, if the same potential is prescribed between a conducting plane and vertex, then the field strength is characterized by the gradient of the potential as described in Eq.(2.16) and shown graphically in Figure 2.9(b).

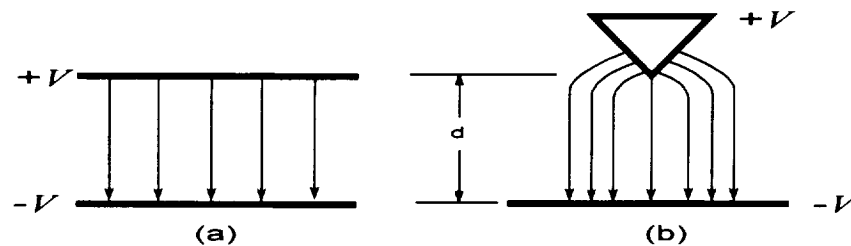


Figure 2.9 Electric Field Potential Gradient

Therefore, a significantly large non-uniform electric field distribution exists due to the gradient of the applied voltage present on the interdigital electrodes of an MFC wafer as shown in Figure 2.10.

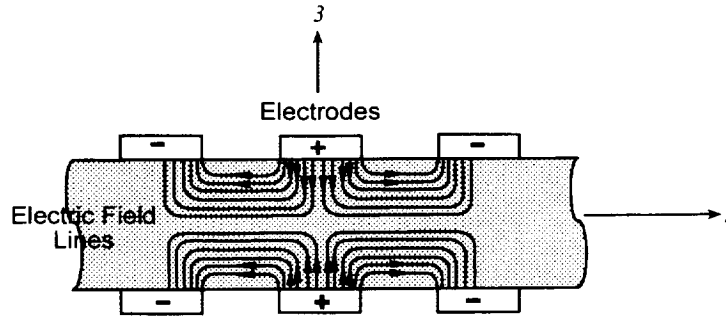


Figure 2.10 Non-uniform Electric Field Distribution of MFC

Within the area directly under the interdigital electrode, the piezoceramic experiences high field gradients of opposing directions; thus, the linear piezoelectric theory approximations may be exceeded. Bent³⁶ analyzed this effect using ANSYS[®] finite element analysis code; however, Bent assumed that the piezoceramic was uniformly poled along the length of the fiber, which is in contrast to the current MFC manufacturing process where the fiber is poled *in situ* and is therefore non-uniform along the fiber length.

Consistent with composite laminate theory, the local or principal material coordinates are independent of the global coordinates and are related through a geometrical transformation. The geometric orientation of an AFC patch is shown in Figure 2.11.

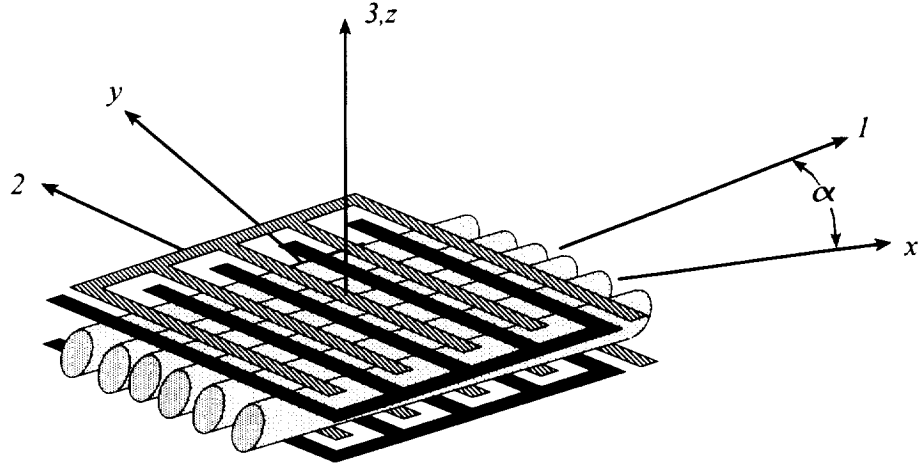


Figure 2.11 Principal and Global Coordinate Relation

The piezoceramic charge constants are proportional to strain and therefore follow the strain transformation found in composite mechanics.³⁹ Thus, the global charge constants can be determined from the material principal constants as

$$\begin{aligned}
 \begin{Bmatrix} d_x \\ d_y \\ d_{xy} \end{Bmatrix} &= \begin{bmatrix} \cos^2 \alpha & \sin^2 \alpha & \cos \alpha \sin \alpha \\ \sin^2 \alpha & \cos^2 \alpha & -\cos \alpha \sin \alpha \\ -2 \cos \alpha \sin \alpha & 2 \cos \alpha \sin \alpha & \cos^2 \alpha - \sin^2 \alpha \end{bmatrix}^{-1} \begin{Bmatrix} d_{11} \\ d_{12} \\ 0 \end{Bmatrix} \\
 &= \begin{bmatrix} \cos^2 \alpha & \sin^2 \alpha & 2 \cos \alpha \sin \alpha \\ \sin^2 \alpha & \cos^2 \alpha & -2 \cos \alpha \sin \alpha \\ -\cos \alpha \sin \alpha & \cos \alpha \sin \alpha & \cos^2 \alpha - \sin^2 \alpha \end{bmatrix} \begin{Bmatrix} d_{11} \\ d_{12} \\ 0 \end{Bmatrix} \quad (2.17)
 \end{aligned}$$

The piezoelectric charge constants d_{11} and d_{12} are being used to describe the MFC transducer pursuant to subsequent finite element analyses. When referring to traditional PZT transducers, charge constants d_{11} and d_{12} are equivalent to d_{31} and d_{32} , respectively.

CHAPTER III

FINITE ELEMENT FORMULATION

Introduction

The three-node MIN6 shallow shell element developed by Tessler⁴⁰ is modified to include the addition of piezoceramic electrical nodal DOF, cylindrical curvature, and membrane displacement field. The triangular element consists of fifteen structural nodal DOF to describe bending, rotation, and extensional displacement fields. The element formulation employs an anisoparametric interpolation scheme since quadratic interpolation polynomials approximate the deflection, while linear polynomials approximate the rotation and membrane displacement. This modeling is in contrast with isoparametric formulation where identical degree polynomials interpolate each of the primary variables. Using a quadratic polynomial for displacements requires six nodes per element; however, Tessler constrains the mid-edge nodes thereby achieving a reduction in element nodes. The MIN6 element is an enhanced version of Tessler's MIN3⁴¹ triangular Mindlin plate element. Subsequently, Chen demonstrated the ability of MIN3 to perform well under cylindrical curvature since he determined nonlinear post-buckling response with incremental structural deflections.⁴² This research further enhances the MIN6 element capability by including anisotropic piezoceramic materials in conjunction with first order shear deformation theory resulting in a fully coupled electrical-structural composite shallow cylindrical shell finite element.

Element Displacement Functions

The element displacement field components u_x , u_y , and u_w , consistent with Mindlin theory, are described as

$$\begin{aligned}
u_x &= u(x, y, t) + \bar{z} \theta_y(x, y, t) \\
u_y &= v(x, y, t) + \bar{z} \theta_x(x, y, t) \\
u_w &= w(x, y, t)
\end{aligned} \tag{3.1}$$

where u , v , w represent the mid-surface membrane (inplane) and transverse (out-of-plane) displacements; bending rotations of the normal about the x and y axes are given by θ_x and θ_y respectively. The element geometry is shown in Figure 3.1. The arbitrary shallow shell shape is described by $h_o(x, y)$ and is related to the z -axis as $\bar{z} = z - h_o(x, y)$. The cylindrical shape chosen for this research resulted by limiting the curvature to one direction; however, the formulation presented herein applies equally to geometry described by a double curvature.

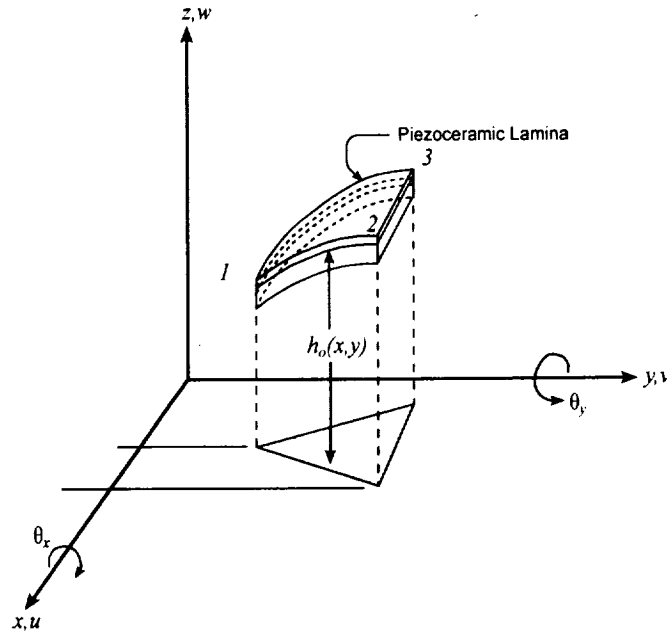


Figure 3.1 Shell Element Geometry

The element nodal displacement vectors are defined as

$$\{w\}^T = \left\{ \begin{bmatrix} w_b \end{bmatrix} \quad \begin{bmatrix} \theta \end{bmatrix} \quad \begin{bmatrix} w_m \end{bmatrix} \quad \begin{bmatrix} w_\phi \end{bmatrix} \right\} \tag{3.2}$$

$$\{w_b\}^T = \begin{bmatrix} w_1 & w_2 & w_3 \end{bmatrix} \tag{3.3}$$

$$\{\theta\}^T = [\theta_{x1} \quad \theta_{x2} \quad \theta_{x3} \quad \theta_{y1} \quad \theta_{y2} \quad \theta_{y3}] \quad (3.4)$$

$$\{w_m\}^T = [u_1 \quad u_2 \quad u_3 \quad v_1 \quad v_2 \quad v_3] \quad (3.5)$$

where each electrical DOF is the coupled electric potential of each piezoceramic layer.

For example, considering np piezoceramic layers, the electric potential DOF is given by

$$\{w_\phi\}^T = [V_1 \quad \cdots \quad V_{np}] \quad (3.6)$$

The electrical DOF follows traditional finite element assembly method where the electric boundary condition stipulates an equipotential across interelement boundaries for each continuous piezoceramic transducer. If more than one piezoceramic transducer is used, each is prescribed by an independent electrical DOF.

Given that the piezoelectric constitutive relation includes inherent two-way coupling between strain and charge, the electrical DOF must also account for the coupled fields. Hence, the intrinsic electrical DOF simultaneously describes both the self-generated charge, or sensor voltage, and the externally applied charge, or actuation voltage. The applied voltage and charge are linearly related through the piezoceramic capacitance as shown in Eq. (2.3). Further examination of the piezoelectric constitutive relation is discussed in greater detail in the subsequent Constitutive Relations section.

The displacement field throughout the element is determined by interpolating the nodal displacement as

$$\begin{aligned} w(x, y, t) &= [H_w] \{w_b\} + [H_{w\theta}] \{\theta\} \\ &= [\xi_1 \quad \xi_2 \quad \xi_3] \{w_b\} + [L_1 \quad L_2 \quad L_3 \quad M_1 \quad M_2 \quad M_3] \{\theta\} \end{aligned} \quad (3.7)$$

$$\theta_x(x, y, t) = [H_\alpha] \{\theta\} = [\xi_1 \quad \xi_2 \quad \xi_3 \quad 0 \quad 0 \quad 0] \{\theta\} \quad (3.8)$$

$$\theta_y(x, y, t) = [H_{\theta_y}] \{\theta\} = [0 \quad 0 \quad 0 \quad \xi_1 \quad \xi_2 \quad \xi_3] \{\theta\} \quad (3.9)$$

$$u(x, y, t) = [H_u] \{w_m\} = [\xi_1 \quad \xi_2 \quad \xi_3 \quad 0 \quad 0 \quad 0] \{w_m\} \quad (3.10)$$

$$v(x, y, t) = [H_v] \{w_m\} = [0 \quad 0 \quad 0 \quad \xi_1 \quad \xi_2 \quad \xi_3] \{w_m\} \quad (3.11)$$

where ξ_i are the area coordinates and L_i and M_i the quadratic interpolation polynomials.

Area, or natural coordinates commonly used to describe triangles, refer simply to area ratios as shown in Figure 3.2.

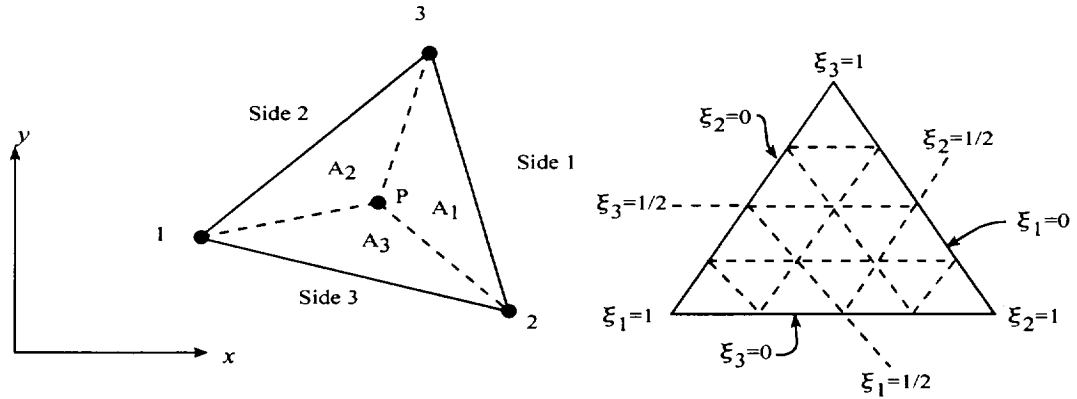


Figure 3.2 Element Area Coordinates

These area or natural coordinates ξ_1, ξ_2, ξ_3 are related to the geometric coordinates by utilizing the following transformation relations

$$\begin{Bmatrix} 1 \\ x \\ y \end{Bmatrix} = \begin{bmatrix} 1 & 1 & 1 \\ x_1 & x_2 & x_3 \\ y_1 & y_2 & y_3 \end{bmatrix} \begin{Bmatrix} \xi_1 \\ \xi_2 \\ \xi_3 \end{Bmatrix} \quad (3.12)$$

$$\begin{Bmatrix} \xi_1 \\ \xi_2 \\ \xi_3 \end{Bmatrix} = \frac{1}{2A} \begin{bmatrix} x_2 y_3 - x_3 y_2 & y_2 - y_3 & x_3 - x_2 \\ x_3 y_1 - x_1 y_3 & y_3 - y_1 & x_1 - x_3 \\ x_1 y_2 - x_2 y_1 & y_1 - y_2 & x_2 - x_1 \end{bmatrix} \begin{Bmatrix} 1 \\ x \\ y \end{Bmatrix}$$

where (x_i, y_i) designate the i^{th} nodal coordinate, and the triangular area A is given by

$$A = \frac{1}{2} ((x_2 - x_1)(y_3 - y_1) - (x_3 - x_1)(y_2 - y_1)).$$

The interpolation functions are defined as follows:

$$\begin{aligned}
L_1 &= \frac{1}{8}(b_3 N_4 - b_2 N_6) & L_2 &= \frac{1}{8}(b_1 N_5 - b_3 N_4) \\
L_3 &= \frac{1}{8}(b_3 2N_6 - b_1 N_5) & M_1 &= \frac{1}{8}(a_2 N_6 - a_3 N_4) \\
M_2 &= \frac{1}{8}(a_3 N_4 - a_1 N_5) & M_3 &= \frac{1}{8}(a_1 N_5 - a_2 N_6) \\
N_4 &= 4\xi_1 \xi_2 & N_5 &= 4\xi_2 \xi_3 & N_6 &= 4\xi_3 \xi_1 \\
a_1 &= x_{32} & a_2 &= x_{13} & a_3 &= x_{21} \\
b_1 &= y_{32} & b_2 &= y_{13} & b_3 &= y_{21} \\
x_{ij} &= x_i - x_j & y_{ij} &= y_i - y_j
\end{aligned} \tag{3.13}$$

Strain Displacement Functions

The strain-displacement relation is expressed by including the membrane strain and curvature as

$$\{\boldsymbol{\varepsilon}\} = \begin{Bmatrix} \varepsilon_x \\ \varepsilon_y \\ \gamma_{xy} \end{Bmatrix} = \{\boldsymbol{\varepsilon}^o\} + \bar{z} \{\boldsymbol{\kappa}\} \tag{3.14}$$

The Margurre membrane strain-displacement relations for a thin shallow shell are defined as

$$\{\boldsymbol{\varepsilon}^o\} = \begin{Bmatrix} u_{,x} \\ v_{,y} \\ u_{,y} + v_{,x} \end{Bmatrix} + \begin{Bmatrix} h_{o,x} w_{,x} \\ h_{o,y} w_{,y} \\ h_{o,y} w_{,x} + h_{o,x} w_{,y} \end{Bmatrix} \tag{3.15}$$

For notational compactness, the subscript comma is used to denote partial differentiation with respect to the coordinate variable, therefore $u_{,x} \equiv \frac{\partial u(x,y)}{\partial x}$. Tessler⁴⁰ discusses an important inherent difference in the transverse displacement variables defined in Reissner-Mindlin and Marguerre theories that must be addressed when the two theories are merged. The Reissner-Mindlin theory includes shear deformation; therefore, the transverse variable is a weighted average transverse displacement through the

thickness, whereas Marguerre theory assumes mid-plane transverse displacement as a consequence of neglecting shear deformation using the Kirchhoff theory. Enforcing the Kirchhoff thinness assumption yields

$$\begin{Bmatrix} w_{,x} \\ w_{,y} \end{Bmatrix} = - \begin{Bmatrix} \theta_y \\ \theta_x \end{Bmatrix} \quad (3.16)$$

Thus, the membrane strain in Eq. (3.15) becomes

$$\begin{aligned} \{\epsilon^o\} &= \begin{Bmatrix} u_{,x} \\ v_{,y} \\ u_{,y} + v_{,x} \end{Bmatrix} - \begin{Bmatrix} h_{o,x} \theta_y \\ h_{o,y} \theta_x \\ h_{o,y} \theta_y + h_{o,x} \theta_x \end{Bmatrix} \\ &= [C_m] \{w_m\} - \begin{bmatrix} h_{o,x} & 0 \\ 0 & h_{o,y} \\ h_{o,y} & h_{o,x} \end{bmatrix} \begin{Bmatrix} \theta_y \\ \theta_x \end{Bmatrix} \\ &= [C_m] \{w_m\} - [h_o] [C_{xy}] \{\theta\} \end{aligned} \quad (3.17)$$

For a cylindrical shell formulation $h_{o,x} = 0$ and the remaining slope of the curvature is determined from

$$h_{o,y} = \frac{b - 2y}{2\sqrt{r^2 - b^2/4 + b/y - y^2}} \quad (3.18)$$

where b is the length of the cylindrical panel along the local y coordinate and r is the radius of curvature, as shown in Figure 3.3.

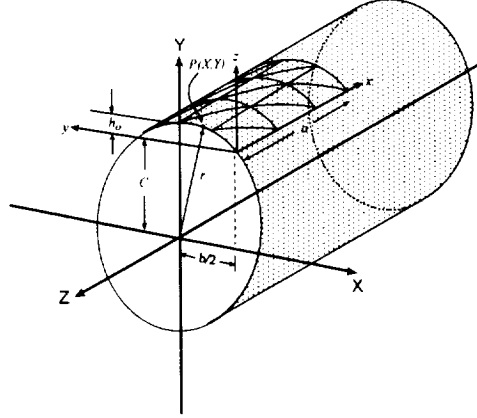


Figure 3.3 Shell Curvature Geometry

Furthermore, the curvature and shear strain are defined as

$$\{\kappa\} = \begin{Bmatrix} \theta_{y,x} \\ \theta_{x,y} \\ \theta_{y,y} + \theta_{x,x} \end{Bmatrix} = [C_b] \{\theta\} \quad (3.19)$$

$$\begin{aligned} \{\gamma\} &= \begin{Bmatrix} \gamma_{yz} \\ \gamma_{xz} \end{Bmatrix} = \begin{Bmatrix} w_{,y} \\ w_{,x} \end{Bmatrix} + \begin{Bmatrix} \theta_x \\ \theta_y \end{Bmatrix} \\ &= [C_{\gamma b}] \{w_b\} + [C_{\gamma \theta}] \{\theta\} \end{aligned} \quad (3.20)$$

The strain interpolation matrices result from completing the required differentiation indicated by the strain-displacement relations on the displacement interpolation functions. The defined strain interpolation matrices are summarized as follows:

$$[C_m] = \begin{bmatrix} [H_u]_{,x} \\ [H_v]_{,y} \\ [H_v]_{,x} + [H_u]_{,y} \end{bmatrix} = \frac{1}{2A} \begin{bmatrix} y_{23} & y_{31} & y_{12} & 0 & 0 & 0 \\ 0 & 0 & 0 & x_{32} & x_{13} & x_{21} \\ x_{32} & x_{13} & x_{21} & y_{23} & y_{31} & y_{12} \end{bmatrix} \quad (3.21)$$

$$[C_b] = \begin{bmatrix} [H_{\theta_y}]_{,x} \\ [H_{\theta_x}]_{,y} \\ [H_{\theta_x}]_{,x} + [H_{\theta_y}]_{,y} \end{bmatrix} = \frac{1}{2A} \begin{bmatrix} 0 & 0 & 0 & y_{23} & y_{31} & y_{12} \\ x_{32} & x_{13} & x_{21} & 0 & 0 & 0 \\ y_{23} & y_{31} & y_{12} & x_{32} & x_{13} & x_{21} \end{bmatrix} \quad (3.22)$$

$$[C_{xy}] = \begin{bmatrix} H_{\theta_y} \\ H_{\theta_x} \end{bmatrix} = \begin{bmatrix} 0 & 0 & 0 & \xi_1 & \xi_2 & \xi_3 \\ \xi_1 & \xi_2 & \xi_3 & 0 & 0 & 0 \end{bmatrix} \quad (3.23)$$

$$[C_{\phi}] = \begin{bmatrix} H_w \downarrow_y \\ H_w \downarrow_x \end{bmatrix} = \frac{1}{2A} \begin{bmatrix} x_{32} & x_{13} & x_{21} \\ y_{23} & y_{31} & y_{12} \end{bmatrix} \quad (3.24)$$

$$[C_{\phi\theta}] = \begin{bmatrix} H_{w\theta} \downarrow_y + H_{\alpha_x} \\ H_{w\theta} \downarrow_x + H_{\theta_y} \end{bmatrix} \quad (3.25)$$

Constitutive Relations

The k^{th} layer of the laminate specifies either structural or piezoceramic properties and is characterized by the following coupled constitutive relations

$$\{\sigma\}_k = [\bar{Q}]_k (\{\varepsilon\} - \mathcal{E}_{ik} \{d\}_k) \quad (3.26)$$

$$\begin{aligned} \{\tau\}_k &= \begin{Bmatrix} \tau_{yz} \\ \tau_{xz} \end{Bmatrix}_k = \begin{bmatrix} \bar{Q}_{44} & \bar{Q}_{45} \\ \bar{Q}_{45} & \bar{Q}_{55} \end{bmatrix}_k \begin{Bmatrix} \gamma_{yz} \\ \gamma_{xz} \end{Bmatrix} \\ &= [\bar{Q}_s]_k \{\gamma\} \end{aligned} \quad (3.27)$$

$$\mathcal{D}_{3k} = \{d\}_k^T [\bar{Q}]_k (\{\varepsilon\} - \mathcal{E}_{ik} \{d\}_k) + \epsilon_{ik}^{\sigma} \mathcal{E}_{ik} \quad (3.28)$$

where $i=1$ or 3 for MFC or traditional PZT transducers, respectively. The electric field is related to the electric potential DOF as

$$\begin{Bmatrix} \mathcal{E}_1 \\ \vdots \\ \mathcal{E}_{np} \end{Bmatrix} = -[B_{\phi}] \{w_{\phi}\} = - \begin{bmatrix} \frac{1}{h_1} & \dots & 0 \\ \vdots & \ddots & \vdots \\ 0 & \dots & \frac{1}{h_{np}} \end{bmatrix} \begin{Bmatrix} V_1 \\ \vdots \\ V_{np} \end{Bmatrix} \quad (3.29)$$

and h_i describes the electrode spacing, either through the thickness for conventional piezoceramics or the electrode spacing of the interdigital electrodes for MFC transducers.

The constitutive relations describe the fundamental behavior of electrical and mechanical properties used throughout the rest of the formulation. The electric flux density \mathcal{D} describes the electric field \mathcal{E} independent of dielectric used as shown in Eq. (2.10). However, the inherent two-way coupling between stress and electric field is clearly indicated in Eqs. (3.26) and (3.28). Interestingly, the electric field and subsequent flux density is a function of strain, which is related to the state of stress. Therefore, the electric field intrinsically depends on strain, which is a function of the electric field. This coupling must be accounted for whether the piezoceramic is a sensor or actuator.

Laminated composite theory provides a convenient modeling procedure even if an isotropic plate with bonded piezoceramic layers is considered, since the piezoceramic constitutes a lamina. Hence, lamina reduced stiffness components are determined from the principal material properties as

$$\begin{aligned} Q_{11} &= \frac{E_1}{1 - \nu_{12}\nu_{21}}, & Q_{12} &= \frac{\nu_{12}E_2}{1 - \nu_{12}\nu_{21}}, & Q_{22} &= \frac{E_2}{1 - \nu_{12}\nu_{21}} \\ Q_{66} &= G_{12}, & Q_{44} &= G_{23}, & Q_{55} &= G_{12} \end{aligned} \quad (3.30)$$

The ability to accurately model piezoceramic anisotropy supports current research trends in advanced transducer development. For anisotropic piezoceramic material, such as an MFC transducer, the principal mechanical properties are included at the constitutive level.

Force and Moment Resultant

Analysis of laminated composites maintains distinct lamina stresses; therefore, utilizing stress resultants is imperative. The stress resultants, or force and moment per unit length, are defined as

$$(\{N\}, \{M\}) = \int_{-h/2}^{h/2} \{\sigma\}_k (1, \bar{z}) d\bar{z} \quad (3.31)$$

$$\{R\} = \int_{-h/2}^{h/2} \begin{Bmatrix} \tau_{yz} \\ \tau_{xz} \end{Bmatrix}_k d\bar{z} \quad (3.32)$$

Utilizing Eqs.(3.31) and (3.32), it is useful to define the stress resultants as follows:

$$\begin{aligned} \begin{Bmatrix} N \\ M \end{Bmatrix} &= \begin{bmatrix} [A] & [B] \\ [B] & [D] \end{bmatrix} \begin{Bmatrix} \epsilon^o \\ \kappa \end{Bmatrix} - \begin{Bmatrix} N_\phi \\ M_\phi \end{Bmatrix} \\ \{R\} &= [A_s] \{\gamma\} \end{aligned} \quad (3.33)$$

where the extension, extension-bending, bending, and shear stiffness matrices are defined as

$$[A] = \sum_{k=1}^n [\bar{Q}]_k (\bar{z}_{k+1} - \bar{z}_k) \quad (3.34)$$

$$[B] = \frac{1}{2} \sum_{k=1}^n [\bar{Q}]_k (\bar{z}_{k+1}^2 - \bar{z}_k^2) \quad (3.35)$$

$$[D] = \frac{1}{3} \sum_{k=1}^n [\bar{Q}]_k (\bar{z}_{k+1}^3 - \bar{z}_k^3) \quad (3.36)$$

$$[A_s] = \sum_{k=1}^n [\bar{Q}_s]_k (\bar{z}_{k+1} - \bar{z}_k) \quad (3.37)$$

Considering the k^{th} piezoceramic layer and the coupled constitutive relations the piezoceramic force and moment vectors are given by

$$(\{N_\phi\}, \{M_\phi\}) = \int_{-h/2}^{h/2} [\bar{Q}]_k \{d\}_k \mathcal{E}_{3k} (1, \bar{z}) d\bar{z} \quad (3.38)$$

Equations of Motion

Finite element equations of motion for the laminated composite shell with fully coupled electrical-structural properties are derived utilizing the generalized Hamilton's principle⁴³ to obtain

$$\int_1^2 \delta(T - U + W_e - W_m + W) dt = 0 \quad (3.39)$$

where T and U are the kinetic energy and strain energy of the system, W_e is the electrical energy, W_m is the magnetic energy, and W is the work done due to external forces and applied electric field. The magnetic energy is negligible for piezoceramic materials if no external magnetic fields are located near the specimen.

The kinetic energy of the shallow shell finite element is defined as

$$T = \int_V \frac{1}{2} \rho (\{\dot{w}\}^T \{\dot{w}\} + \{\dot{u}\}^T \{\dot{u}\} + \{\dot{v}\}^T \{\dot{v}\}) dV \quad (3.40)$$

where \dot{w} , \dot{u} , and \dot{v} are the transverse and membrane velocity components and ρ is the mass per unit volume, and V is the volume of the element. The potential and electrical energy are defined as

$$U = \int_V \frac{1}{2} (\{\epsilon\}^T \{\sigma\} + \{\gamma\}^T \{\tau\}) dV \quad (3.41)$$

$$W_e = \int_V \frac{1}{2} \{\mathcal{E}\}^T \{\mathcal{D}\} dV \quad (3.42)$$

and the work done on the element by external sources is defined as

$$W = \int_V \{w\}^T \{F_b\} dV + \int_{S_1} \{w\}^T \{F_s\} dS + \{w\}^T \{F_c\} - \int_{S_2} V \rho_{cs} dS \quad (3.43)$$

where $\{F_b\}$ is the body force vector, $\{F_s\}$ is the surface traction vector, $\{F_c\}$ is the concentrated loading vector, S_1 is the surface area of the applied traction, S_2 is the surface area of the piezoelectric material, V is the voltage applied to the piezoceramic layer, and ρ_{cs} is the total electrical charge due to self-generated piezoelectricity in addition to the applied actuation voltage. Recall that a voltage applied to a capacitor yields an

accumulation of charges on its conductors. Thus, the actuation voltage produces charges across the intrinsic piezoceramic capacitance. In Hamilton's principle, all variations must vanish at the time $t = t_1$ and $t = t_2$. The Hamilton's variational statement may be written as

$$\begin{aligned} & \int_V [\rho \{ \delta \dot{w} \}^T \{ \dot{w} \} + \{ \delta \dot{u} \}^T \{ \dot{u} \} + \{ \delta \dot{v} \}^T \{ \dot{v} \}] \\ & - \{ \delta \epsilon \}^T \{ \sigma \} + \{ \delta E \}^T \{ D \} + \{ \delta w \}^T \{ F_b \}] dV \\ & + \int_{S_1} \{ \delta w \}^T \{ F_s \} dS - \int_{S_2} \delta V \rho_{cs} dS + \{ \delta w \}^T \{ F_c \} = 0 \end{aligned} \quad (3.44)$$

Evaluation of Eq. (3.44) leads to the development of the finite element matrices and the elemental equations of motion. Employing the stress resultants, the variational potential and electrical energy may be described as

$$\delta(U - W_e) = \int_A \left(\{ \delta \epsilon^o \}^T \{ N \} + \{ \delta \kappa \}^T \{ M \} + \alpha \{ \delta \gamma \}^T \{ R \} - \{ \delta E \}^T \{ D \} \right) dA \quad (3.45)$$

where the shear correction factor for the MIN6 element is defined as

$$\alpha = \left(1 + 0.5 \left(\frac{tr(k_{\gamma\theta})}{tr(k_\theta)} \right) \right)^{-1}, \quad (3.46)$$

with $tr(k_{\gamma\theta})$ and $tr(k_\theta)$ denoting the trace or summation of diagonal terms of the coupled shear-bending and bending element stiffness matrices respectively. Tessler provides a more complete derivation for the shear correction factor along with an enhanced higher order membrane interpolation scheme.⁴⁰

The finite element equations can be determined by completing the variational work statement in terms of the nodal values. Writing the stress resultants described in Eq.(3.45) in the nodal quantities yields

$$\begin{aligned}\{N\} &= [A]\{\varepsilon^o\} + [B]\{\kappa\} - \{N_\phi\} \\ &= [A][C_m]\{w_m\} - [A][h_o][C_{xy}]\{\theta\} + [B][C_b]\{\theta\} - \{N_\phi\}\end{aligned}\quad (3.47)$$

$$\begin{aligned}\{M\} &= [B]\{\varepsilon^o\} + [D]\{\kappa\} - \{M_\phi\} \\ &= [B][C_m]\{w_m\} - [B][h_o][C_{xy}]\{\theta\} + [D][C_b]\{\theta\} - \{M_\phi\}\end{aligned}\quad (3.48)$$

$$\{R\} = [A_s][C_{\gamma\theta}]\{w_b\} + [A_s][C_{\gamma\theta}]\{\theta\} \quad (3.49)$$

The variation of the electrical energy term in Eq.(3.45) is expanded by including the piezoelectric constitutive relation in Eq.(3.28). Since the piezoceramic layers are separated by general lamina, integration through the thickness must be carried out for the np piezoceramic layers only. Hence, the variational electric energy becomes

$$\begin{aligned}& \int_A \int_{-h/2}^{h/2} [(\delta \mathcal{E}_{3k}) \mathcal{D}_{3k} d\bar{z}] dA = \\ & \int_A \left[\sum_{k=1}^{np} \int_{\bar{z}_k}^{\bar{z}_{k+1}} [(\delta \mathcal{E}_{3k}) \{d\}_k^T [\bar{Q}]_k (\{\varepsilon^o\} + \bar{z} \{\kappa\} - \mathcal{E}_{3k} \{d\}_k) + \epsilon_{33k}^\sigma \mathcal{E}_{3k}] d\bar{z} \right] dA\end{aligned}\quad (3.50)$$

Completing the integration with respect to \bar{z} yields

$$\begin{aligned}& \int_A \left[\sum_{k=1}^{np} [(\delta \mathcal{E}_{3k}) \{d\}_k^T [\bar{Q}]_k h_k \{\varepsilon^o\} + (\delta \mathcal{E}_{3k}) \{d\}_k^T [\bar{Q}]_k \{\kappa\} \frac{h_k}{2} (\bar{z}_{k+1} + \bar{z}_k) \right. \\ & \left. - (\delta \mathcal{E}_{3k}) \{d\}_k^T [\bar{Q}]_k \{d\}_k \mathcal{E}_{3k} h_k + (\delta \mathcal{E}_{3k}) \epsilon_{33k}^\sigma \mathcal{E}_{3k} h_k \right] dA\end{aligned}\quad (3.51)$$

Before continuing, we can further expand the definitions of the piezoelectric force and moment vectors. The force vector may be expressed as

$$\begin{aligned}\{N_\phi\} &= \sum_{k=1}^{np} [\bar{Q}]_k \{d\}_k h_k \mathcal{E}_{3k} \\ &= \left[[\bar{Q}]_1 \{d\}_1 h_1 \quad \cdots \quad [\bar{Q}]_k \{d\}_k h_k \quad \cdots \quad [\bar{Q}]_{np} \{d\}_{np} h_{np} \right] \{\mathcal{E}_3\} \\ &= - \left[[\bar{Q}]_1 \{d\}_1 h_1 \quad \cdots \quad [\bar{Q}]_k \{d\}_k h_k \quad \cdots \quad [\bar{Q}]_{np} \{d\}_{np} h_{np} \right] [B_\phi] \{w_\phi\} \\ &= - [P_N] [B_\phi] \{w_\phi\}\end{aligned}\quad (3.52)$$

Similarly, the piezoelectric moment vector follows as

$$\{M_\phi\} = -[P_M][B_\phi]\{w_\phi\} \quad (3.53)$$

where

$$[P_M] = \begin{bmatrix} \frac{1}{2}[\bar{Q}]_1 \{d\}_1 h_1 (\bar{z}_2 + \bar{z}_1) & \cdots & \frac{1}{2}[\bar{Q}]_k \{d\}_k h_k (\bar{z}_{k+1} + \bar{z}_k) & \cdots \\ \vdots & & \vdots & \\ \frac{1}{2}[\bar{Q}]_{np} \{d\}_{np} h_{np} (\bar{z}_{np+1} + \bar{z}_{np}) \end{bmatrix} \quad (3.54)$$

Equation (3.51) can be recast in matrix form using the above definitions as

$$\int_A \{\delta \mathcal{E}_3\}^T ([P_N]^T \{\epsilon^o\} + [P_M]^T \{\kappa\} - [\chi][B_\phi]^{-1} \{\mathcal{E}_3\} + [\epsilon_{33}^\sigma][B_\phi]^{-1} \{\mathcal{E}_3\}) dA \quad (3.55)$$

where

$$[\chi] = \begin{bmatrix} \{d\}_1^T [\bar{Q}]_1 \{d\}_1 & \cdots & 0 \\ \vdots & \{d\}_k^T [\bar{Q}]_k \{d\}_k & \vdots \\ 0 & \cdots & \{d\}_{np}^T [\bar{Q}]_{np} \{d\}_{np} \end{bmatrix} \quad (3.56)$$

Thus, by completing the necessary substitutions the variational energy statement becomes

$$\begin{aligned} \delta(U - W_e) &= \int_A \left(\{\delta \epsilon^o\}^T \{N\} + \{\delta \kappa\}^T \{M\} + \alpha \{\delta \gamma\}^T \{R\} - \{\delta \mathcal{E}\}^T \{\mathcal{D}\} \right) dA \\ &= \int_A \left(\{(-\{\delta \theta\}^T [C_{xy}]^T [h_o]^T + \{\delta w_m\}^T [C_m]^T) \right. \\ &\quad \left([A][C_m]\{w_m\} - [A][h_o][C_{xy}]\{\theta\} + [B][C_b]\{\theta\} - \{N_\phi\} \right) \\ &\quad + \{\delta \theta\}^T [C_b]^T ([B][C_m]\{w_m\} - [B][h_o][C_{xy}]\{\theta\} \\ &\quad + [D][C_b]\{\theta\} - \{M_\phi\}) \\ &\quad + \alpha \left(\{\delta w_b\}^T [C_{rb}]^T + \{\delta \theta\}^T [C_{r\theta}]^T \right) \\ &\quad \left([A_s][C_{rb}]\{w_b\} + [A_s][C_{r\theta}]\{\theta\} \right) \\ &\quad - \{\delta \mathcal{E}\}^T \left([P_N]^T ([C_m]\{w_m\} - [h_o][C_{xy}]\{\theta\}) \right. \\ &\quad \left. + [P_M]^T [C_b]\{\theta\} + ([\epsilon^\sigma] - [\chi])[B_\phi]^T \{\mathcal{E}\} \right) dA \end{aligned} \quad (3.57)$$

Expanding Eq.(3.57) term by term yields expressions leading to the element stiffness matrices

$$= \int_A \left(-\{\delta\theta\}^T [C_{xy}]^T [h_o]^T [A][C_m]\{w_m\} \right. \quad (3.58)$$

$$+ \{\delta\theta\}^T [C_{xy}]^T [h_o]^T [A][h_o][C_{xy}]\{\theta\} \quad (3.59)$$

$$- \{\delta\theta\}^T [C_{xy}]^T [h_o]^T [B][C_b]\{\theta\} \quad (3.60)$$

$$+ \{\delta\theta\}^T [C_{xy}]^T [h_o]^T \{N_\phi\} \quad (3.61)$$

$$+ \{\delta w_m\}^T [C_m]^T [A][C_m]\{w_m\} \quad (3.62)$$

$$- \{\delta w_m\}^T [C_m]^T [A][h_o][C_{xy}]\{\theta\} \quad (3.63)$$

$$+ \{\delta w_m\}^T [C_m]^T [B][C_b]\{\theta\} \quad (3.64)$$

$$- \{\delta w_m\}^T [C_m]^T \{N_\phi\} \quad (3.65)$$

$$+ \{\delta\theta\}^T [C_b]^T [B][C_m]\{w_m\} \quad (3.66)$$

$$- \{\delta\theta\}^T [C_b]^T [B][h_o][C_{xy}]\{\theta\} \quad (3.67)$$

$$+ \{\delta\theta\}^T [C_b]^T [D][C_b]\{\theta\} \quad (3.68)$$

$$- \{\delta\theta\}^T [C_b]^T \{M_\phi\} \quad (3.69)$$

$$+ \alpha \{\delta w_b\}^T [C_{yb}]^T [A_s][C_{yb}]\{w_b\} \quad (3.70)$$

$$+ \alpha \{\delta w_b\}^T [C_{yb}]^T [A_s][C_{y\theta}]\{\theta\} \quad (3.71)$$

$$+ \alpha \{\delta\theta\}^T [C_{y\theta}]^T [A_s][C_{yb}]\{w_b\} \quad (3.72)$$

$$+ \alpha \{\delta\theta\}^T [C_{y\theta}]^T [A_s][C_{y\theta}]\{\theta\} \quad (3.73)$$

$$+\{\delta w_\phi\}^T [B_\phi]^T [P_N]^T [C_m]\{w_m\} \quad (3.74)$$

$$-\{\delta w_\phi\}^T [B_\phi]^T [P_N]^T [h_o][C_{xy}]\{\theta\} \quad (3.75)$$

$$+\{\delta w_\phi\}^T [B_\phi]^T [P_M]^T [C_b]\{\theta\} \quad (3.76)$$

$$+\{\delta w_\phi\}^T [B_\phi]^T ([\epsilon_{33}^\sigma] - [\chi])\{w_\phi\} dA \quad (3.77)$$

Completing the generalized Hamilton's principle considering nodal DOF yields inertia, external mechanical loading, and piezoceramic actuation quantities

$$\begin{aligned} \delta W_{external} = & \int_A \left(\{\delta w_b\}^T \{H_w\} + \{\delta \theta\}^T \{H_{w\theta}\} \right) \\ & \left(p(x, y, t) - \rho h ([H_w] \{\ddot{w}_b\} + [H_{w\theta}] \{\ddot{\theta}\}) \right) \\ & - \rho h \{\delta w_m\}^T (\{H_u\} [H_u] \{\ddot{w}_m\} - \{H_v\} [H_v] \{\ddot{w}_m\}) dA \\ & - \int_{S_p} \{\delta w_\phi\}^T \{\rho_{cs}\} dA \end{aligned} \quad (3.78)$$

Evaluating the potential and electrical energies of the variational work statement yields the finite element inertial and stiffness matrices. Succinctly expanding Eqs.(3.58)-(3.78) using typical finite element notation clearly indicates element stiffness matrices including fully coupled electrical-structural shallow shell element and element inertial matrices. Each element stiffness matrix contribution is summarized as follows:

$$\{\delta \theta\}^T [k_\theta] \{\theta\} \text{ where } [k_b] = \int_A [C_b]^T [D] [C_b] dA \quad (3.79)$$

$$\{\delta w_m\} [k_{m\theta}] \{\theta\} \text{ where } [k_{mb}] = \int_A [C_m]^T [B] [C_b] dA \quad (3.80)$$

$$\{\delta \theta\} [k_{\theta m}] \{w_m\} \text{ where } [k_{bm}] = \int_A [C_b]^T [B] [C_m] dA \quad (3.81)$$

$$\{\delta w_m\}^T [k_m] \{w_m\} \text{ where } [k_m] = \int_A [C_m]^T [A] [C_m] dA \quad (3.82)$$

The following element stiffness matrices represent geometric stiffness due to the shallow shell geometry:

$$\{\delta \theta\}^T [k_{b\theta}]_o \{\theta\} \text{ where } [k_{b\theta}]_o = - \int_A [C_b]^T [B] [h_o] [C_{xy}] dA \quad (3.83)$$

$$\{\delta \theta\}^T [k_{\theta b}]_o \{\theta\} \text{ where } [k_{\theta b}]_o = - \int_A [C_{xy}]^T [h_o]^T [B] [C_b] dA \quad (3.84)$$

$$\{\delta w_m\}^T [k_{m\theta}]_o \{\theta\} \text{ where } [k_{m\theta}]_o = - \int_A [C_m]^T [A] [h_o] [C_{xy}] dA \quad (3.85)$$

$$\{\delta \theta\}^T [k_{\theta m}]_o \{w_m\} \text{ where } [k_{\theta m}]_o = - \int_A [C_{xy}]^T [h_o]^T [A] [C_m] dA \quad (3.86)$$

$$\{\delta \theta\}^T [k_\theta]_o \{\theta\} \text{ where } [k_\theta]_o = \int_A [C_{xy}]^T [h_o]^T [A] [h_o] [C_{xy}] dA \quad (3.87)$$

The following element stiffness matrices represent the shear strain effect:

$$\alpha \{\delta \theta\}^T [k_\theta]_s \{\theta\} \text{ where } [k_\theta]_s = \int_A [C_{\gamma\theta}]^T [A_s] [C_{\gamma\theta}] dA \quad (3.88)$$

$$\alpha \{\delta \theta\}^T [k_{\theta b}]_s \{w_b\} \text{ where } [k_{\theta b}]_s = \int_A [C_{\gamma\theta}]^T [A_s] [C_{\gamma b}] dA \quad (3.89)$$

$$\alpha \{\delta w_b\}^T [k_{b\theta}]_s \{\theta\} \text{ where } [k_{b\theta}]_s = \int_A [C_{\gamma b}]^T [A_s] [C_{\gamma\theta}] dA \quad (3.90)$$

$$\alpha \{\delta w_b\}^T [k_b]_s \{w_b\} \text{ where } [k_b]_s = \int_A [C_{\gamma b}]^T [A_s] [C_{\gamma b}] dA \quad (3.91)$$

The following element stiffness matrices represents coupled piezoelectric-structural stiffness:

$$\{\delta w_m\}^T [k_{m\phi}] \{w_\phi\} \text{ where } [k_{m\phi}] = \int_A [C_m]^T [P_N] [B_\phi] dA \quad (3.92)$$

$$\{\delta w_\phi\}^T [k_{\phi m}] \{w_m\} \text{ where } [k_{\phi m}] = \int_A [B_\phi]^T [P_N]^T [C_m] dA \quad (3.93)$$

$$\{\delta \theta\}^T [k_{\phi \theta}] \{w_\phi\} \text{ where } [k_{\phi \theta}] = \int_A [C_b]^T [P_M]^T [B_\phi] dA \quad (3.94)$$

$$\{\delta w_\phi\}^T [k_{\phi \theta}] \{\theta\} \text{ where } [k_{\phi \theta}] = \int_A [B_\phi]^T [P_M]^T [C_b] dA \quad (3.95)$$

$$\{\delta w_\phi\}^T [k_{\phi \theta}]_o \{\theta\} \text{ where } [k_{\phi \theta}]_o = - \int_A [B_\phi]^T [P_N]^T [h_o] [C_{xy}] dA \quad (3.96)$$

$$\{\delta w_b\}^T [k_{\phi \theta}]_o \{w_\phi\} \text{ where } [k_{\phi \theta}]_o = \int_A [C_{xy}]^T [h_o]^T [P_N]^T [B_\phi] dA \quad (3.97)$$

$$\{\delta w_\phi\}^T [k_\phi] \{w_\phi\} \text{ where } [k_\phi] = \int_A [B_\phi]^T ([\epsilon_{33}^\sigma] - [\chi]) dA \quad (3.98)$$

The following element matrices represent inertial matrices and load vectors from the potential energy and external work indicated in Eq. (3.78):

$$[m_b] = \int_A [H_w]^T \rho [H_w] dA \quad (3.99)$$

$$[m_{b\theta}] = \int_A [H_w]^T \rho [H_{w\theta}] dA \quad (3.100)$$

$$[m_{\theta b}] = \int_A [H_{w\theta}]^T \rho [H_w] dA \quad (3.101)$$

$$[m_\theta] = \int_A [H_{w\theta}]^T \rho [H_{w\theta}] dA \quad (3.102)$$

$$[m_m] = \int_A ([H_u] + [H_u])^T \rho ([H_u] + [H_u]) dA \quad (3.103)$$

$$\{p_b(t)\} = \int_A [H_w]^T p(x, y, t) dA \quad (3.104)$$

$$\{p_\theta(t)\} = \int_A [H_{w\theta}]^T p(x, y, t) dA \quad (3.105)$$

$$\{p_\phi(t)\} = - \int_A \rho_{cs} dA \quad (3.106)$$

Furthermore, using matrix equation notation yields the following finite element equations of motion:

$$\begin{aligned} & \begin{bmatrix} m_b & m_{b\theta} & 0 & 0 \\ m_{\theta b} & m_\theta & 0 & 0 \\ 0 & 0 & m_m & 0 \\ 0 & 0 & 0 & 0 \end{bmatrix} \begin{Bmatrix} \ddot{w}_b \\ \ddot{\theta} \\ \ddot{w}_m \\ \ddot{w}_\phi \end{Bmatrix} + \begin{bmatrix} 0 & 0 & 0 & 0 \\ 0 & k_\theta & k_{\theta m} & k_{\theta \phi} \\ 0 & k_{m\theta} & k_m & k_{m\phi} \\ 0 & k_{\phi\theta} & k_{\phi m} & k_\phi \end{bmatrix} \begin{Bmatrix} w_b \\ \theta \\ w_m \\ w_\phi \end{Bmatrix} + \begin{bmatrix} 0 & k_{b\theta_s} & 0 & 0 \\ k_{\theta b_s} & k_{\theta_s} & k_{\theta m_s} & k_{\theta \phi_s} \\ 0 & k_{m\theta_s} & 0 & 0 \\ 0 & k_{\phi\theta_s} & 0 & 0 \end{bmatrix} \begin{Bmatrix} w_b \\ \theta \\ w_m \\ w_\phi \end{Bmatrix} \\ & + \alpha \begin{bmatrix} k_{b_s} & k_{b\theta_s} & 0 & 0 \\ k_{\theta b_s} & k_{\theta_s} & 0 & 0 \\ 0 & 0 & 0 & 0 \\ 0 & 0 & 0 & 0 \end{bmatrix} \begin{Bmatrix} w_b \\ \theta \\ w_m \\ w_\phi \end{Bmatrix} = \begin{Bmatrix} p_b(t) \\ p_\theta(t) \\ 0 \\ p_\phi(t) \end{Bmatrix} \quad (3.107) \end{aligned}$$

Once the element mass and stiffness matrices are determined, they can be applied to specific structural configurations by prescribing boundary conditions, and associated loading. By following conventional finite element assembly procedures a global system of equations can be determined to represent the structure. Assembly can be carried out for various loading and boundary conditions without calculating the element level matrices.

Global Equations of Motion

Following standard finite element assembly procedures, the system equations of motion can be expressed as

$$\begin{bmatrix} M & 0 \\ 0 & 0 \end{bmatrix} \begin{Bmatrix} \ddot{W} \\ \ddot{W}_\phi \end{Bmatrix} + \begin{bmatrix} K_w & K_{w\phi} \\ K_{\phi w} & K_\phi \end{bmatrix} \begin{Bmatrix} W \\ W_\phi \end{Bmatrix} + \begin{bmatrix} K_s & 0 \\ 0 & 0 \end{bmatrix} \begin{Bmatrix} W \\ W_\phi \end{Bmatrix} = \begin{Bmatrix} P_w \\ P_\phi \end{Bmatrix} \quad (3.108)$$

Assembly accounts for both the number of piezoceramic layers and multiple transducer patches. To facilitate the solution process, it is convenient to manipulate Eq. (3.108) to

account for the coupled field properties previously discussed. First, Eq. (3.108) is partitioned into the following two equations

$$[M]\{\ddot{W}\} + ([K_w] + [K_s])\{W\} + [K_{w\phi}]\{W_\phi\} = \{P_w\} \quad (3.109)$$

and

$$\{W_\phi\} = [K_\phi]^{-1} \{P_\phi\} - [K_\phi]^{-1} [K_{\phi w}]\{W\} \quad (3.110)$$

Equations (3.109) and (3.110) resemble the actuator and sensor equations found in the literature; however, since the electrical DOF $\{W_\phi\}$ is a primary variable and is inherently coupled to the applied voltage and structural displacement $\{W\}$ further simplification is required. Given the inherent coupling Eq. (3.110) must be substituted into (3.109) resulting in

$$[M]\{\ddot{W}\} + ([K_w] + [K_s] - [K_{w\phi}][K_\phi]^{-1}[K_{\phi w}])\{W\} = \{P_w\} - [K_{w\phi}][K_\phi]^{-1}\{P_\phi\} \quad (3.111)$$

Now, Eq. (3.111) represents the true actuator equation since the secondary variables contain nodal forces and applied actuator voltages. The solution of Eq. (3.111) yields structural deformation due to applied nodal forces and actuation voltages. However, if the piezoceramic is used for structural sensing only, then the applied actuation voltage, the secondary variable, $\{P_\phi\}$, is zero, leaving the primary nodal variable, $\{W_\phi\}$, (the electrical nodal DOF) intact, resulting in the following coupled equations:

$$[M]\{\ddot{W}\} + ([K_w] + [K_s] + [K_{w\phi}][K_\phi]^{-1}[K_{\phi w}])\{W\} = \{P_w\} \quad (3.112)$$

and

$$\{W_\phi\} = -[K_\phi]^{-1}[K_{\phi w}]\{W\} \quad (3.113)$$

The sensor equation shown in Eq. (3.113) provides the nodal voltage due to the structural response given the nodal structural loading of Eq.(3.112). Therefore, the actuator and sensor equations maintain the fully coupled mixed field formulation since the structural properties of the piezoceramic are retained. The global equations of motion of may be solved simultaneously by maintaining that the electrical nodal DOF represents a sensor and actuator signal. The simultaneous sensing-actuation signal was exploited by and analog circuit developed by Dosch⁴⁴ *et al.* and through adaptive digital signal processing by Cole and Clark.⁴⁵

Finite Element Validation

The finite element natural frequencies for a completely clamped aluminum shell panel are compared to the Donnell-Mushtari⁴⁶ shell equations. The shell was 11 5/8" long with a radius of curvature $R=96"$ and a curved length of 9 5/8" with a thickness of 0.032". Mesh refinement was carried out to verify convergence to the analytical solution and are shown in Table 3.1. The Donnell-Mushtari natural frequency for the first mode is 314.4 Hz., and the finite element analysis converges to 316.5 Hz., which is in error of less than 0.5 %.

Table 3.1 Finite Element Convergence

Finite Element Analysis	
Mesh	Frequency of Mode 1 (Hz)
10x10x2	328.9
12x12x2	323.3
14x14x2	319.9
16x16x2	317.9
18x18x2	316.5

Numerical Examples of a Curved Panel With MFC

The triangular shell element facilitates arbitrary placement of anisotropic MFC piezoceramic transducers on the structure. For example, not only does the transducer location become important, the rotation angle of the MFC principal axes also becomes a factor. The finite element model incorporates the MFC transducer concept utilizing rectangular PZT-5A fiber properties. Figure 3.4 indicates the placement of the MFC transducer on a curved panel modeled with triangular shell elements.

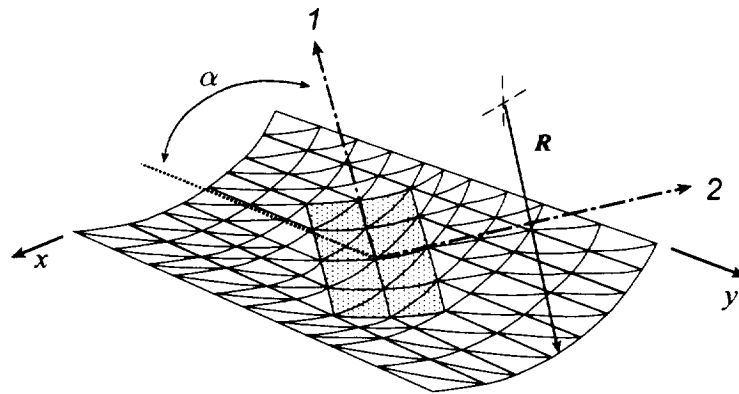


Figure 3.4 MFC Finite Element Mesh

To investigate the effect of the angle of orientation of the MFC actuator on structural vibration control, an aluminum 10"x14"x0.040" curved panel with radius of curvature $R=96$ " and a 2"x4"x0.010" MFC actuator located at the panel center was modeled with 144 triangular elements for several orientation angles and compared to a similar panel using a traditional 2"x4"x0.010" PZT-5A actuator. The finite element mesh is shown in Figure 3.4. The triangular elements are arranged with eight rectangles in the x direction and ten rectangles in the y as shown in Figure 3.5. The finite element mesh is adaptively updated for each orientation angle α .

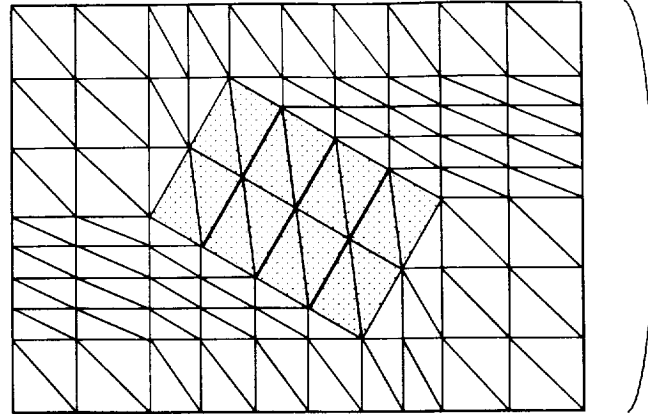


Figure 3.5 MFC Curved Finite Element Mesh

The electrical and mechanical material properties for the piezoceramic used are shown in Table 3.2. The MFC properties were provided by NASA Langley Research Center.⁴⁷ Note that the PZT-5A uses d_{31} values in lieu of d_{11} as previously described. The mechanical properties of the MFC transducer were determined using micromechanical analysis using representative volume fractions since it has not been extensively tested to determine all of the mechanical properties. However, the piezoceramic strain coefficients were experimentally determined using actual MFC actuators.

Table 3.2 Piezoceramic Properties

	MFC	PZT-5A
d_{11} (m/V)	450e-12	171e-12
d_{12} (m/V)	-210e-12	171e-12
E_1 (N/m ²)	36.5e9	69e9
E_2 (N/m ²)	7.5e9	69e9
ρh (Kg/m ²)	1.937	1.96

To evaluate the MFC actuator compared to traditional PZT-5A, an LQR feedback controller was developed using the finite element model as the dynamic plant and a single

piezoceramic actuator to minimize the curved panel vibration. The actuator was placed at the center of a cylindrical shell structure, as shown in Figure 3.4. The open and closed loop transfer function of velocity per force at a point located at the center of the panel were determined for orientation angles of 5, 15, 25, 35, 45, 55, 65, and 75 degrees for a traditional PZT and a MFC actuator. Even though a voltage is applied to the actuator, a force is applied to the structure as shown in the right hand side of the coupled finite element actuator equation in Eq. (3.111). Figures 3.6-3.13 provide the velocity per force transfer function for each angle comparing the MFC and traditional actuators.

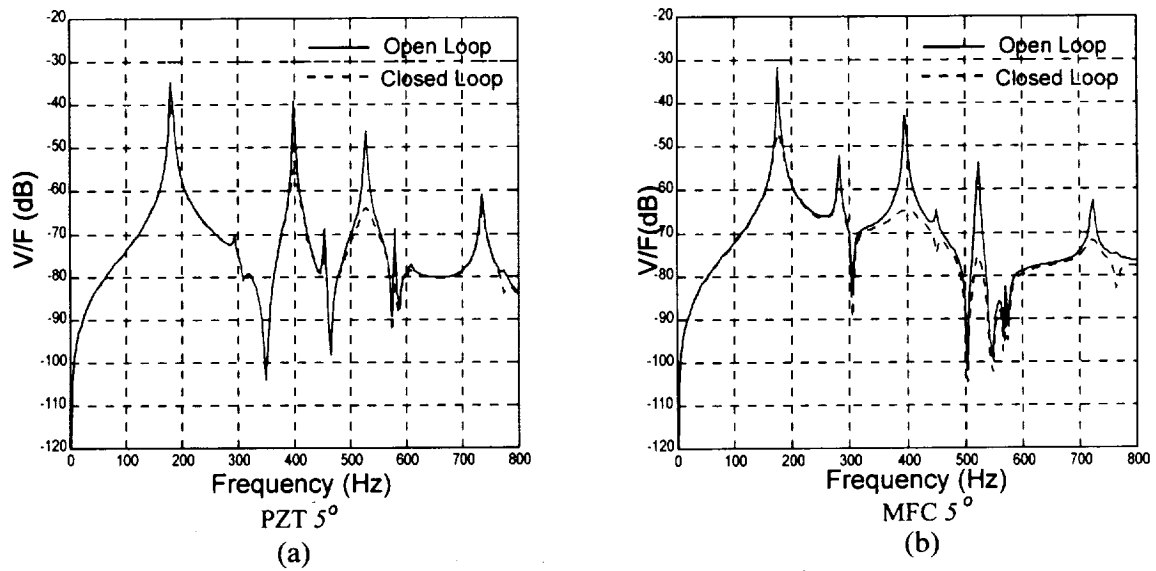
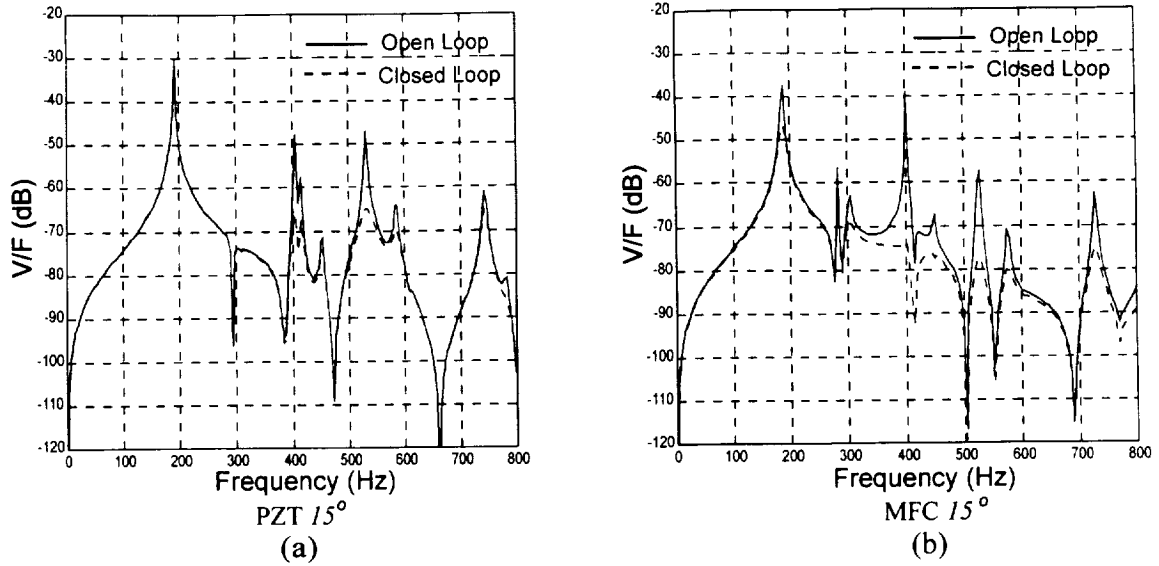
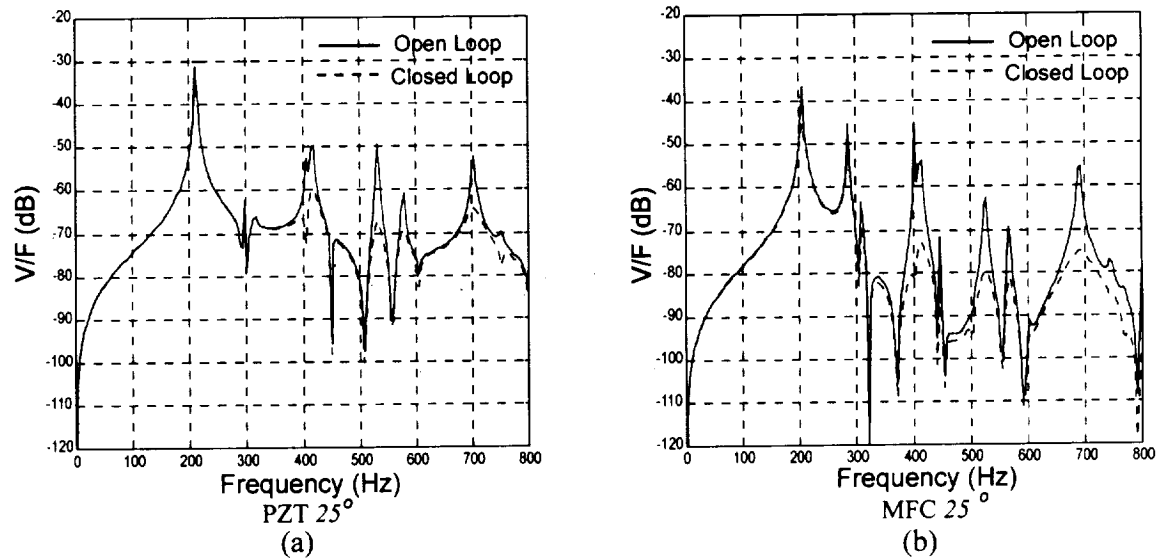


Figure 3.6 MFC and PZT for 5°

The MFC actuator provides better control authority for both 5 and 15 degrees, as shown in Figures 3.6 and 3.7. However, the structural dynamics of the shell are influenced due to the inherent anisotropic material properties of the MFC actuator.

Figure 3.7 MFC and PZT for 15°

Similarly, MFC performs better than the traditional PZT for 25 and 35 degree rotation angle, as shown in Figures 3.8 and 3.9. Both the PZT and MFC actuator were 0.010" thick.

Figure 3.8 MFC and PZT for 25°

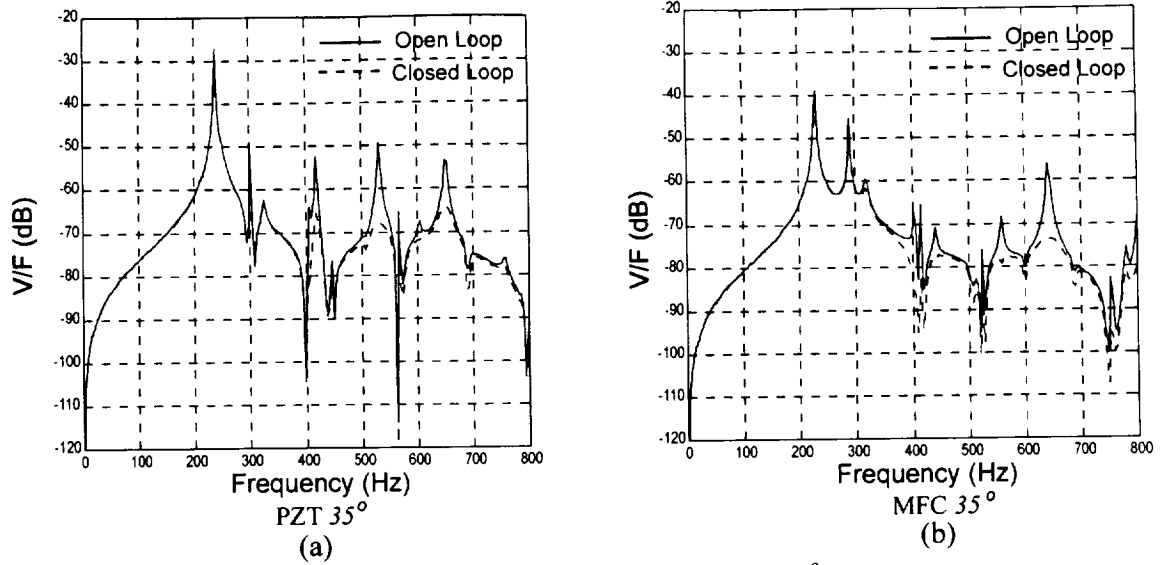


Figure 3.9 MFC and PZT for 35°

The structural dynamics of the MFC curved panel were significantly different than that of PZT curved panel for the 45 degree angle. However, the PZT actuator performs better than the MFC, especially for higher modes, as shown in Figure 3.10.

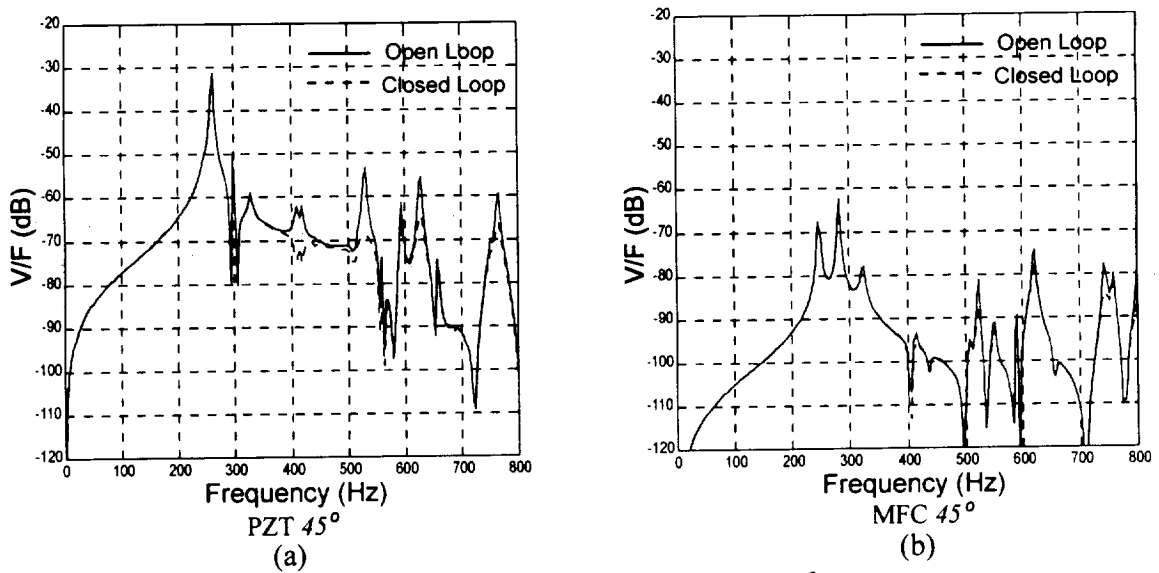


Figure 3.10 MFC and PZT for 45°

The MFC actuator performs better than the PZT for 55, 65, and 75 degrees, as shown in Figures 3.11-3.13. Since the dynamics differ significantly in some cases, this evaluation may not provide a fair evaluation. However, the comparison does provide significant insight into the benefits of using MFC actuators for structural vibration control.

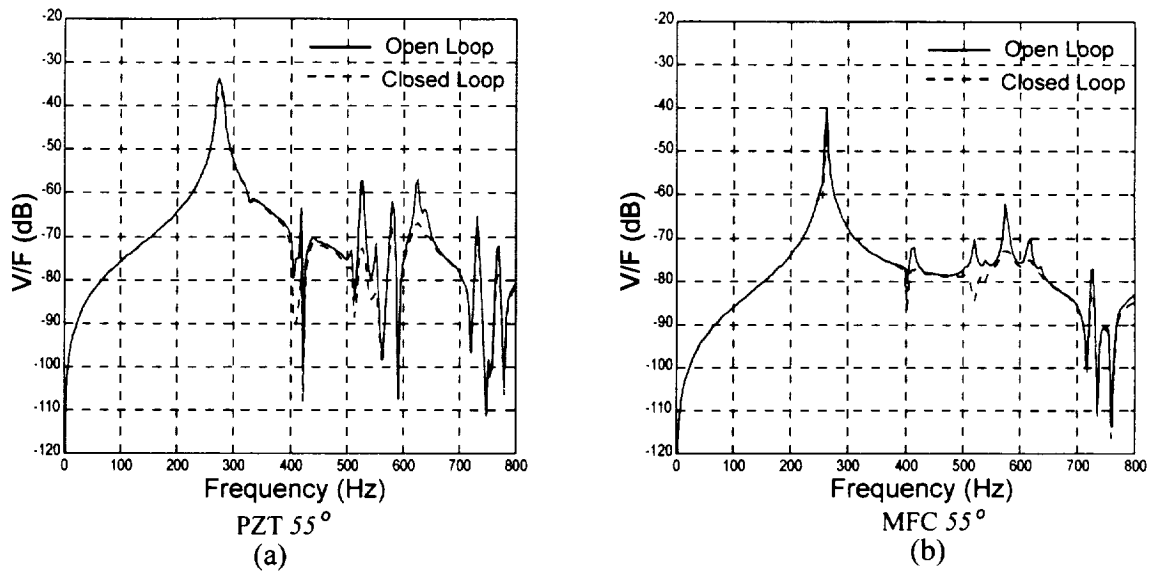


Figure 3.11 MFC and PZT for 55°

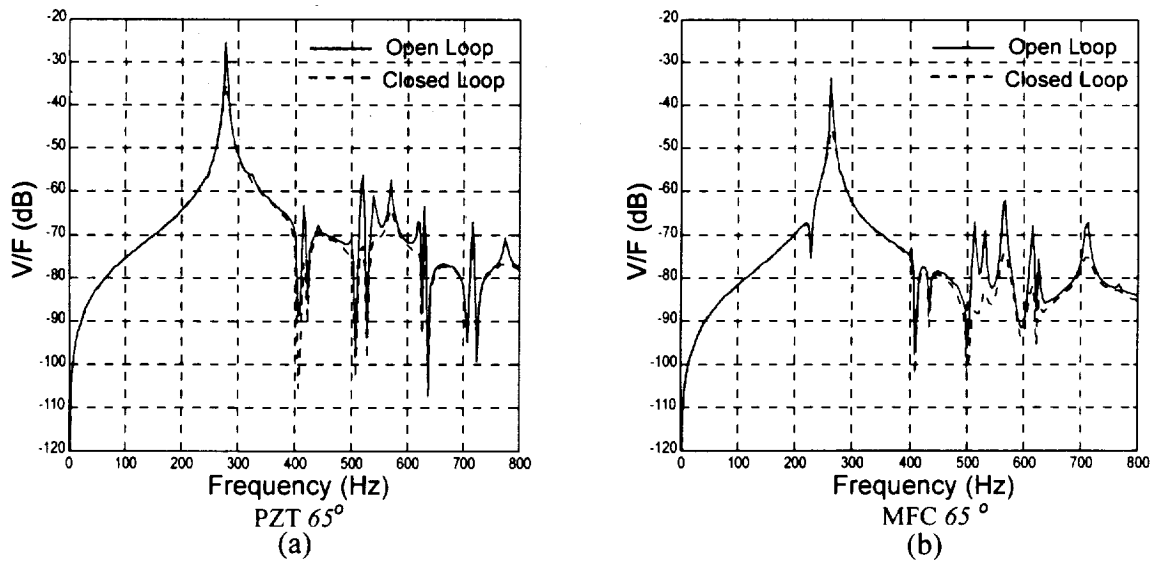


Figure 3.12 MFC and PZT for 65°

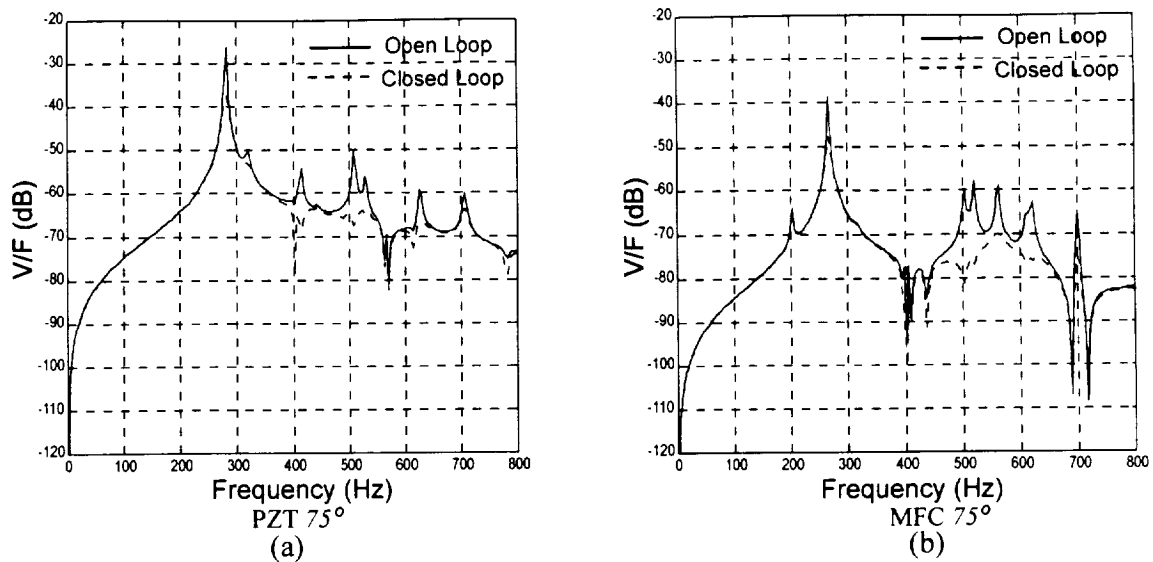


Figure 3.13 MFC and PZT for 75°

The analytical results presented for MFC actuators suggest that enhanced control performance is achievable over traditional PZT actuators. However, the results also indicate that the structural dynamics may be modified significantly by including the anisotropic actuator material properties. Therefore, to obtain optimum performance, increased control authority, placement, and orientation angle must be considered when designing smart structures. By introducing multiple actuators with different orientation angles, the performance may be greatly enhanced. Furthermore, it is recommended that experimental mechanical properties be obtained for representative MFC transducers to ensure accurate modeling.

In any event, the transfer functions shown may not provide sufficient information to evaluate MFC actuators regarding structural acoustic control. To this end, additional analytical simulation results are provided in APPENDIX A for curved and flat panel.

CHAPTER IV

STRUCTURAL ACOUSTICS

Introduction

The concept of active structural acoustic control (ASAC) emphasizes control of selected structural surface vibrations that contribute directly to the far field radiated acoustic energy. In contrast, active vibration control (AVC) solely addresses reduction of surface vibration regardless of acoustic implications. Hence, identifying structural vibration characteristics that contribute directly to the acoustic radiation becomes prudent.

An arbitrarily vibrating structure consists of an infinite sum of the natural vibration mode shapes corresponding natural frequencies. Upon examination, the mode shapes exhibit characteristics that relate their importance to acoustic radiation efficiency. Intuitively, this concept can be visualized by considering mode shapes of a baffled plate structure. Boundary conditions only affect the absolute natural frequencies and specific mode shapes but not the conceptual argument.

Suffice it to say that, relative to the acoustic wavelength, the geometry yields an infinite baffled planar structure. The fundamental mode shape yields a domed shape, whereas the second mode approximately represents a sine wave along the major axis and a sine along the minor axis. If we visualize the behavior of a fluidic medium immediately in front of the vibrating surface, for the two distinct modes, radiation efficiency becomes evident. The fluid reacts quite differently to each mode shape. For example, in the case of the second mode, it is apparent that the fluid simply sloshes back and forth between each oscillating trough of the sine shape. The fundamental mode,

however, displaces the fluid outward virtually in-phase across the entire surface of the plate. Hence, fluid particles immediately in front of the plate will be transported farther away from the plate given sufficient time. The net fluid motion of the second mode remains transverse and never propagates far from the planar surface regardless of the amount of time. Thus, the fundamental mode efficiently transfers the surface vibration throughout the surrounding medium, while the second mode is a very inefficient mechanism to facilitate propagation of the surface vibration.

This example demonstrates the concept of radiation efficiency for single mode shapes; however, in general, structural modes do not radiate independently. In fact, the strong dependence on inter-modal coupling between structural modes affects the radiated power such that reducing dominant structural vibration modes may have little effect on the radiated sound power. In fact, by the reducing dominant structural vibration modes the radiated sound power may actually increase.

Pursuant to identifying structural acoustic radiation characteristics, researchers developed the concept of surface velocity filters, or acoustic radiation filters. Acoustic radiation filters describe radiated power in terms of discrete surface velocities and the surface radiation resistance as shown by Cunefare.⁴⁸ However, this concept can be described as a modal approach for characterizing acoustic radiation from vibrating structures. The term “modal” here refers to acoustic radiation modes and are independent of structural vibration modes. Furthermore, radiation modes should not be confused with acoustic cavity modes. Borgiotti and Jones¹⁶ first introduced a modal representation using Singular Value Decomposition (SVD) to represent radiation efficiencies and singular velocity patterns. Since the introduction of the modal description, many

researchers have investigated various aspects of radiation modes. For instance, Baumann, Saunders, and Robertshaw²³ implemented feedback control by using radiation filters in frequency weighted cost functions to minimize the most efficient radiating modes. Elliot and Johnson⁴⁹ implemented feedforward control of beams and plates using radiation filters. Gibbs²⁴ *et al.* developed a Radiation Modal Expansion technique, exploiting the acoustic radiation bounding properties, thereby reducing computational effort of radiation filters for real time digital signal processing applications.

In essence, the radiation filter concept is an orthogonal vector decomposition performed on a discretized radiation operator, dependant solely on the frequency range of interest and structural geometry. The acoustic radiation of a structure can be described by a functional, or radiation operator, which can be derived to incorporate the desired acoustic radiation physics. Radiation modes produced by orthogonal decomposition can best be described as a radiation space transformation, and the modes do not directly correspond to the more common structural vibration modes, nor should they be confused with traditional acoustic modes for enclosed volumes.

Acoustic Radiation Filters

The acoustic radiation filter concept can be understood by considering basic structural acoustic concepts. The Kirchhoff-Helmholtz integral equation describes sound radiation due to vibrating bodies. Pierce⁵⁰ derives this equation, and for simple harmonic motion, the acoustic pressure is as follows:

$$p(\vec{r})e^{j\omega t} = \frac{1}{4\pi} e^{j\omega t} \int_S \left\{ p(\vec{r}_s) \frac{\partial}{\partial n} \left(\frac{e^{-jkR}}{R} \right) + j\omega \rho_0 v_n(\vec{r}_s) \left(\frac{e^{-jkR}}{R} \right) \right\} dS \quad (4.1)$$

where $p(\bar{r})$ is the acoustic pressure at the vector position \bar{r} , $p(\bar{r}_s)$ is the pressure near the surface at vector position \bar{r}_s , $R = |\bar{r} - \bar{r}_s|$, the normal surface velocity is $v_n(\bar{r}_s)$, and the fluid density is ρ_o . Clearly, the acoustic pressure is due to both the pressure and velocity of the vibrating surface.

For typical vibrating structures, the solution of Eq. (4.1) is difficult and is usually approached using numerical methods. However, by considering a vibrating planar surface bounded by an infinite half-space, a more tractable solution exists, as shown by Fahy⁵¹. The acoustic pressure from a vibrating planar surface within an infinite half-space is described by

$$p(\bar{r})e^{j\omega t} = \frac{j\omega\rho_o}{4\pi} \int_S \left\{ 2v_n(\bar{r}_s) \left(\frac{e^{-jkR}}{R} \right) \right\} dS \quad (4.2)$$

Thus, the vibrating surface can be considered as a differential area representing a point source of strength $2v_n dS$. Expressing the planar vibration response in modal coordinates, Eq. (4.2) becomes

$$p(\bar{r})e^{j\omega t} = \frac{j\omega\rho_o}{2\pi} e^{j\omega t} \int_0^a \int_0^b \left\{ \sum_{n=1}^{\infty} v_n \varphi_n(x, y) \left(\frac{e^{-jkR}}{R} \right) \right\} dx dy \quad (4.3)$$

where v_n and $\varphi_n(x, y)$ are the velocity and mode shape of the n^{th} mode. By introducing the definition of acoustic radiation efficiency, further insight may be gained and applied to the development of the acoustic radiation filters.

The ratio of the average acoustic power radiated due to surface vibration to that of an equivalent piston defines radiation efficiency. The piston infers that the radiating area is small relative to the acoustic wavelength and that the velocity is uniform across its surface. Hence, radiation efficiency is expressed as

$$\hat{\sigma} = \frac{\bar{P}}{\rho_o c S \langle \bar{v}_n^2 \rangle} \quad (4.4)$$

where $\langle \bar{v}_n^2 \rangle$ is the averaged mean-square normal velocity, \bar{P} is the time averaged power, and S represents surface area, c velocity of sound in the medium.

Next, recall the acoustic intensity is defined as the product of pressure and velocity hence the time averaged intensity can be expressed as

$$I(r, \theta, \phi) = \frac{1}{T} \int_0^T p(r, \theta, \phi, t) v(r, \theta, \phi, t) dt \quad (4.5)$$

where (r, θ, ϕ) represents the spherical coordinates of a field point within an infinite half-space. In the far field, the surface integral of the intensity represents the time averaged radiated power and is expressed as

$$\bar{P} = \int_0^\pi \int_0^{2\pi} I(r, \theta, \phi) r^2 \sin \theta d\theta d\phi \quad (4.6)$$

Since the pressure and velocity of a plane wave are related through the characteristic impedance as $\rho_o c = \frac{p(r, \theta, \phi, t)}{v(r, \theta, \phi, t)}$, the intensity in Eq. (4.5) can be expressed in terms of the pressure only. The average power in Eq. (4.6) now becomes

$$\bar{P} = \int_0^\pi \int_0^{2\pi} \left[\frac{1}{T} \int_0^T \frac{p^2(r, \theta, \phi, t)}{\rho_o c} dt \right] r^2 \sin \theta d\theta d\phi \quad (4.7)$$

The modal formulation for the pressure shown in Eq. (4.3) can be substituted into the radiated power expression of Eq. (4.7). Utilizing the far field assumption $R \approx r - x \sin \theta \cos \phi - y \sin \theta \sin \phi$, Eq. (4.3) may be simplified as

$$p(\vec{r}) = \frac{j\omega\rho_o}{2\pi r} e^{-jkr} e^{j\omega t} \int_0^a \int_0^b \left\{ \sum_{n=1}^{\infty} v_n \varphi_n(x, y) e^{jk \sin \theta \cos \phi x + jk \sin \theta \cos \phi y} \right\} dx dy \quad (4.8)$$

Furthermore, the squared pressure in terms of the velocity and structural mode shapes can be expressed as

$$|p(\vec{r})|^2 = \frac{\omega^2 \rho_o^2}{4\pi^2 r^2} \sum_{r=1}^{\infty} v_r H_r(\theta, \phi, \omega) \sum_{s=1}^{\infty} v_s H_s(\theta, \phi, \omega) \quad (4.9)$$

where $H(\theta, \phi, \omega) = \int_0^a \int_0^b v \varphi(x, y) e^{jk \sin \theta \cos \phi x + jk \sin \theta \cos \phi y} dx dy$. Substituting Eq. (4.9) into Eq.

(4.7) produces an expression for the far field radiated power of a vibrating structure as a function its surface velocity. Thus, the radiated power is expressed as

$$\bar{P}(j\omega) = \frac{\omega^2 \rho_o}{4\pi^2 c} \{v\} [M] \{v\}^h \quad (4.10)$$

where

$$[M] = \int_0^\pi \int_0^{2\pi} [H][H]^h \sin \theta d\theta d\phi \quad (4.11)$$

Comparing Eqs. (4.4) and (4.10), we note that the frequency dependant radiation matrix $[M]$ is proportional to the radiation efficiency and describes the structural acoustic interaction of the structural modes.⁵² Specifically, the diagonal terms represent the self-radiation efficiencies and the off diagonal terms indicate mutual radiation efficiencies. Hence, the $[M]$ matrix is termed the coupling matrix since it provides information on the structural modal coupling to the acoustic radiation modes. An important result of the above derivation is that the far field radiated acoustic power can be determined from the modal velocities and radiation matrix $[M]$, thus eliminating the field pressure from the power expression. Furthermore, the radiation matrix $[M]$, or

acoustic impedance is positive definite and Hermitian. In general, this matrix operator can be determined using the Helmholtz integral for three-dimensional bodies, or by Rayleigh's integral for planar baffled structures.

Planar Radiation Resistance

Elliott and Johnson⁴⁹ derived the radiation resistance matrix of a planar baffled structure comprised of elemental radiators. It is assumed that the acoustic pressure and normal surface velocity are constant over each elemental radiator. This requires that the size of the elemental radiator be much less than the acoustic wavelength. Furthermore, it is assumed that the structure is radiating into free-space. The acoustic transfer impedance from an infinite baffled radiator is given by⁵⁰

$$z(x, y) = \frac{p(y)}{v(x)} = \frac{j\omega\rho_o S}{2\pi r} e^{-jkr} \quad (4.12)$$

where $k = \omega/c$ is the wave number and S the elemental area. The element of the corresponding radiation resistance matrix $[M]$ in Eq. (4.11), is determined by applying Eulers identity to Eq. (4.12) yielding

$$\frac{S}{2} \text{Re}[z(x, y)] = \frac{\omega\rho_o S^2}{4\pi r} \sin kr = \frac{\omega^2 \rho_o S^2}{4\pi c} \left(\frac{\sin kr}{kr} \right) \quad (4.13)$$

For an array of n radiator elements the radiation matrix becomes

$$[R] = \frac{\omega^2 \rho_o S^2}{4\pi c} \begin{bmatrix} 1 & \frac{\sin kr_{12}}{kr_{12}} & \dots & \frac{\sin kr_{1n}}{kr_{1n}} \\ \frac{\sin kr_{21}}{kr_{21}} & 1 & & \vdots \\ \vdots & & \ddots & \frac{\sin kr_{(n-1)n}}{kr_{(n-1)n}} \\ \frac{\sin kr_{n1}}{kr_{n1}} & \dots & \frac{\sin kr_{n(n-1)}}{kr_{n(n-1)}} & 1 \end{bmatrix} \quad (4.14)$$

where r_{ij} is the distance between the i^{th} and j^{th} radiator elements. Notice that the radiation resistance matrix is dependant on frequency and geometry only. The radiation resistance matrix of Eq. (4.14) is valid for flat planar structures of arbitrary shape.

Curved Panel Radiation Operator

So far, only planar baffled structures were considered for acoustic radiation filter development using the Rayleigh integral; however, since a cylindrical shell is of particular interest in this research, the Helmholtz integral equation will be investigated. To develop radiation filters for shell configurations, the surface radiation impedance formulation is developed for a vibrating structure of arbitrary shape radiating into free-space. The formulation utilizes a discretization of Kirchhoff-Helmholtz integral as developed by Koopman and Benner⁵³ to determine radiated sound power of machines.

Consider an arbitrary radiating closed surface as shown in Figure 4.1 the pressure at point \bar{R} can be expressed with the following Kirchhoff-Helmholtz integral equation⁵⁴

$$p(\bar{R}) = -\frac{1}{2\pi} \int_S p(\bar{R}_o) \frac{e^{jk r}}{r} \left(\frac{1}{r} - jk \right) \cos \gamma dS(\bar{R}_o) - \frac{j\omega\rho_o}{2\pi} \int_S \dot{w}(\bar{R}_o) \frac{e^{jk r}}{r} dS(\bar{R}_o) \quad (4.15)$$

where $r = |\bar{R} - \bar{R}_o|$ is the distance between the two points on the surface S .

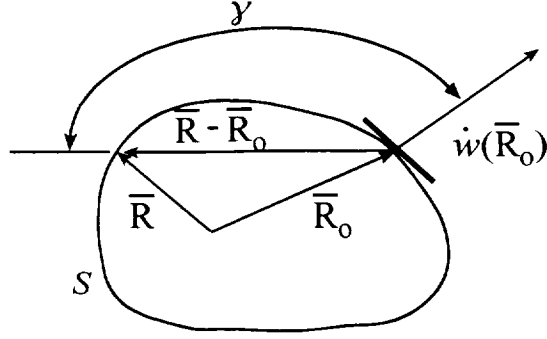


Figure 4.1 Vibrating Surface Geometry

If the surface S is approximated by n planar elements then the three-dimensional arbitrary surface integration reduces to integration over a two-dimensional element surface. The requisite number of elements may be determined such that the pressure and velocity be uniform over each element. For convenience, the Kirchhoff-Helmholtz integral in Eq. (4.15) may be expressed in non-dimensional form as

$$p(\bar{R}) = \frac{-jk\mathcal{L}}{2\pi} \int_a p(\bar{R}_o) \frac{e^{jkr}}{(r/\mathcal{L})} \left(\frac{1}{kr} - j \right) \cos \gamma da(\bar{R}_o) - \frac{jk\mathcal{L}}{2\pi} \int_a v(\bar{R}_o) \frac{e^{jkr}}{(r/\mathcal{L})} da(\bar{R}_o) \quad (4.16)$$

where $v = \dot{w}/\dot{w}_c$ is a dimensionless surface velocity normalized to an arbitrary constant \dot{w}_c , $r = |\bar{R} - \bar{R}_o|$ is the magnitude of the distance between two radiating elements on the structure, $a = S/\mathcal{L}^2$ is the dimensionless element area, \mathcal{L} represents an element length, and $p = p/\rho_o c \dot{w}_c$ is the dimensionless acoustic pressure. Assuming a finite element discretization is applied to a radiating surface S , resulting in n planar elements, Eq. (4.16) can be expressed in indicial form as

$$p(\bar{R}_i) = p(\bar{R}_j) D_{ij} + u(\bar{R}_j) M_{ij} \quad (4.17)$$

The dipole coefficient, or mutual pressure interaction between the i^{th} and j^{th} elements is given as

$$D_{ij} = \frac{-k\mathcal{L}}{2\pi} \int_{a_j} \frac{e^{jk r_{ij}}}{(r_{ij}/\mathcal{L})} \left(\frac{1}{kr_{ij}} - \mathbf{j} \right) \cos \gamma_{ij} da_j \quad (4.18)$$

The relationship between the normal velocity of the j^{th} element and pressure on the i^{th} element is coupled by a monopole coefficient defined as

$$M_{ij} = \frac{-\mathbf{j}k\mathcal{L}}{2\pi} \int_{a_j} \frac{e^{jk r_{ij}}}{(r_{ij}/\mathcal{L})} da_j \quad (4.19)$$

where r_{ij} is the magnitude of the vector from the reference point of element i to element j , γ_{ij} is the angle between the outward normal of element j and r_{ij} . Note that for a planar radiating structure the dipole coefficient $D_{ij} = 0$ since $\gamma_{ij} = \pi/2$. Furthermore, Eq. (4.19) becomes $M_{ij} = \frac{-\mathbf{j}\omega S}{2\pi c r_{ij}} e^{-jk r_{ij}}$ which upon substitution into Eq. (4.17) yields

$$\frac{p_i}{v_j} = \frac{\mathbf{j}\omega \rho_o S}{2\pi r_{ij}} e^{-jk r_{ij}} \quad (4.20)$$

Thus, Eq. (4.20) is identically equal to the radiation impedance of the planar radiator defined in Eq. (4.12). The surface pressure may be determined by the solution of the following system of $n \times n$ linear inhomogeneous equations

$$([I] - [D])\{p\} = [M]\{v\} \quad (4.21)$$

In Eq. (4.21), the terms in the dipole matrix will reduce to zero if the structure is planar. However, for a non-planar surface Eq. (4.21) may be written as

$$\{p\} = [A]^{-1} [M]\{v\} \quad (4.22)$$

where $[A] = ([I] - [D])$. Thus, the matrix product of $[A]^{-1} [M]$ represents the Helmholtz surface radiation impedance. In order to determine the radiation resistance, or the real part of the impedance, the monopole and dipole coefficients may be simplified as

follows. The monopole coefficient shown in Eq. (4.19) may be expanded by using Euler's formula yielding

$$M_y = \frac{-jk\mathcal{L}}{2\pi} \int_{a_j} \frac{1}{r_y/\mathcal{L}} (\cos kr_y + j \sin kr_y) da_j$$

$$\text{Re}(M_y) = \frac{\omega^2 \mathcal{L}^2 a_j}{2\pi c^2} \left(\frac{\sin kr_y}{r_y} \right)$$
(4.23)

Similarly, the dipole coefficient shown in Eq.(4.18) may be expanded yielding

$$D_y = \frac{-k\mathcal{L}^2}{2\pi r_y} \int_{a_j} \cos \gamma_y \left(\frac{\cos kr_y}{kr_y} + \sin kr_y + j \frac{\sin kr_y}{kr_y} - j \sin kr_y \right) da_j$$

$$\text{Re}(D_y) = -\frac{\omega^2 \mathcal{L}^2 a_j}{2\pi c^2} \left(\frac{\cos kr_y}{(kr_y)^2} + \frac{\sin kr_y}{kr_y} \right) \cos \gamma_y$$
(4.24)

In matrix equation notation, the radiation matrix can be noted as

$$[R] = ([I] - [D])^{-1} [M]$$
(4.25)

where the dipole and monopole matrices are defined as

$$[D] = \frac{\omega^2 \mathcal{L}^2 a}{2\pi c^2} \begin{bmatrix} 0 & \left(\frac{\cos kr_{12}}{(kr_{12})^2} + \frac{\sin kr_{12}}{kr_{12}} \right) \cos \gamma_{12} & \cdots & \left(\frac{\cos kr_{1n}}{(kr_{1n})^2} + \frac{\sin kr_{1n}}{kr_{1n}} \right) \cos \gamma_{1n} \\ \left(\frac{\cos kr_{21}}{(kr_{21})^2} + \frac{\sin kr_{21}}{kr_{21}} \right) \cos \gamma_{21} & 0 & \ddots & \vdots \\ \vdots & \ddots & \ddots & \left(\frac{\cos kr_{(n-1)n}}{(kr_{(n-1)n})^2} + \frac{\sin kr_{(n-1)n}}{kr_{(n-1)n}} \right) \cos \gamma_{(n-1)n} \\ \left(\frac{\cos kr_{n1}}{(kr_{n1})^2} + \frac{\sin kr_{n1}}{kr_{n1}} \right) \cos \gamma_{n1} & \cdots & \cdots & 0 \end{bmatrix}$$
(4.26)

$$[M] = \frac{\omega^2 \mathcal{L}^2 a}{2\pi c^2} \begin{bmatrix} 1 & \frac{\sin kr_{12}}{kr_{12}} & \dots & \frac{\sin kr_{1n}}{kr_{1n}} \\ \frac{\sin kr_{21}}{kr_{21}} & 1 & \ddots & \vdots \\ \vdots & \ddots & \ddots & \frac{\sin kr_{(n-1)n}}{kr_{(n-1)n}} \\ \frac{\sin kr_{n1}}{kr_{n1}} & \dots & \dots & 1 \end{bmatrix} \quad (4.27)$$

Thus, the radiated power of a curved surface can be determined from the surface velocities by substituting the radiation resistance matrix of Eq. (4.25) into Eq. (4.10). A curved panel meshed with triangular finite elements representing discrete radiating piston at the element centroids is shown in Figure 4.2.

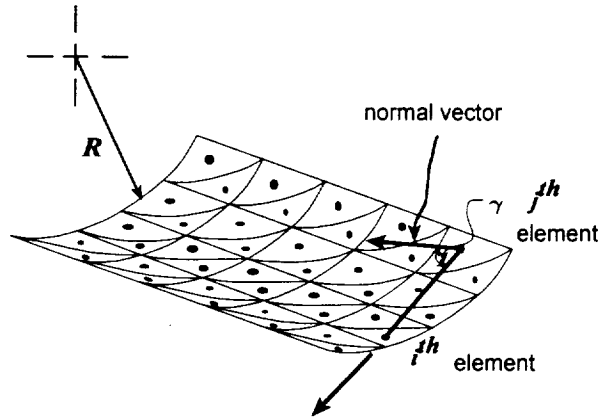


Figure 4.2 Curved Panel Finite Element Geometry

The panel radiates into an infinite free half-space from the convex side, and it is considered to be infinitely baffled. Since the most significant radiation modes are of concern for ASAC, edge constraints at the boundaries have little effect⁵⁵. The radiation efficiencies demonstrate a linear relationship for long wavelengths ($k\mathcal{L} > 1$) when plotted on a logarithmic scale with dependence on wavenumber to even integer powers.⁵⁶

The approximate dominant radiation efficiencies obtained using radiation modal expansion²⁴ are shown in Figure 4.3 for a 10"x14" rectangular curved panel with radius of curvature $R=40$ " along the major axis. Note that the singular points shown in Figure 4.3 arise from Eq. (4.26). When $i=j$, then $\cos \gamma_u = 0$ and $D_{ij}=0$, while the monopole coefficients become

$$M_{ij} = \begin{cases} \frac{\omega^2 \mathcal{L}a}{2\pi c^2} & \text{for } i = j \\ 0 & \text{for } i \neq j \end{cases} \quad (4.28)$$

However, when the source and receiving radiators are near each other the dipole coefficients approach zero, resulting in an ill-conditioned matrix inversion while the monopole coefficient matrix remains valid.

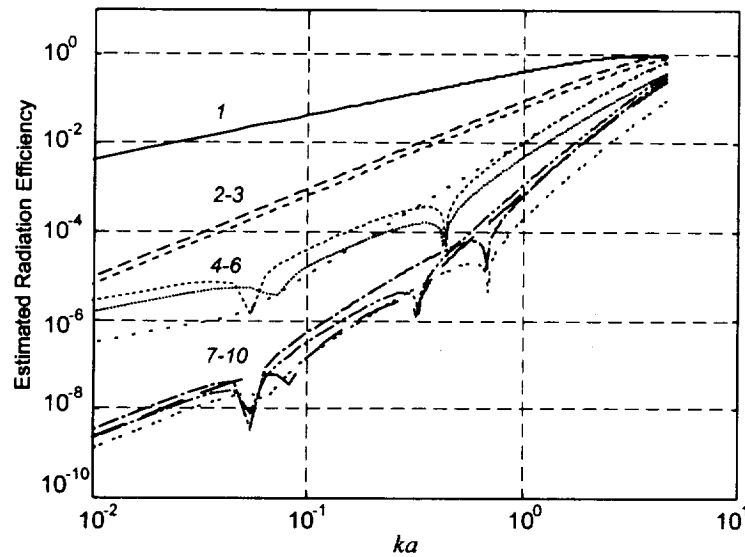


Figure 4.3 Curved Panel Using Triangular Acoustic Radiators

The approximate dominate radiation efficiencies for a flat panel with the same dimensions ($R=\infty$) are shown in Figure 4.4. The grouping characteristics of the

dominant radiation modes follow the same trend for both the flat and curved panels, as expected since both represent the approximate radiation in to an infinite half-space.

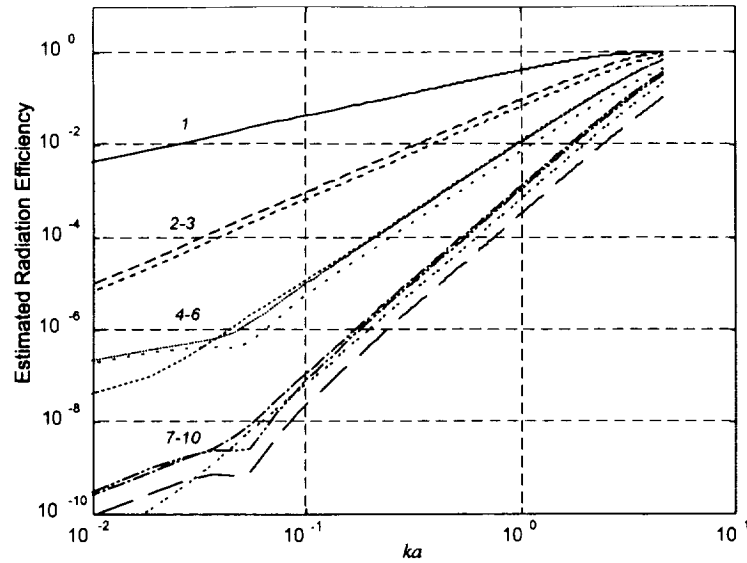


Figure 4.4 Flat Panel Using Triangular Acoustic Radiators

Furthermore, to validate the discrete triangular acoustic radiator approach the estimated radiation efficiencies were calculated using rectangular radiators following Gibbs.²⁴ Figure 4.5 indicates excellent agreement between the two methods.

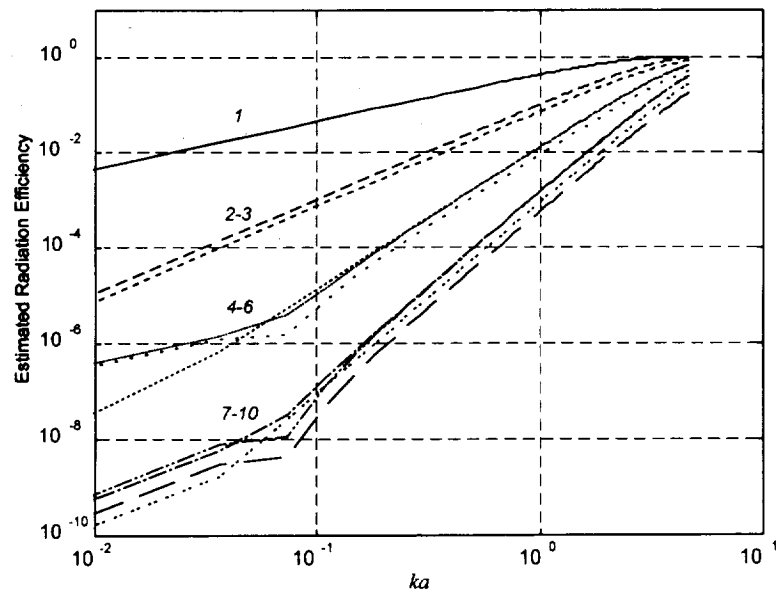


Figure 4.5 Flat panel Using Rectangular Acoustic Radiators

If the dominant radiation efficiencies are plotted as magnitude versus frequency then the frequency dependant amplitude becomes apparent. The radiation efficiency of the dominant radiation modes of the curved panel is shown in Figure 4.6. For comparison the dominant radiation efficiencies of a flat panel are shown in Figure 4.7. The curved panel exhibits lower radiation efficiencies for the radiation modes above 150 Hz., as expected, given increased panel stiffness due to the curvature.

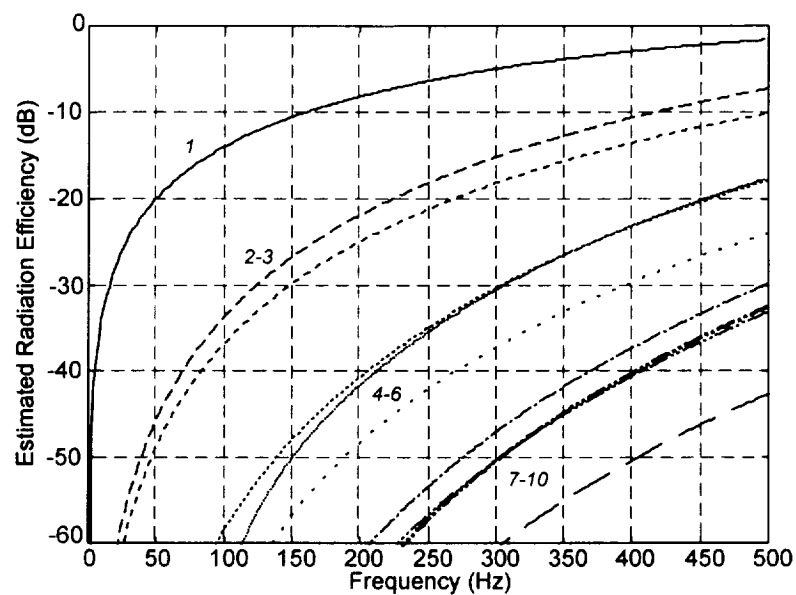


Figure 4.6 Curved Panel With Triangular Acoustic Radiators

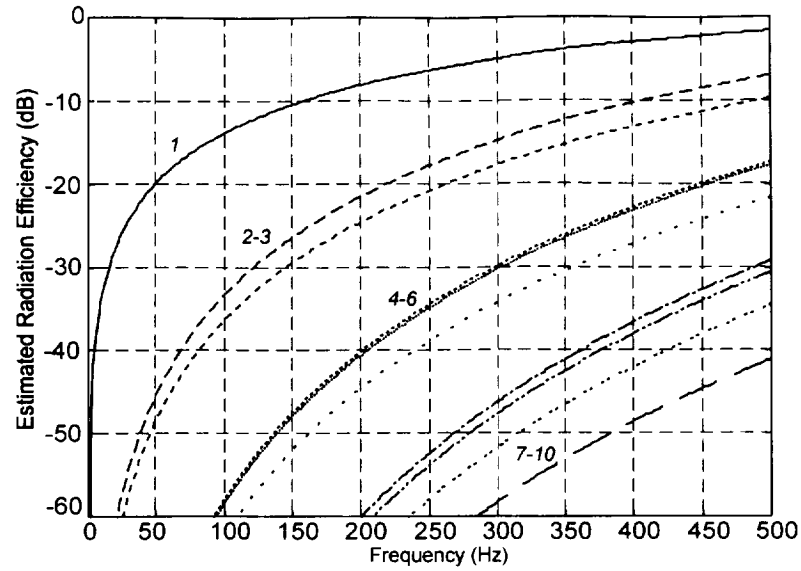


Figure 4.7 Flat Panel With Triangular Acoustic Radiators

The radiation filters developed will be implemented in the state-space representation and included in the analytical model to compute the structurally radiated sound power. They are also implemented within the real time DSP control algorithm to compute the structurally radiated sound power using discrete panel acceleration measurements. By implementing radiation filters a causal system exist since the acoustic radiated power is determined from structural vibration measurements.

CHAPTER V

FEEDBACK CONTROL AND PIEZOCERAMIC

ACTUATOR PLACEMENT

Introduction

Feedback control uses dynamic signal information obtained from sensors located on the structure for utilization by the controller to generate a signal that is applied to the structure through actuators. Controller design is based on minimizing a specified performance criterion, or cost function. The cost functional may include a control effort penalty, structural vibration state, an acoustic sound field condition, or as in this research structurally radiated noise levels. The feedback control method implemented in this research is the linear quadratic regulator (LQR) augmented to include acoustic radiation filters, thus yielding a cost function that minimizes structurally radiated power.

Finite Element State-Space Representation

The dynamic plant model used to represent the structure is determined from the finite element model. Thus, the finite element actuator equation shown in Eq. (3.111) can be written in modal coordinates as

$$\ddot{q}_r + 2\zeta_r\omega_r\dot{q}_r + \omega_r^2q_r = \frac{f_r}{m_r} - \frac{f_{r\phi}}{m_r} \quad (5.1)$$

where the modal coordinate transformation is defined as $\{W\} = [\Phi]\{q\}$, and q_r, ω_r, ζ_r are the r^{th} modal coordinate, natural frequency, and damping ratio, respectively. The modal mass, modal stiffness, and modal forces are obtained from

$$\begin{aligned}
\{\Phi\}_r^T ([M], [K]) \{\Phi\}_r &= (m_r, k_r) \\
[K] &= [K_w] - [K_{w\phi}] [K_\phi]^{-1} [K_{\phi w}] \\
\{\Phi\}_r^T \{P_w\} &= f_r \\
\{\Phi\}_r^T [K_{w\phi}] [K_\phi]^{-1} \{P_\phi\} &= f_{r\phi}
\end{aligned} \tag{5.2}$$

Equation (3.111) does not include a damping matrix. However, the damping values shown in Eq. (5.1) were determined experimentally.¹⁰

By defining a state vector as $\{x\} = [q \quad \dot{q}]^T$, the modal equations can be cast in state-space form as

$$\begin{aligned}
\{\dot{x}\} &= [A]\{x\} + [B]\{u\} \\
\{y\} &= [C]\{x\} + [D]\{u\}
\end{aligned} \tag{5.3}$$

The plant dynamic matrix $[A]$ is defined as

$$[A] = \begin{bmatrix} 0 & I \\ -[m]^{-1}[k] & -[m]^{-1}[c] \end{bmatrix} \tag{5.4}$$

The feedback matrix $[B]$ is defined as

$$[B] = \begin{bmatrix} 0 & 0 \\ [m]^{-1}[\Phi]^T & [m]^{-1}[\Phi]^T [K_{w\phi}] [K_\phi]^{-1} \end{bmatrix} \tag{5.5}$$

The output equation can be formulated by selecting an appropriate output matrix $[C]$.

Radiation Filter State-Space Representation

The frequency response information of the radiation filters can be exploited by curve fitting each radiation transfer function and including this information in the state-space model. The radiation-coupling matrix defined in Eqs. (4.14) and (4.25) provide amplitude-weighting coefficients proportional to the radiated power as a function of

frequency. Using the radiation modal expansion technique²⁴, the approximate radiated power coefficients can be determined from

$$\{\psi^2(\omega)\}_j = \{u(\omega_i)\}_j^H [R(j\omega)] \{u(\omega_i)\}_j, \quad (5.6)$$

where ω_i represents the single prescribed modal expansion frequency used to compute the radiation mode shapes. The approximate radiation modal expansion coefficients $\{\psi^2(\omega)\}$ are curve fitted as frequency response functions to represent the input-output relationship of an analog filter for each radiating mode. The constructed radiation filter includes the first three acoustic radiation modes. However, an eighth order polynomial was used to fit the six dominant acoustic radiation modes to validate the curve fit accuracy and are shown in Figure 5.1.

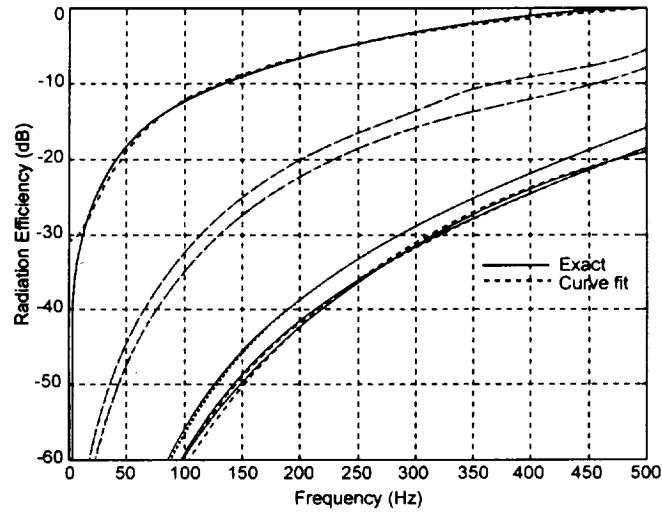


Figure 5.1 Approximate and Exact Radiation Efficiency

The polynomial coefficients are transformed into the filter zeros and poles and subsequently transformed into a state-space filter model for each desired acoustic radiation mode. Each radiation filter can be expressed in state-space form as

$$\begin{aligned}\{\dot{r}\} &= [A_f]\{r\} + [B_f]\{v\} \\ \{z\} &= [C_f]\{r\} + [D_f]\{v\}\end{aligned}\tag{5.7}$$

where $\{r\}$ represents the radiation state vector and $\{z\}$ corresponds to the acoustic radiated power due to the elemental radiator velocity $\{v\}$. Note that the filter input is the structural velocity and not the disturbance applied directly to the structure. The singular velocity vectors, or radiation mode shapes, are contained in the $[D_f]$ matrix. By incorporating radiation filters, an inherent state weighting is included for both the radiation and modal velocity states. Inclusion of the radiation filter is achieved by augmenting the structural state-space model with the radiation filter state-space model.

Structural Acoustic State-Space Representation

The state-space formulation easily permits construction of complex system models by specifying combinations of inputs, outputs, and state variables. Since the radiation filters derive their input from the structural response, an augmented state-space model represents the overall structural acoustic system. The augmented state-space system with acoustic radiated power as the output can be represented as

$$\begin{aligned}\begin{Bmatrix} \dot{x} \\ \dot{r} \end{Bmatrix} &= \begin{bmatrix} A & 0 \\ \bar{B}_f & A_f \end{bmatrix} \begin{Bmatrix} x \\ r \end{Bmatrix} + \begin{bmatrix} B \\ 0 \end{bmatrix} \{u\} + \begin{bmatrix} B_d \\ 0 \end{bmatrix} \{w\} \\ \{z\} &= [\bar{D}_f \quad C_f] \begin{Bmatrix} x \\ r \end{Bmatrix}\end{aligned}\tag{5.8}$$

where $\{w\}$ represents an acoustic disturbance, and the augmented state vector

$[\begin{bmatrix} x \\ r \end{bmatrix}]^T$ consists of the modal states $\{x\} = \{q \quad \dot{q}\}^T$ and the radiation states $\{r\}$.

Recall that the radiation filter formulation assumes a constant normal velocity for each elemental radiator. Therefore, the velocity vector $\{v\}$ in Eq. (5.7) is in physical

coordinates and not in modal coordinates. Since the finite element formulation uses a 4-node rectangular plate element, the modal coordinate transformation must be interpolated to obtain corresponding values at the center of each element. The $[\bar{D}_f]$ and $[\bar{B}_f]$ matrices are determined from

$$\begin{aligned} [\bar{D}_f] &= [D_f][\hat{\Phi}] \\ [\bar{B}_f] &= [B_f][\hat{\Phi}] \end{aligned} \quad (5.9)$$

where $[\hat{\Phi}]$ is the interpolated mode shapes at the center of each element. The radiated acoustic power $\{z\}$, shown in Eq.(5.8), includes contributions from both the modal velocity states and the radiation filter states.

To minimize the structural acoustic radiated power the following output-based functional was selected

$$J_{rad} = \int_0^{\infty} \left(\{z\}^T \{z\} + \{u\}^T [R] \{u\} \right) dt \quad (5.10)$$

where $[R]$ is a control effort penalty matrix and the acoustic radiated power incorporates the inherent frequency weighting of the radiation filters. Thus, minimizing the cost function achieves a trade off between the radiated power and control effort. If $[R]$ approaches zero then the cost function approaches the integral squared radiated power.

The standard linear quadratic state-based cost function includes a state weighting matrix $[Q]$ and is indicated as

$$J = \int_0^{\infty} \left(\{\mathcal{X}\}^T [Q] \{\mathcal{X}\} + \{\mathcal{U}\}^T [R] \{\mathcal{U}\} \right) dt \quad (5.11)$$

By expanding the first term in Eq.(5.10), it can be demonstrated that the radiation filters inherently define a state-weighting matrix as

$$\begin{aligned} \{z\}^T \{z\} &= \begin{bmatrix} x^T & r^T \end{bmatrix} \begin{bmatrix} \bar{D}_f^T \\ C_f^T \end{bmatrix} \begin{bmatrix} \bar{D}_f & C_f \end{bmatrix} \begin{Bmatrix} x \\ r \end{Bmatrix} \\ [Q] &\equiv \begin{bmatrix} \bar{D}_f^T \\ C_f^T \end{bmatrix} \begin{bmatrix} \bar{D}_f & C_f \end{bmatrix} \end{aligned} \quad (5.12)$$

Thus, the state weighting is equivalent to scaling both the modal velocity and the radiation state through the individual plant matrices $[C_f]$ and $[\bar{D}_f]$.

The state-space system defined in Eq. (5.8) is in the form of a standard linear quadratic regulator (LQR). The optimal control law is a linear time invariant state-feedback given as

$$\{u\} = -[K] \begin{Bmatrix} x \\ r \end{Bmatrix} \quad (5.13)$$

The feedback gain matrix $[K]$ is determined by solving the algebraic Riccati equation. However, since MATLAB[®] is used, the optimal gain matrix is determined using the *LQRY* command since it identically solves Eq. (5.10). Thus, a complete system utilizing the finite element model and acoustic radiation filters results in minimizing the structural acoustic radiation.

Genetic Algorithm Optimization

Pursuant to the objective of selecting optimum placement of two piezoceramic actuators to minimize structural radiated noise, an analytical model consisting of a coupled dynamic finite element model with, acoustic radiation filters, and LQR feedback control, is constructed and embedded within a genetic algorithm. Since the experiments conducted are performed on flat rectangular panels, the finite element formulation used a

modified high precision rectangular plate element.¹⁰ The original primary objective of this research focused on ASAC of curved panels. However, the funding agent, NASA Langley Research Center, supporting this research identified a need to address piezoceramic actuator placement on flat panels for ASAC.

Two traditional PZT-5A piezoceramic actuators of predetermined size are modeled with multiple finite elements and constrained from overlapping. If each piezoceramic actuator is placed on opposite sides of the panel, the overlapping constraint can be relaxed. However, this arrangement is not consistent with typical aerospace structures.

Each piezoceramic actuator location is indexed with integer values corresponding to the finite element mesh. A modified genetic algorithm with stochastic coding was selected since integer coding corresponds to the discrete actuator locations. The FT3PAK[®] and FlexGA[®] genetic algorithm by Flexible Intelligence Group⁵⁷ is used and operates in the MATLAB[®] environment. The genetic algorithm selects potential actuator locations that are subsequently used as input variables by the coupled finite element model to determine the closed loop acoustic radiation attenuation. The genetic algorithm can be configured to either minimize or maximize the performance index. Since the acoustic attenuation is defined as the actuator placement performance index, a maximization procedure is selected. Note that the genetic algorithm performance index is not the same cost function identified for determining the optimal feedback gains. For the genetic algorithm search, the performance index is identified as the overall structurally radiated sound power, which is to be reduced to a maximum extent.

The genetic algorithm search invokes an iterative process involving several steps. First, the finite element model is solved to provide a coupled dynamic plant model for the current actuator locations. Next, the optimal feedback gain is determined based on the acoustic radiation filters. Finally, the dynamic plant model is subjected to a uniform random acoustic plane wave disturbance source, indicated by $\{w\}$ in Eq. (5.8), and the structurally radiated sound power is calculated for both open and closed loop conditions.

The structurally radiated power is determined by computing the power spectrum density for the system output indicated in Eq. (5.8). For the open loop condition the control input $\{u\}$ vector in Eq. (5.8) is identically zero. The reduction in structurally radiated noise is determined by computing the difference of the real part of the open and closed loop power spectra. The iterative genetic algorithm process continues until a maximum acoustic radiation attenuation is achieved indicating the best actuator location.

To maximize computational efficiency several genetic algorithm models are constructed to determine actuator placement. These results are analyzed and then further studied using a refined finite element mesh without the genetic algorithm to determine the optimum actuator locations. Initially, a uniform 10x14 finite element mesh is used with the genetic algorithm to select actuator placement. Various actuator sizes considered included 1"x2", 1"x3", 2"x2", and 2"x3". Since 1"x3" piezoceramics were available for experimental testing, subsequent analysis was limited to this size.

A typical genetic algorithm graphical user display is shown in Figure 5.2 and portrays the fitness value, or performance index, versus number of functions evaluated along with the best, worst, and average fitness value versus the number of generations. Each generation provides the numerical location index for each actuator location.

The optimum actuator locations for 1"x2", 2"x2", 2"x3", and 1"x3" as determined from the genetic algorithm are shown in Figure 5.3 (a)-(d), respectively. The finite element mesh used for these iterations is 10x14, which yields an element resolution of 1"x1". The 10x14 mesh provides reasonable computational efficiency; however, it does not facilitate symmetric actuator placement.

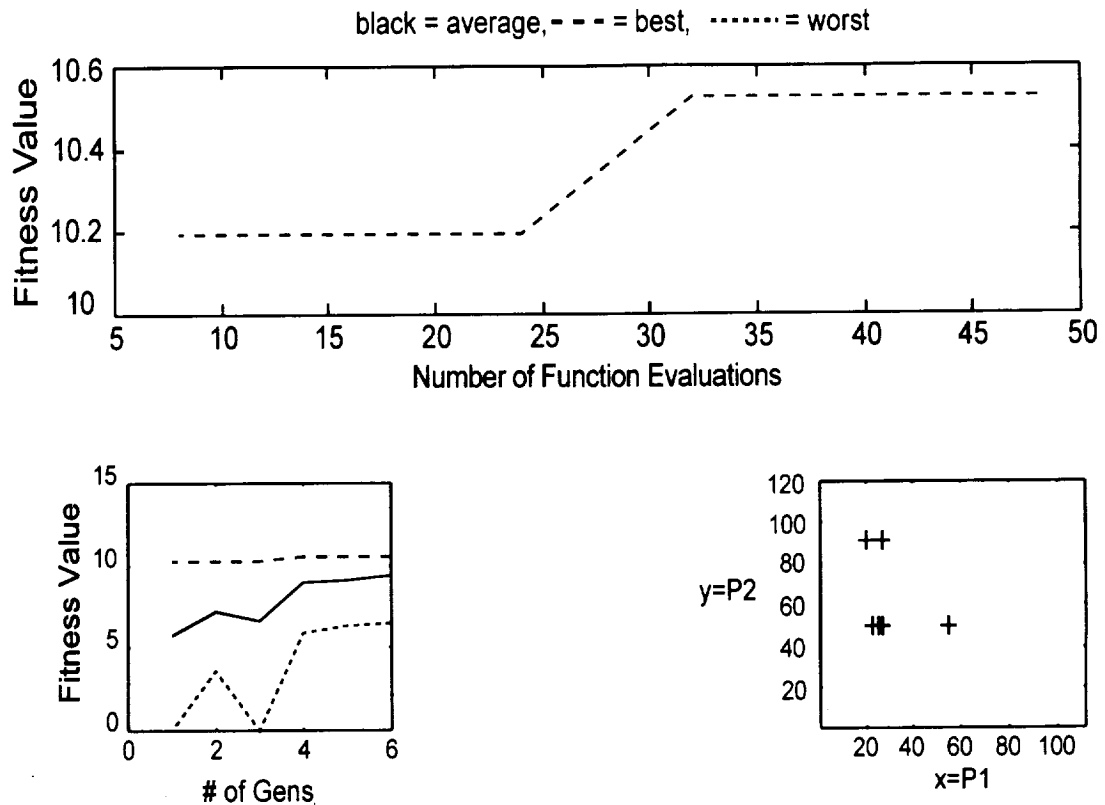


Figure 5.2 Genetic Algorithm Output

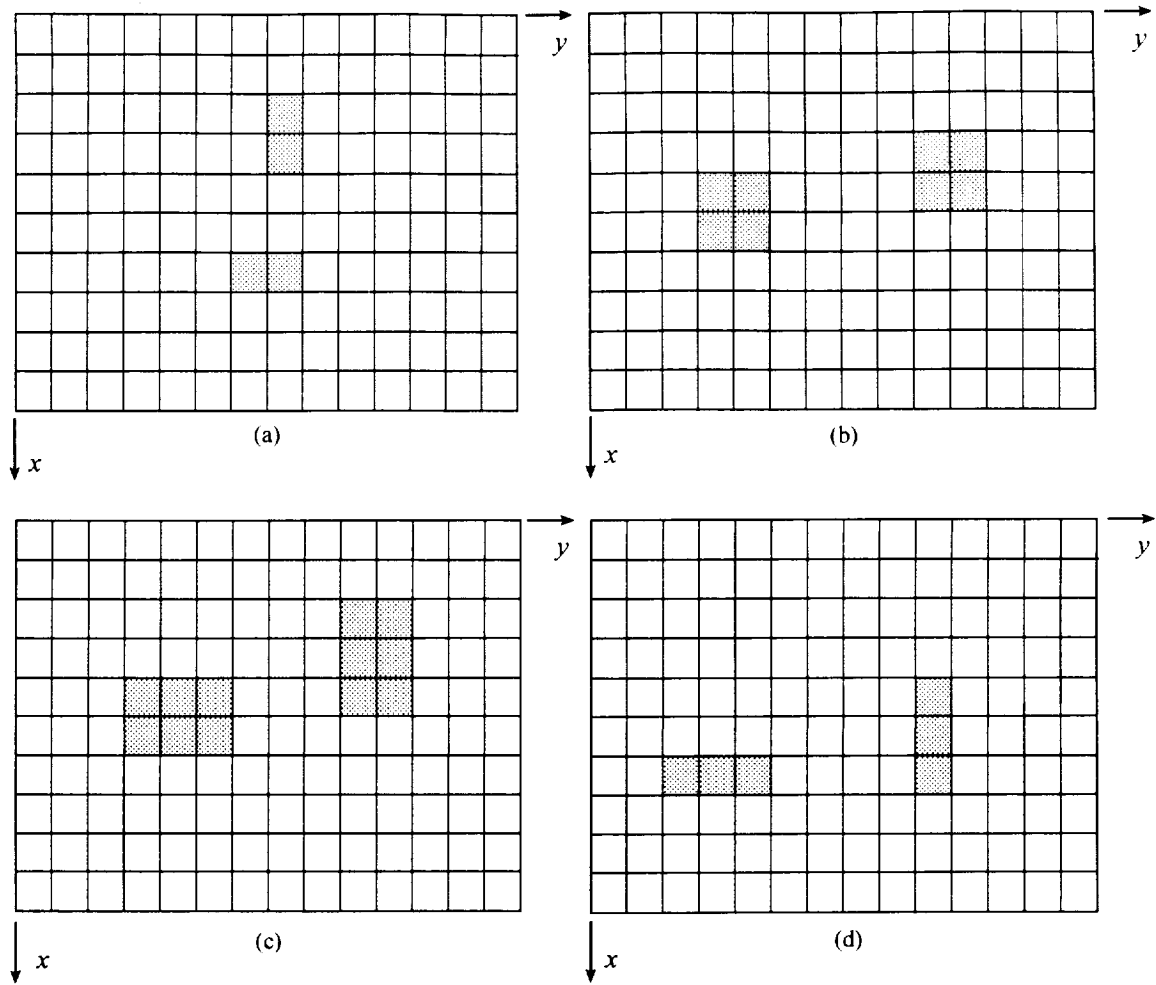


Figure 5.3 GA Actuator Placement

A non-uniform meshing scheme would overcome this obstacle; however, it requires an adaptive meshing routine. The adaptive meshing scheme is not included since it introduces another level of optimization. Even though adaptive mesh refinement techniques have been successfully applied to stress recovery problems, it would be computationally extensive for this application. In lieu of adaptive mesh refinement, the initial genetic algorithm results are further evaluated using a 20x28 finite element mesh yielding an element resolution of $\frac{1}{2}'' \times \frac{1}{2}''$. Hence, each 1''x3'' piezoceramic actuator is modeled with a 2x6 mesh. The optimum actuator locations depicted in Figure 5.3(d) were enhanced using the refined mesh, resulting in the locations shown in Figure 5.4.

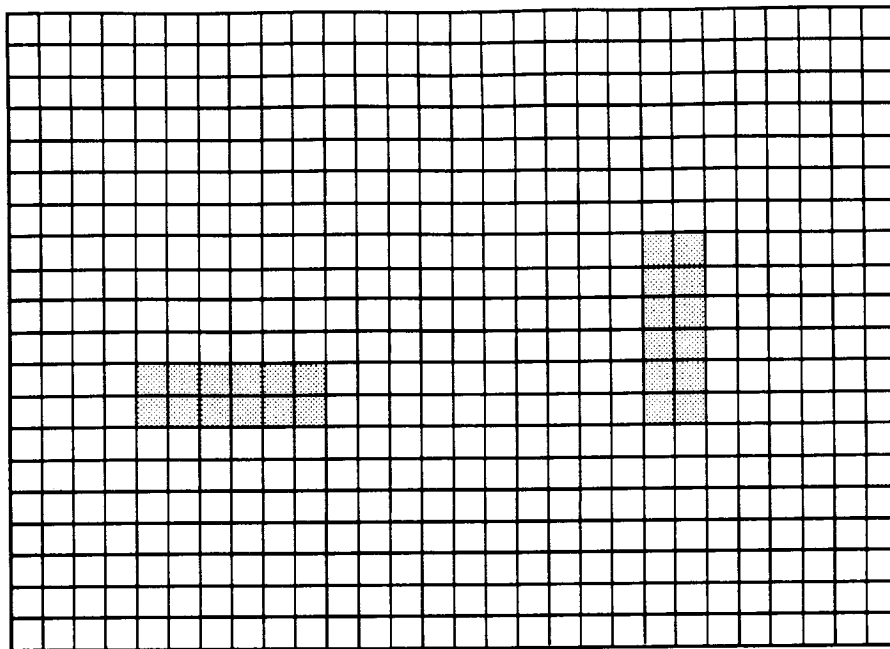


Figure 5.4 Refined Optimum Actuator Locations

The actuator locations shown in Figure 5.4 are used to design the panel used in experiments to validate the analytical design method. Two other panels are also manufactured with different actuator locations to establish comparable performance data. The non-optimum panels were also modeled using the finite element program to provide corresponding analysis for comparison. Details describing the non-optimum test panels are presented in Chapter VI.

CHAPTER VI

EXPERIMENTAL AND NUMERICAL RESULTS

Introduction

Several flat panels with various piezoceramic actuators locations are experimentally tested to ensure the accuracy of the analytical method presented. The experimental results suggested that the analytical model be improved to include a transmission path representing the disturbance to radiated sound power, which is consistent with the experimental data. A brief description of acoustic measurements is included, followed by details of the data acquisition system and control method implemented is provided before discussing the experimental results. The analytical data presented include results from both the initial analysis and the improved model. The accuracy of the improved model is established since the analytical data agrees well with the experimental data. Evaluating the sound transmission loss characteristics of a panel using active structural acoustic control determines the effectiveness of the piezoceramic actuator locations.

A sound transmission loss (STL) suite facilitated the experiments by providing the opportunity to evaluate various panels subjected to an acoustic disturbance. The STL suite provides a window between two adjacent rooms, one anechoic and the other reverberant. The window between the adjacent rooms facilitates the test panel and provides excessive sound transmission loss, thereby providing a convenient means of evaluating the sound transmission of the test specimen. The anechoic chamber provides a non-reverberant environment that supports acoustical measurements of the radiated sound through the test specimen. The source room, or reverberant chamber, contains a

loudspeaker sound source that provides structural acoustic disturbance. To characterize the STL suite, a baseline panel without piezoceramic actuators is inserted between the two rooms and the structurally radiated noise is measured due to a broadband random excitation. The structurally radiated sound pressure is measured in the receiving room while the loudspeaker provides an acoustic disturbance in the source room. The receiving room microphones and source room loudspeaker configuration is shown in Figure 6.1.

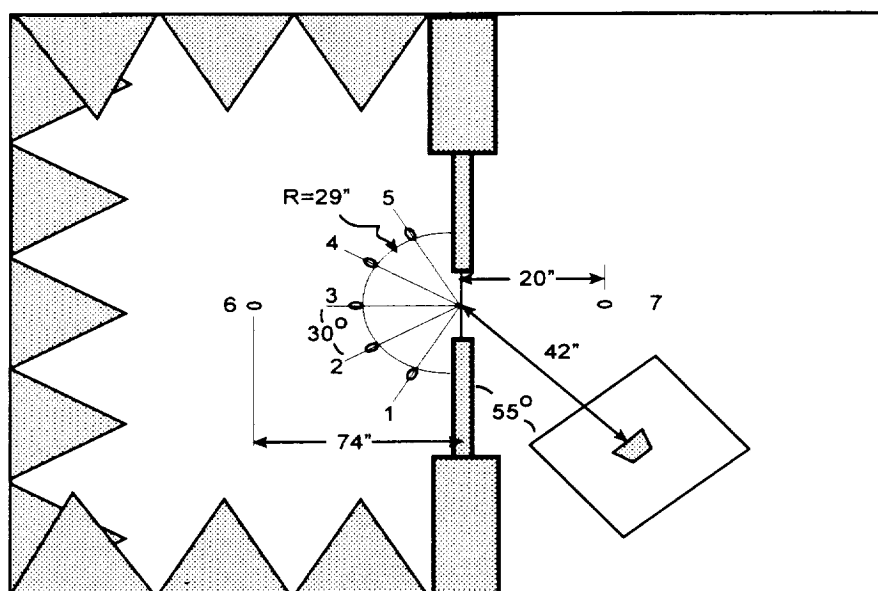


Figure 6.1 STL Instrumentation Layout

A traditional STL suite provides a highly reverberant source room devoid of standing waves. Such a source room provides a statistically uniform sound field impinging upon the test specimen characterized by the sound power of a known calibrated source. On the other hand, the receiving room provides a free-field environment suitable for measuring sound pressure levels using conventional microphones to support sound power calculations. By measuring the free field acoustic

pressure over a hemispherical surface, it is possible to measure the radiated sound power.

The estimated sound power may be determined by

$$10\log_{10}\left(\frac{P}{P_o}\right) = 20\log_{10}\left(\frac{p_m}{p_o}\right) + 10\log_{10}\left(\frac{S}{S_o}\right) \quad (6.1)$$

where P is the estimated sound power, $P_o = 10^{-12} W$, p_m is the mean measured sound pressure, $p_o = 20 \mu Pa$, S is the hemisphere surface area, and S_o is $1 m^2$. Figure 6.2 shows a typical sound power spectrum of the sound source measured 20 inches away from the center of a baseline test panel and the corresponding sound power in the receiving room.

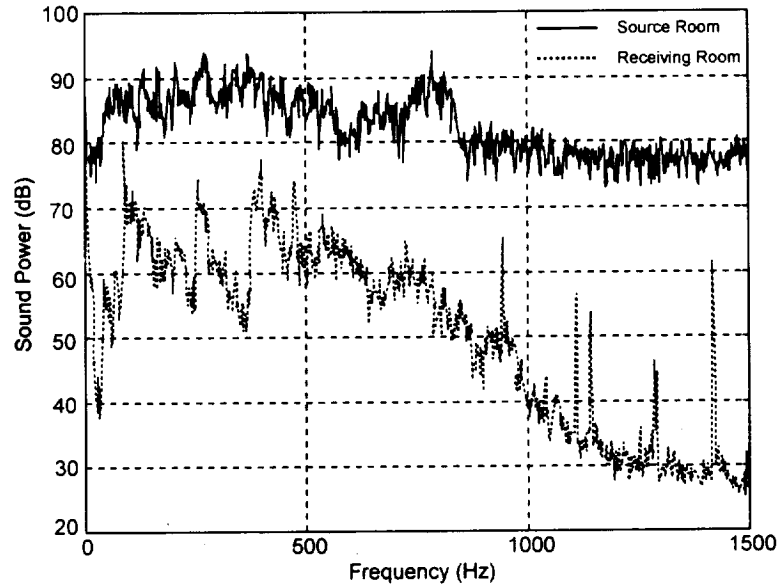


Figure 6.2 Source and Receiving Room Sound Power

The sound transmission loss of the specimen can be calculated simply by subtracting the source and measured sound power. The baseline test panel is identical to subsequent panels tested, but is not fitted with piezoceramic actuators.

Data Acquisition and Control

To validate the accuracy of the analytical model, several real time control experiments tests are conducted. Real time control of the radiated structure-borne noise was achieved by utilizing a control system implemented on a Texas Instruments TMS320C40[®] digital signal processor (DSP). An Intel Pentium[®] personal computer hosted the DSP and MATLAB[®] was used to design a state-space controller and subsequently download this controller to the DSP board. The DSP program codes and supporting MATLAB[®] files were developed by NASA Langley Research Center resulting in a real-time turnkey active structural acoustic control system.⁵⁸ Originally, NASA implemented a general predictive control algorithm⁵⁹ (GPC); however, LQR control was utilized for these experiments to be consistent with the analytical results.

Following the analytical format, radiation filters were included to calculate the structural radiated noise. Hence, the traditional sound power measurement technique described above was not employed. Instead, the structural radiated noise was calculated using the measured panel surface accelerations and corresponding radiation filters based on the radiation modal expansion technique. The radiation filter concept ensures a causal system since it relies on the structural surface velocity to calculate the far field radiated sound power. Since microphones must be located in the far field, an inherent propagation delay exists between the surface velocity and the measured sound pressure. Therefore, causality is not guaranteed.

The plant dynamic characteristics were determined by system identification using an observer/Kalman filter identification algorithm. The OKID⁶⁰ system identification algorithm performs modal parameter identification by applying a disturbance to the

piezoceramic actuators and measuring the response of panel vibrations using accelerometers. The accelerometers provide sensor information, used to calculate the radiated sound power, during the closed loop experiments. Two actuators and fifteen accelerometers were used in each of the panels tested. The locations of the actuators varied for each test; however, the locations of the accelerometers remained fixed. The fifteen-accelerator locations are shown in Figure 6.3. Each accelerometer represents a discrete acoustic radiator as previously described in the Radiation Filter section.

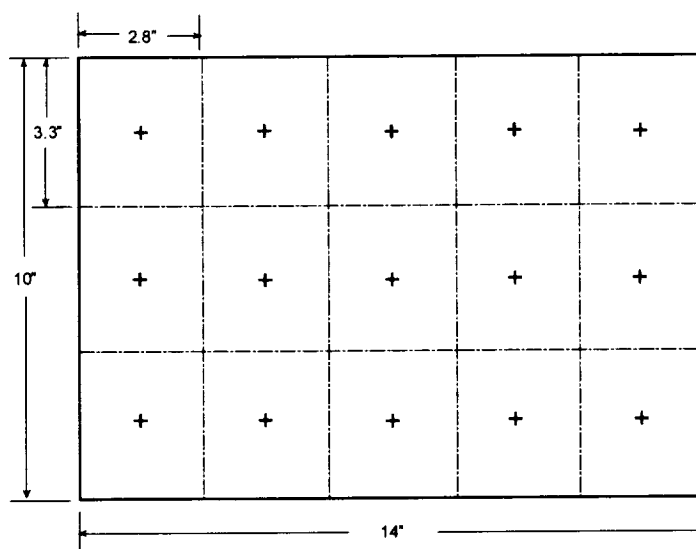


Figure 6.3 Accelerometer Locations

A state-space LQR controller was designed using the experimental modal parameters determined from the system identification data using MATLAB.[®] The controller includes the acoustic radiation filters of the first three dominant acoustic radiation modes and subsequently downloaded to the DSP board to support real-time control. The control effort penalty, determined through trial and error, remained constant for each panel tested. Prescribed experimental parameters include a sampling frequency of 1.5 kHz, bandwidth of 500 Hz, three acoustic radiation modes, and 35,000 data

samples. For each experiment, the panel is exposed to broadband random noise with a flat response to 800 Hz.

Experimental Results

Experiments were conducted for three different panels to validate the analytical prediction of the optimum actuator placement to achieve the greatest reduction in radiated structure-borne noise. Each panel has two piezoceramic actuators bonded to the same side of the panel. This configuration obviously prohibits overlapping piezoceramic actuators; however, it represents realistic aerospace application by restricting the actuators to lie within the fuselage interior. The panels are 6061-T6 aluminum and are clamped along all edges. The overall panel dimensions are 22"x20"x0.040"; however, the clamping fixture provides a 14"x10" window exposing the test panel area. The clamping fixture was constructed of two 6061-T6 aluminum plates ½" thick with 52 bolts around the inner perimeter and 8 bolts around the outer perimeter. The outer bolts were used to attach the fixture to the STL window. The piezoceramic actuators are PZT-5A⁶¹ with dimensions 1"x3"x0.01". The three panels tested, designated A, B, and C, are shown in Figures 6.4-6.6, respectively.

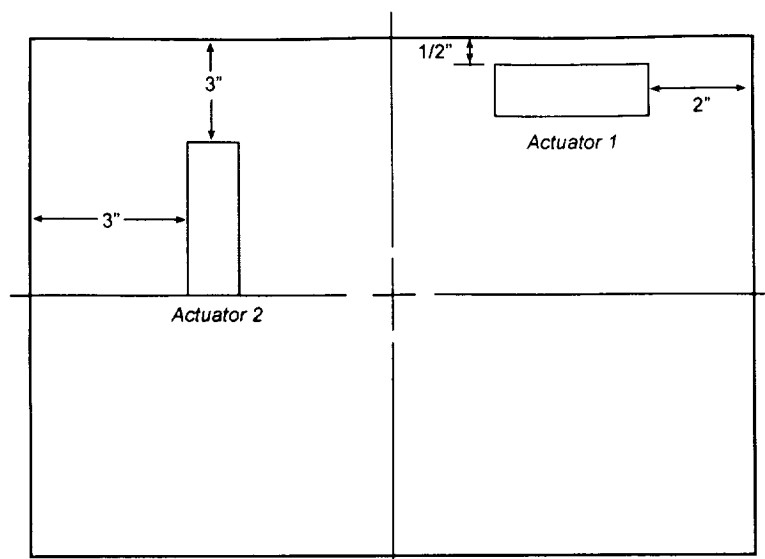


Figure 6.4 Panel A Actuator Placement

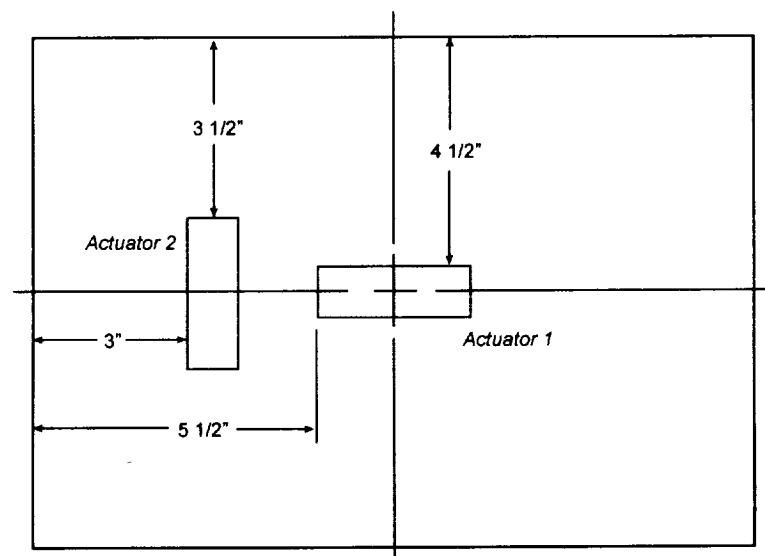


Figure 6.5 Panel B Actuator Placement

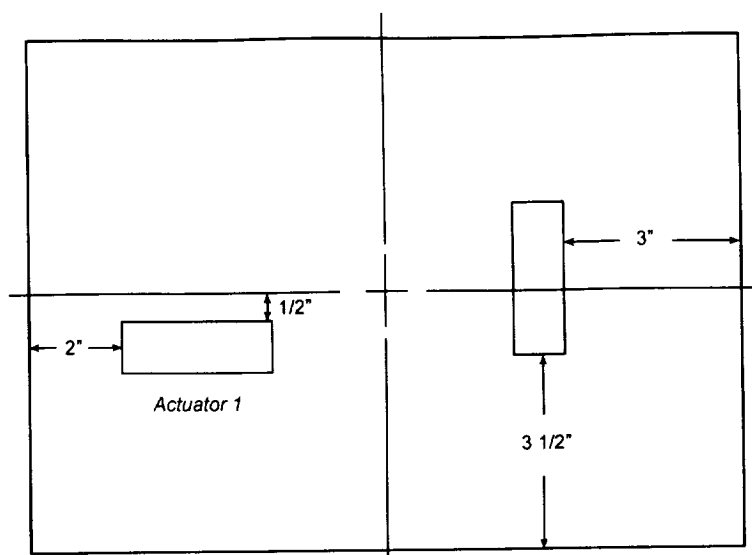


Figure 6.6 Panel C Actuator Placement

To evaluate the performance of the piezoceramic actuator locations selected, the open and closed loop structure-borne acoustic radiation was determined experimentally for each panel subjected to a random acoustical disturbance using the loudspeaker shown in Figure 6.1. The location of the piezoceramic actuator on the panel determines the effective structural modal interaction of each actuator. Thus, optimum actuator locations have strong modal coupling with the dominant acoustic radiation modes. For a rectangular panel, the structural modes $(1,1)$, $(3,1)$, $(3,2)$, $(1,3)$, and $(2,3)$, where the (i,j) indices indicate the mode shape along the major and minor panel dimensions respectively, are dominant acoustic radiators. As outlined in the section on radiation filters, structural vibration mode shapes that do not contribute to the acoustic radiation modes are not targeted for effective control. The experiments indicate that panel C provides the best radiated noise reduction, panel B is next best, and finally panel A.

The radiated noise reduction is determined from the difference between the open and closed loop radiated sound power. The open loop radiated sound power is

determined while the panel is subjected to an acoustic disturbance without invoking the control algorithm. Similarly, the closed loop structurally radiated sound power is calculated by invoking the control algorithm. Accelerometers provide a convenient means of measuring structural vibrations. However, the radiation filters must be modified to calculate radiated sound power due to acceleration in lieu of velocity. The noise reduction, or attenuation, is then determined by the quotient of the sum of the squared magnitude of the open and closed loop sound power from 40 to 500 Hertz.

Table 6.1 summarizes the closed loop sound power attenuation of each mode of concern for several closed loop control experiments. The structurally radiated sound power attenuation shown in Table 6.1 is the difference between the open loop panel and a closed loop panel with two actuators. The values in Table 6.1 are obtained from Figures 6.7-6.9 by converting the decibel levels to the squared magnitudes and taking the difference between the open and closed loop data and converting to decibels. Data is presented for several experiments, and the mean is considered for analysis. The number 1 actuator location of panel A had such low control authority that it was unstable for most experimental runs. The control authority could have been weighted as to limit power to actuator 2; however, the results would have been inconsistent with the other panels. Furthermore, the analysis predicted that panel A would provide the worst-case performance. The data indicates that control authority is limited for higher order modes, namely $(1,3)$ and $(2,3)$ modes. In fact, the $(2,3)$ mode did not show up in the data for any panel and therefore was not included in Table 6.1. Since the $(2,3)$ mode was not present in the open loop data, these results lead to the conclusion that the acoustic disturbance did not sufficiently excite this structural mode. Amplifying the actuation voltage or

increasing the actuator size may have enhanced control of the higher modes. Panel C obtains the best ranking, due mainly to its ability to control mode (3,1) the best. Panel C has a mean attenuation of -9.98 dB for mode (1,1), as compared to -9.04 dB for panel B and -8.64 dB for panel A. However, for mode (3,1) the attenuation for panel C is 2.9 dB greater than panel B.

Table 6.1 Open and Closed Loop Sound Power Attenuation

	Structurally Radiated Noise Attenuation (dB)			
Mode	(1,1)	(3,1)	(3,2)	(1,3)
Panel A	-8	-6.67	-6	-0.67
	-9.33	-4	-2.67	-2
Mean	-8.64	-5.23	-4.18	-1.31
Panel B	-11.67	-8	-7.33	-4.67
	-8.3	-7.59	-6.2	0
	-7.67	-9.33	-8.76	-6.67
Mean	-9.04	-8.28	-7.37	-3.31
Panel C	-10.67	-9.33	-6.33	-5.33
	-10	-13.33	-10	-3.33
	-9.33	-11.33	-9	-3.33
Mean	-9.98	-11.18	-8.30	-3.95

The experimentally determined structurally radiated sound power for the open and closed loop performance of panels A, B, and C are shown in Figures 6.7-6.9 respectively. The radiated sound power is calculated using the radiation filters and the measured panel accelerations. The open loop data is determined while the panel is subjected to a broadband random acoustic disturbance without invoking the control algorithm. The closed loop radiated sound power is calculated with the same disturbance; however, the control loop between the radiated sound power and the two actuators is invoked.

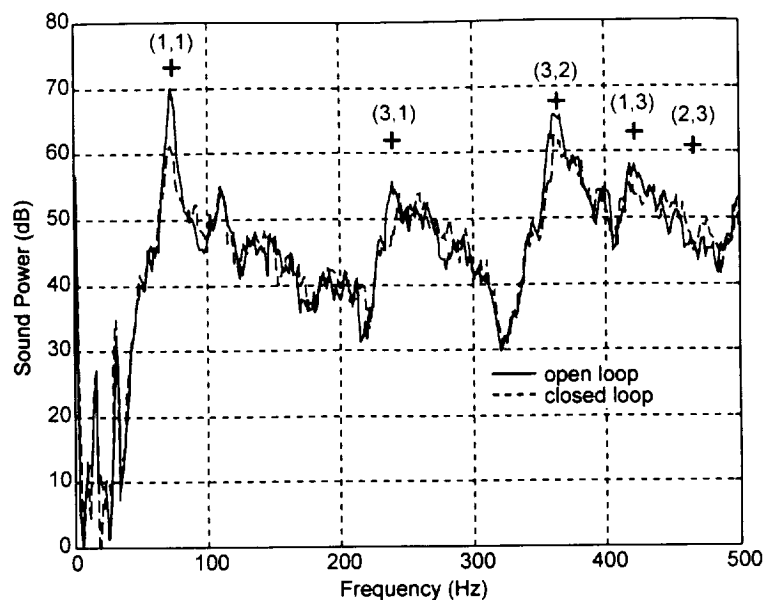


Figure 6.7 Open and Closed Loop Performance of Panel A

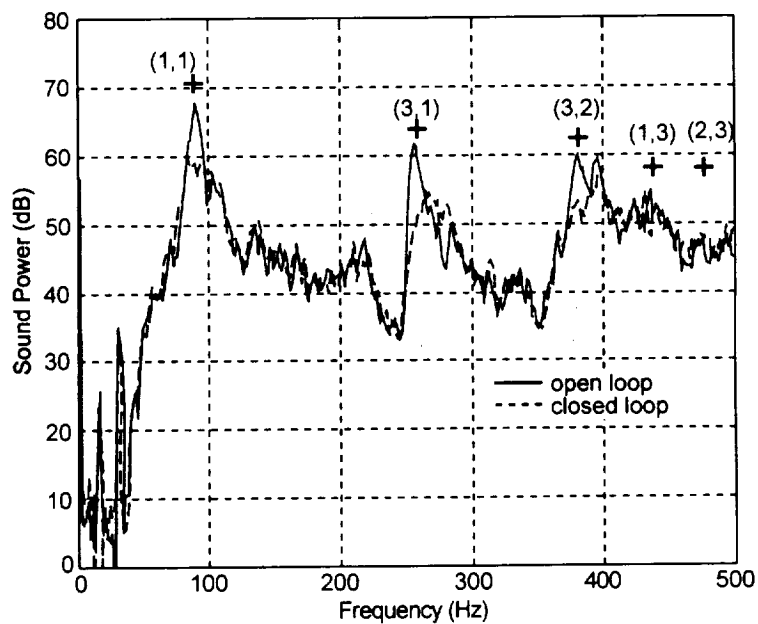


Figure 6.8 Open and Closed Loop Performance of Panel B

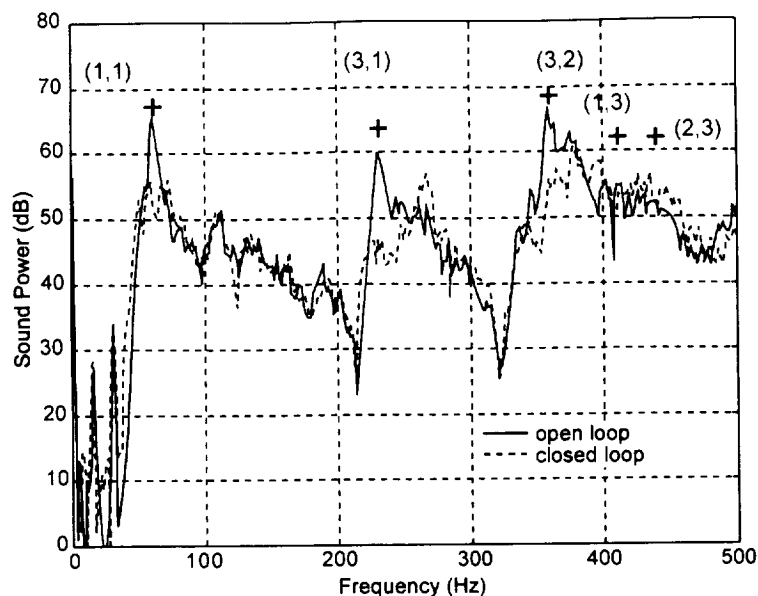


Figure 6.9 Open and Closed Loop Performance of Panel C

Analytical Results

The refined finite element analysis used to model the experiments utilized a modified rectangular high precision plate element with 24 nodal DOF with an additional electrical DOF for each actuator.¹⁰ The finite element mesh consisted of 20x28 elements for the panel. Each piezoceramic actuator consisted of a 2x6 mesh. Even though the panel was 0.040" thick, the small displacement approximation was used since the experimental disturbance sound pressure never exceeded 95 dB.

Panel C represents the predicted optimum actuator locations determined from the GA simulation. Analytical models were also constructed to represent panels A and B to further compare analytical results to the experimental data. Analytical performance is evaluated by comparing the radiated power attenuation determined from the open and closed loop singular value decomposition of the system frequency response. The closed loop transmission path is from the actuator control signals to the sound power output. For a multiple-input, multiple-output system, the singular value decomposition is

analogous to Bode plots commonly used for single-input, single-output systems.⁶²

Analytical results for the predicted sound power reduction are summarized in Table 6.2.

Table 6.2 Open and Closed Loop Predicted Sound Power Attenuation

Attenuation (dB)					
Mode	(1,1)	(3,1)	(3,2)	(1,3)	(2,3)
Panel A	-7.3733	-21.5816	-1.9749	-0.1426	-2.2925
Panel B	-11.3157	-15.6861	-0.0985	-8.5569	-14.0291
Panel C	-10.2561	-19.3582	-0.4863	-7.6422	-15.7369

The data indicates that the analytical results exhibit control authority for the entire bandwidth. This behavior is expected since LQR control does not model extraneous signal noise present in the experiments. The analysis indicates that the performance of panel C is slightly better than panel B. This observation is consistent with the experimental results. The singular values of the open and closed loop sound power from actuator control input for each panel are shown in Figures 6.10-6.12. The analytical data is normalized to indicate relative attenuation between each panel for a constant control effort penalty. The open loop dynamic characteristics shown in Figures 6.10-6.12 is significantly different for each panel since the data describes the transmission path from distinctly different actuator locations of each panel to the radiated sound power. Thus, the data represents the transmission path from the actuators to radiated sound power.

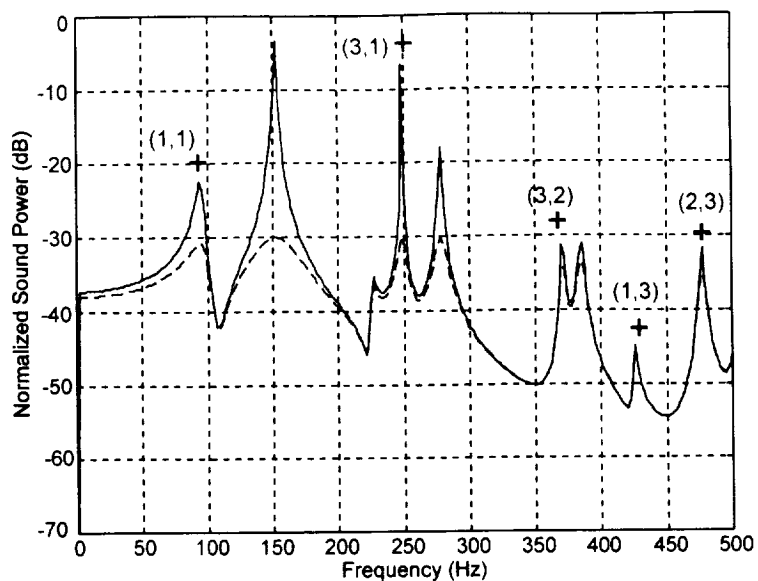


Figure 6.10 Panel A Singular Values

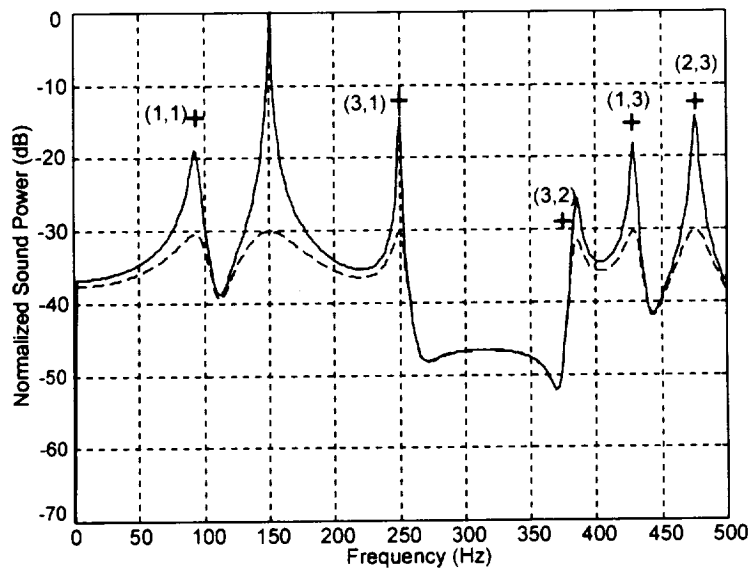


Figure 6.11 Panel B Singular Values

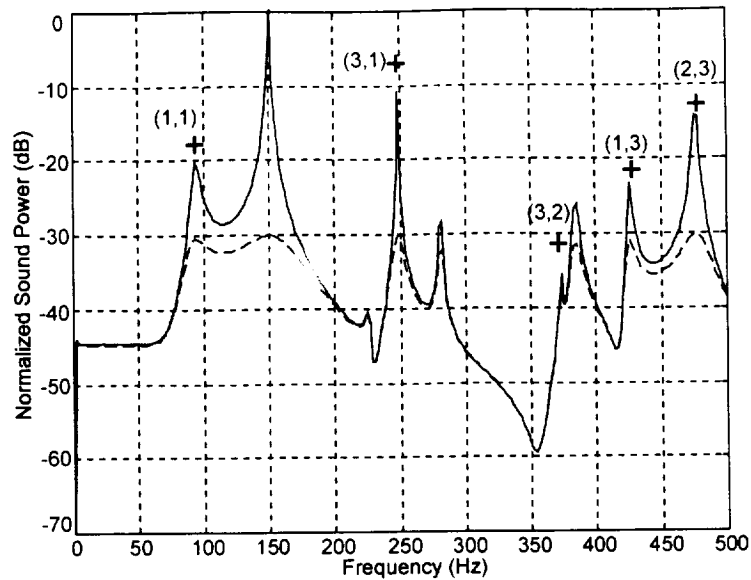


Figure 6.12 Panel C Singular Values

The analytical predicted results are consistent with the experimental test results. However, the predicted level of attenuation was not clearly confirmed by the experimental test data. Therefore, the analytical model is modified to include the transmission path represented by the experimental tests. Thus, the model is modified to predict the structurally radiated sound power due to a uniform random acoustical disturbance.

The closed loop path now becomes the structurally radiated power due to the acoustical disturbance. The open loop structurally radiated power is determined for the same acoustic disturbance without applying a control signal to the actuators. The quotient of the sum of the squared magnitude of the open and closed loop curve from 40 to 500 Hz. in decibels determines the structurally radiated power attenuation. This attenuation level was then used as the performance index for the genetic algorithm. Therefore, the GA determined the best actuator location by maximizing the attenuation of the structurally radiated power. The acoustic disturbance was modeled as a uniform

random plane wave and interpolated to the transverse finite element nodes. The uniform random acoustic disturbance had an overall power of 92 dB and the power spectrum density is shown in Figure 6.13.

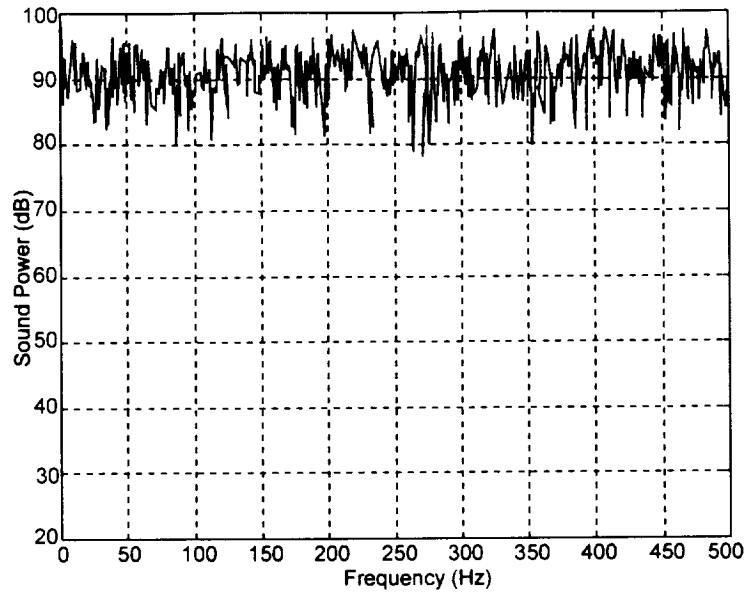


Figure 6.13 Uniform Random Simulation Acoustic Disturbance PSD

To validate the simulation model, the open and closed loop structurally radiated power was computed for panel configurations B and C and compared to the test results. The attenuation for panel B is -2.415 dB and the predicted structurally radiated sound power is shown in Figure 6.14. The attenuation for panel C is -3.107 dB and the predicted structurally radiated power is shown in Figure 6.15.

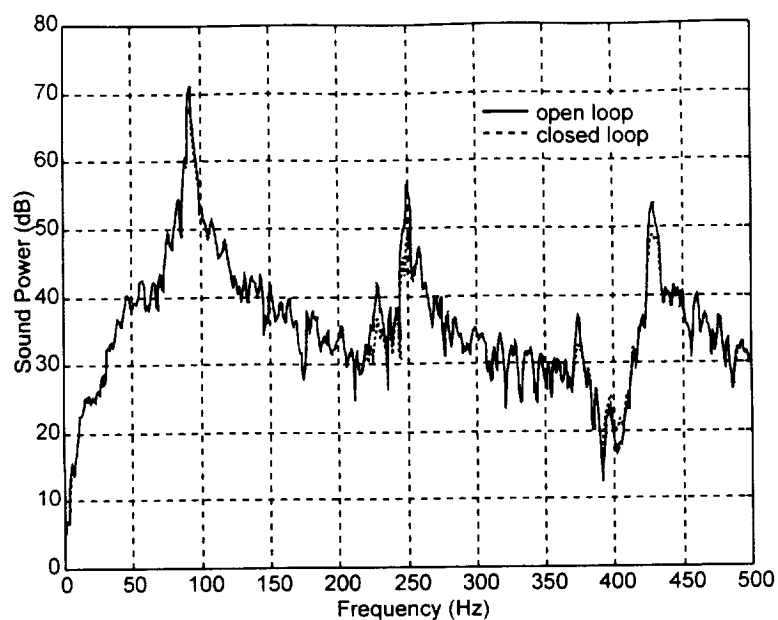


Figure 6.14 Predicted Open and Closed Loop Radiated Power for Panel B

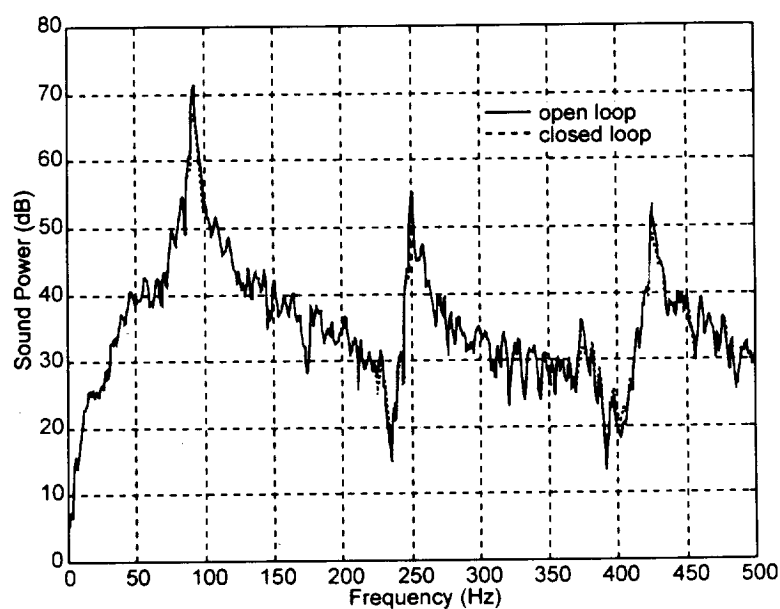


Figure 6.15 Predicted Open and Closed Loop Radiated Power for Panel C

The predicted radiated sound power for panels B and C are shown in Figures 6.14 and 6.15, respectively. The predicted open loop radiated sound power data shown in Figures 6.14 and 6.15 agrees well with the corresponding test data shown in Figures 6.8

and 6.9. However, the predicted closed loop radiated sound power due to the disturbance is less than the corresponding closed loop test data shown in Figures 6.14 and 6.15 and the previous analytical data shown in Figures 6.11 and 6.12. Recall that the closed loop analytical results shown in Figures 6.11 and 6.12 do not include a disturbance and that the transmission path is from the actuators to the radiated sound power. Since control due to a disturbance is a more difficult problem, the lower performance gains are not unexpected. However, by increasing the control authority the performance of panels B and C, indicated in Figures 6.14 and 6.15, may be improved. However, the control authority specified was carefully selected since the GA searches for a global maximum, and many non-optimal actuator locations become unstable for larger values of control authority.

The GA search is modified to define the performance index as the predicted radiated sound power attenuation. Using this new performance index the GA search predicted an optimum actuator location previously not considered. This new optimum location is shown in Figure 6.16.

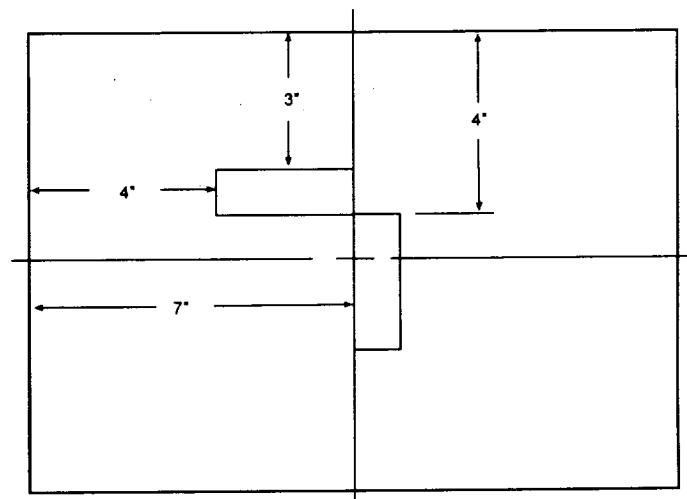


Figure 6.16 Revised Optimum Actuator Locations

The calculated attenuation for the revised optimum location is -4.783 dB. The predicted radiated power for the revised optimum panel is shown in Figure 6.17. The control effort penalty is constant for the data shown in Figures 6.14, 6.15 and 6.17.

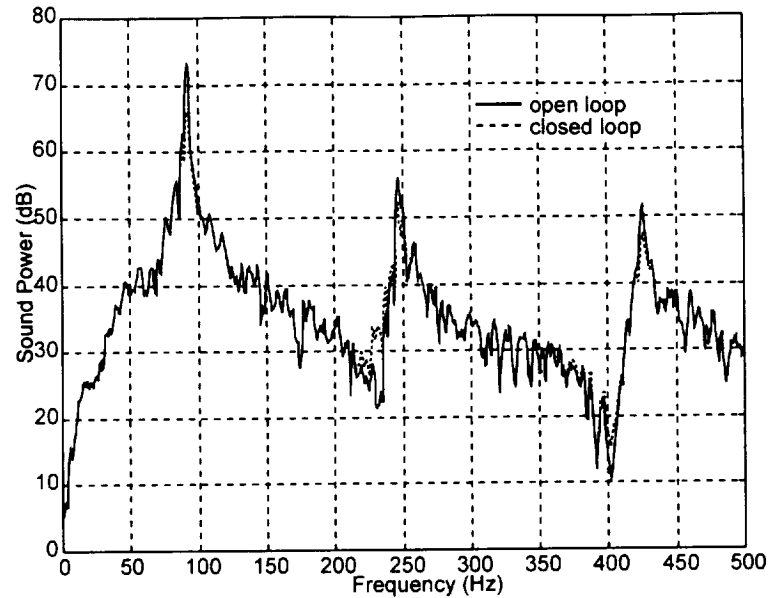


Figure 6.17 Predicted Radiated Power for the Revised Optimum Panel

An alternative metric for determining the optimum actuator location was investigated using the piezoelectric modal participation. The piezoelectric modal participation is determined by substituting the modal coordinate transformation into Eq. (3.113) resulting in

$$\{\Lambda\} = [K_\phi]^{-1} [K_{\phi W}] [\Phi] \quad (6.2)$$

where $[\Phi]$ is a matrix of the normal structural mode shapes. The coupled stiffness matrix $[K_{\phi W}]$ has dimensions $np \times ndof$, where np is the number of actuators and is formed by assembling the coupling stiffness for each element where piezoceramic is present. Therefore, the piezoelectric modal participation represents the effective coupling

between the actuator and the structural modes. Table 6.3 presents the piezoelectric modal participation for each panel tested.

Table 6.3 Piezoelectric Modal Participation

Piezoelectric Modal Participation					
Mode	(1,1)	(3,1)	(3,2)	(1,3)	(2,3)
Panel A	0.6749	1.0013	0.6760	0.0864	0.1369
Panel B	1.0569	1.4056	0	1.5147	0.7311
Panel C	0.7810	1.3226	0.1769	1.0287	0.8538

The piezoelectric modal participation follows the acoustic attenuation shown in Table 6.3, except for mode (3,1) of panel B and C. The modal participation shows that panel B should have greater control of mode (3,1) when compared to panel C. Although, the modal participation distinctly shows that panels B and C are better than panel A.

Overall, the analytical method presented agrees well with the experimental test data for determining piezoceramic actuator locations for structural acoustic noise reduction. However, it was anticipated that the difference between panels B and C would be much more pronounced. The analysis indicates that for the given panel and actuator size, the optimum performance margin is narrow. Furthermore, when the analytical results are carried out in real experiments, such narrow performance margins may not be detectable.

CHAPTER VII

CONCLUSION

By combining coupled finite element analysis, radiation acoustic filters, feedback control theory, and optimal actuator placement using a genetic algorithm, a method for predicting acoustic radiation control was developed and compared to experimental tests. Analytical results were provided for both flat and curved panels with bonded piezoceramic actuators. However, the formulation provides the ability to accommodate laminated composites with embedded piezoceramic actuators and sensors. Furthermore, the triangular shell formulation supports advanced anisotropic piezoceramic transducer concepts. The analytical results show that the coupled finite element formulation is imperative since the material properties of the piezoceramic alter the structural dynamic response. This effect was most significant when anisotropic piezoceramics were considered. The data presented clearly demonstrates that the anisotropic piezoceramic provides enhanced performance over traditional piezoceramics for structural vibration control of curved panels. The data presented for structural acoustic control of curved panels with a single MFC actuator does not demonstrate improved performance when compared to a traditional PZT actuator. This result is not unexpected since actuators orientation angles of $\pm 90^\circ$ are not considered.

However, structural acoustic radiated power simulations for flat rectangular panels indicate that MFC actuators do not improve the sound power attenuation when compared to traditional PZT. The simulations indicate that MFC actuators may be best suited for complex geometric structures requiring induced strain along a preferred

direction. Anisotropic piezoceramic actuators provide control authority along a principal direction, which introduces transducer orientation as an additional design parameter.

The coupled finite element model formulation developed with MFC is derived from linear piezoelectric theory. However, further research is needed to validate the linear piezoelectric assumption since the electric field distribution may in fact be non-uniform along the length of the piezoceramic fiber. The potential non-uniformity arises due to the geometry of the interdigital electrodes. Further research may reveal enhanced transducer performance if the interdigital electrode geometry is optimized. To further enhance the analytical models, it is strongly suggested that extensive mechanical testing be conducted on MFC specimens to accurately determine their mechanical properties.

Structural vibration control of a single bonded MFC actuator was determined to provide a significant increase in performance when compared to an equivalent traditional piezoceramic actuator. Based on the results of this research, structural control can be greatly enhanced by including multiple actuators, each with various orientation angles. Such a configuration would result in various twisting actuators. Furthermore, laminated composites panels with embedded MFC transducers should be considered in future research efforts. Since multiple MFC actuators with various orientation angles embedded within anti-symmetric laminated composites will provide interesting structural control opportunities.

By incorporating the acoustic radiation filter concept, the structural acoustic field is determined directly from the structural vibration characteristics. The radiation operator utilized by the filters reduces the three-dimensional volume integration to a surface integral and when applied to a discretized surface results in individual acoustic radiators.

The acoustic radiation filter was implemented for both analytical and experimental results for the flat panel configuration. The radiation filter concept ensures a causal system since the sound power calculation uses the structural surface velocity. By incorporating the radiation filters directly in the state-space experimental, or analytical, plant model a consistent sound power calculation is developed for comparison.

The experimental test validates the accuracy of the analytical model. Therefore, the analytical model provides a design tool to determine optimal actuator placement in advance of structure construction. Determining the optimal actuator placement using only an experimental approach requires an inordinate amount of time and materials since the actuators must be permanently bonded to the structure. Analytical results were determined using acoustic radiation filters for curved panels using finite element analysis. The radiation modal expansion technique provided an efficient computational method for approximating the dominant acoustic radiation modes for both analysis and real time control experiments.

Feedback control is achieved using a linear quadratic regulator (LQR) for both analytical predictions and experimental tests. LQR control provides an optimal performance limit achievable for ideal state feedback control without any uncertainties²⁵ and is well documented in the literature. Preliminary experimental tests were conducted using the general predictive control (GPC); however, the performance involved optimal parameter selection. Determining the optimum actuator locations might have been obfuscated by poor GPC parameter selection.

The actuator placement optimization search technique selected was a modified genetic algorithm. The genetic algorithm with stochastic coding used binary parameters

mapped to the actuator locations via the finite element mesh. The finite element model was embedded within the genetic algorithm and the structural acoustic attenuation was defined as the performance index. The GA performance index is the structurally radiated noise of the panel due to a broadband random acoustic disturbance. Acoustic radiation filters, using the dynamic solution of the coupled finite element model, compute the structurally radiated noise. Therefore, the analytical simulation is analogous to the real-time experimental test conducted. A commercial genetic algorithm code was selected to facilitate the research objective of finding the optimum actuator locations.

The experimental test results agreed with the analytical results. However, the analytical model, based on a transmission path between the actuators and radiated sound power, indicates that the attenuation should be greater than indicated by the experiments. Therefore, the analytical model was modified to include a transmission path representing the disturbance to radiated sound power. The analytical model now provides dynamic simulations that represent the experiments conducted. The simulations were verified by comparing the results to the experimental test data. Furthermore, an additional genetic algorithm search was performed using the disturbance to radiated sound power attenuation as the performance index. The GA determined a new optimum actuator location previously not considered. The experimental results may be improved by increasing the actuation voltage signal; however, the signal remained constant for all actuator configurations tested. Increasing the applied control authority will also enhance the analytical predicted attenuation. However, careful attention was placed on the control effort penalty to accommodate a global GA search method. An adaptive meshing scheme

would enhance the analytical method by increasing computational efficiency and accommodating larger piezoceramic actuators.

The predicted radiated noise of curved panels presented in Appendix A indicates that the inherent anisotropic material properties of the MFC actuator significantly affect the overall structural dynamics. Future research should include experimental test to accurately determine material properties of MFC actuators. Furthermore, future research should include experiments to validate the finite element method with MFC actuators.

REFERENCES

1. Hagood, N. W., Bent, A. A., "Development of Piezoelectric Fiber Composites for Structural Actuation," AIAA Paper No. 93-1717, *Proceedings of the 34th AIAA/ASME/ASCE/AHS/ASC Structures, Structural Dynamics, and Materials Conference* (La Jolla, CA), AIAA, Washington, DC, 1993, pp. 3265-3638.
2. Wilkie, W. K., Belvin, W. K., Park, K. C., "Aeroelastic Analysis of Helicopter Rotor Blades Incorporating Anisotropic Piezoelectric Twist Action," *Proceedings of the ASME Aerospace Division*, AD-Vol. 52 1996, pp. 423-433.
3. Miller, S. E., Abramovich, H., Oshman, Y., "Active Distributed Vibration Control of Anisotropic Piezoelectric Laminated Plates," *J. Sound and Vibration* 183 (5) 1995, pp. 797-817.
4. Lee, C. K., "Theory of Laminated Piezoelectric Plates For the Design of Distributed Sensors/Actuators, Part I: Governing Equations and Reciprocal Relationships," *J. Acoust. Soc. Am.* 87 (3) March 1990, pp. 1144-1158.
5. Allik, H., Hughes, T., Jr., "Finite Element Method for Piezoelectric Vibration," *International J. for Numerical Methods in Engineering*, Vol. 2 1970, pp. 151-157.
6. Tzou, H. S., *Piezoelectric Shells*, Kluwer Academic Press, Netherlands, 1993.
7. Tseng, C. I., "Development of a Thin Piezoelectric Finite Element Applied to Distributed Sensing and Vibration Controls," *ASME Winter Annual Meeting*, Chicago, IL, 88-WA/CIE-2, 1988.
8. Hwang, W. S., Park, H. C., "Finite Element Modeling of Piezoelectric Sensors and Actuators," *AIAA J.* Vol. 31 No. 5 1993, pp. 930-937.
9. Zhou, R. C., "Finite Element Analysis for Nonlinear Flutter Suppression of Composite Panels at Elevated Temperatures Using Piezoelectric Materials," Ph.D. Dissertation, Department of Aerospace Engineering, Old Dominion University, Norfolk VA, 1994.
10. Bevan, J. S., "Analysis and Testing of Plates with Piezoelectric Sensors and Actuators," M.S. Thesis, Department of Aerospace Engineering, Old Dominion University, Norfolk VA, 1997.
11. Tzou, H. S., Ye, R., "Analysis of Piezoelastic Structures with Laminated Piezoelectric Triangular Shell Elements," *AIAA, J.* Vol. 34, No. 1, January 1996, pp. 110-115.

12. Tzou, H. S., Bao, Y., Venkayya, V. B., "Parametric Study of Segmented Transducers Laminated on Cylindrical Shells, Part I: Sensor Patches," *J. Sound and Vibration*, 197 (2) 1996, pp. 207-224.
13. Saravanos, D. A., "Mixed Laminated Theory and Finite Element for Smart Piezoelectric Composite Shell Structures," *AIAA, J.* Vol. 35 No. 8, August 1997, pp. 1327-1333.
14. Borgiotti, G. V., "The Power Radiated by a Vibrating Body in an Acoustic Fluid and its Determination from Boundary Measurements," *J. Acoust. Soc. Am.* 88 (4) 1990, pp. 1884-2797.
15. Borgiotti, G. V., Jones, K. E., "Frequency Independence Property of Radiation Spatial Filters," *J. Acoust. Am.* 96 (6) 1994, pp. 3516-3524.
16. Borgiotti, G. V., Jones, K. E., "the Determination of the Acoustic Far Field of a Radiating Body in an Acoustic Fluid From Boundary Measurements", *J. Acoust. Soc. Am.*, 93 (5), May 1993, pp. 2788-2797.
17. Photiadis, D. M., "The Relationship of Singular Value Decomposition to Wave-Vector Filtering in Sound Radiation Problems," *J. Acoust. Am.* 88 (2) 1990, pp. 1152-1159.
18. Sarkissian, A., "Acoustic Radiation From Finite Structures," *J. Acoust. Am.* 90 (1) 1991, pp. 574-578.
19. Cunefare, K. A., "The Minimum Multimodal Radiation Efficiency of Baffled Finite Beams," *J. Acoust. Am.* 90 1991 pp. 2521-2529.
20. Cunefare, K. A., "Active Noise Control and the Modes of Planar Structures," AIAA 92-0372, *AIAA 30th Aerospace Sciences Meeting and Exhibit*, Reno NV, 1992.
21. Cunefare, K. A., "Effect of Modal Interaction on Sound Radiation From Vibrating Structures," *AIAA J.* 30 1992, pp. 2819-2828.
22. Cunefare, K. A., Currey, M. N., "On the Exterior Acoustic Radiation Modes of Structures," *J. Acoust. Am.* 96 1994, pp. 2302-2312.
23. Baumann, W. T., Saunders, W. R., Robertshaw, H. H., "Active Suppression of Acoustic Radiation from Impulsively Excited Structures," *J. Acoust. Am.* 90 (6) 1991, pp. 3202-3208.
24. Gibbs, G. P., Clark, R. L., Cox, D. E., Vipperman, J. S., "Radiation Model Expansion for Acoustic Control", *J. Acoust., Am.*, January 2000, pp. 332-339.

25. Clark, R. L., Cox, D. E., "Multi-Variable Structural Acoustic Control with Static Compensation," *J. Acoust. Am.* 102 (5) Pt. 1 1997, pp. 2747-2756.
26. Goldberg, D. E., *Genetic Algorithms in Search, Optimization, and Machine Learning*, Addison-Welsey, Reading, MA, 1989.
27. Ryou, J. K., Park, K. Y., Kim, Y. H., Kim, S. J., "Electrode Pattern Design of Piezoelectric Sensors and Actuators by Genetic Algorithm," AIAA 97-1348, *Proceedings of the AIAA/ASME/ASCE/AHS/ASC Structures, Structural Dynamics, and Materials Conference* (Kissimee FL), AIAA, Washington, DC, 1997, pp. 1747-1754.
28. Simpson, M. T., Hansen, C. H., "Use of Genetic Algorithms for Optimizing Vibration Actuator Placement for Minimizing Sound Transmission into Enclosed Spaces," *SPIE* Vol. 2717, 0-8194-2092-1, 1996, pp. 409-421.
29. Yao, L., Sethares, W. A., Kammer, D. C., "Sensor Placement for On-Orbit Modal Identification via a Genetic Algorithm," *AIAA J.*, Vol. 31, No. 10, 1993, pp. 1922-1928.
30. Tsao, C. C., "Use of the Genetic Algorithm in Positioning Sacrificial Anodes for Optimum Cathodic Protection," M.S., Department of Mechanical Engineering, Old Dominion University, Norfolk, VA, 1994.
31. Ikeda, T., *Fundamentals of Piezoelectricity*, Oxford University Press, New York, 1984.
32. Zhdanov, G.S., *Crystal Physics*, Oliver & Boyd, Edinburgh, 1965.
33. Main, J. A., Garcia, E., Newton, D. V., "Precision Position Control of Piezoelectric Actuators Using Charge Feedback," *SPIE* Vol. 2441 San Diego, CA, 1995, pp. 243-254.
34. Ramo, Whinnery, and Van Duzer, *Fields and waves in Communication Electronics*, 1965 John Wiley & Sons, Inc., New York.
35. Wilkie, K., Turner, T.L, Mei, C., personal meeting, NASA Langley Research Center Aeroelasticity Branch, Hampton, VA.
36. Bent, A.A., "Active Fiber Composites for Structural Actuation," Ph.D. Dissertation, Department of Aeronautics and Astronautics, Massachusetts Institute of Technology, Cambridge, MA 1997.

37. Janos, B. Z., Hagood, N. W., "Magnetic Particle Doping for Anisotropic Matrix Materials in Active Fiber Composites," *SPIE Smart Structures and Materials*, 1999, Paper 3675-02.
38. *ANSI/IEEE Std. 176-1987*, The Institute of Electrical and Electronic Engineers, New York, 1988.
39. Gibson, R. F., *Principles of Composite Material Mechanics*, McGraw-Hill, Inc., New York, 1994, p. 50.
40. Tessler, A., A C^0 Anisoparametric Three-Node Shallow Shell Element, *Computer Methods in Applied Mechanics And Engineering*, 78 1990, pp. 89-103.
41. Tessler, A., Hughes, T. J. R., "A Three-Node Mindlin Plate Element With Improved Transverse Shear," *Computer Methods in Applied Mechanics And Engineering*, 50, 1985, pp. 71-101.
42. Chen, R. R., "Finite Element Nonlinear Random Response of Composite Panels of Arbitrary Shape to Acoustic and Thermal Loads Applied Simultaneously," Ph.D. Dissertation, Department of Aerospace Engineering, Old Dominion University, Norfolk, VA, 1995.
43. Eer Nisse, E. P., "Variational Method for Electrostatic Vibration Analysis", *IEEE Transactions On Sonics and Ultrasonics*, Vol. SbarutU-14, No. 4, October 1967, pp. 153-160.
44. Dosch, J. J., Inman, D. J., Garcia, E., "A Self-Sensing Piezoelectric Actuator for Collocated Control", *J. of Intell. Mater. Syst. And Struct.*, Vol. 3, Jan. 1992, pp. 166-185.
45. Cole, D. G., Clark, R. L., "Adaptive Compensation of Piezoelectric Sensoriactuators", *AIAA J.*, Vol. 34, No. 10, October 1996, pp. 2102-2109.
46. Leissa, A. W., *Vibration of Shells*, NASA SP-288; Reprinted by the Acoustical Society of America, American Institute of Physics, NY, 1993.
47. Wilkie, W. K., NASA Langley Research Center Aeroelasticity Branch, e-mail September 9, 1999.
48. Cunefare, K. A., "The Minimum Multimodal Radiation Efficiency of Baffled Finite Beams," *J. Acoust. Soc. Am.*, 90 (5) 1991, pp. 2521-1580.
49. Elliott, S. J., Johnson, M. E., "Radiation Modes and the Active Control of Sound Power," *J. Acoust. Soc. Am.*, 94 (4) , October 1993, pp. 2194-2204.

50. Pierce, A. D., *Acoustics*, Acoustic Society of America, New York, NY, 1991.
51. Fahy, F., *Sound and Structural Vibration*, Academic Press, San Diego, CA, 1985.
52. Lomas, N. S., Hayek, S. I., "Vibration and Acoustic Radiation of Elastically Supported Rectangular Plates," *J. of Sound and Vibration*, 52 (1), 1977, pp. 1-25.
53. Koopmann, G. H., Benner, H., "Method for Computing the Sound Power of Machines Based on The Helmholtz Integral," *J. Acoust. Soc. Am.*, 71 (1), January 1982, pp. 78-89.
54. Junger, M. C., Feit, D., *Sound, Structure and Their Interaction*, The MIT Press, Cambridge, MA, 1986.
55. Currey, M. N., Cunefare, K. A., "The Radiation Modes of Baffled Finite Plates," *J. Acoust. Soc. Am.*, 98 (3), September 1995, pp. 1570-1580.
56. Currey, M. N., Cunefare, K. A., Johnson, M. E., Elliott, S. J., "Radiating Efficiency Grouping of Acoustic Radiation Modes. Part I, Theory and Validation," *J. Acoust. Soc. Am.* 100 (4) pt. 2, October 1996, p. 2597.
57. Flexible Intelligence Group, *Soft Computing Techniques*, FT3PAK Version 1.0, Tuscaloosa, AL, 1997.
58. Cabell, R. H., General Predictive Control for Turbulent Boundary Layer Noise Software, Personal Meetings, NASA Langley research Center, Structural Acoustics Branch, Hampton, VA, March 2000.
59. Juang, J. N., Eure, K. W., "Predictive Feedback and Feedforward Control for Systems with Unknown Disturbances," NASA/TM-1998-208744, Langley Research Center, Hampton, VA, Dec. 1998.
60. Juang, J. N., *Applied System Identification*, PTR Prentice Hall, Englewood Cliffs, New Jersey, 1994, pp. 198-199.
61. Morgan-Matroc, Inc., *Product Catalog*, Electro-Ceramics Division, Bedford, Ohio, 1993.
62. Clark, R. L., Saunders, W. R., Gibbs, G. P., *Adaptive Structures, Dynamics and Control*, John Wiley and Sons, New York, 1998, p. 350.

APPENDIX A

MFC Structural Acoustic Simulation

Introduction

The following data is presented to further characterize MFC actuator performance as compared to traditional PZT actuators. The data presented in Chapter III clearly demonstrates that MFC actuators can produce results different than that of traditional PZT actuators. However, the transfer function between the actuator and a single nodal velocity output does not provide sufficient information to accurately quantify MFC actuator performance. Specifically, additional information is required to fairly evaluate MFC actuator performance regarding active structural acoustic control. To this end, the following acoustic simulations are provided for curved and flat panels utilizing surface bonded MFC and traditional actuators.

Curved Panel Simulation

The simulation is performed using an aluminum 10"x14"x0.040" curved panel with radius of curvature $R=96''$ and a 2"x4"x0.010" actuator located at the panel center. The actuator is modeled first using MFC properties and then repeated using traditional PZT properties for comparison. The triangular finite element mesh of 144 elements shown in Figure 3.5 is used. The simulations follow the procedure outlined for flat panels subjected to a random acoustic disturbance presented in Chapter VI. However, the radiated sound power is determined by implementing radiation filters for curved panels as described in Chapter IV. The radiation filter is based on the radiation modal expansion technique using fifteen discrete acoustic radiators. The fifteen elemental acoustic

radiators are selected to correspond to the measured acceleration points used during the experimental investigation of flat panels.

The simulation performed considers actuator orientation angles of 20, 35, 45, 50, 60, and 70 degrees. The acoustic disturbance used has an overall sound power level of 92 dB and is depicted in Figure 6.13. The actuator performance is determined by considering the reduction in radiated sound power between the open and closed loop conditions as described in Chapter VI.

MFC and PZT results for 20-degree orientation angle are shown in Figures A.1 and A.2, respectively. An overall attenuation of 14.48 dB is achieved for the MFC actuator and the PZT actuator achieves 16.72 dB.

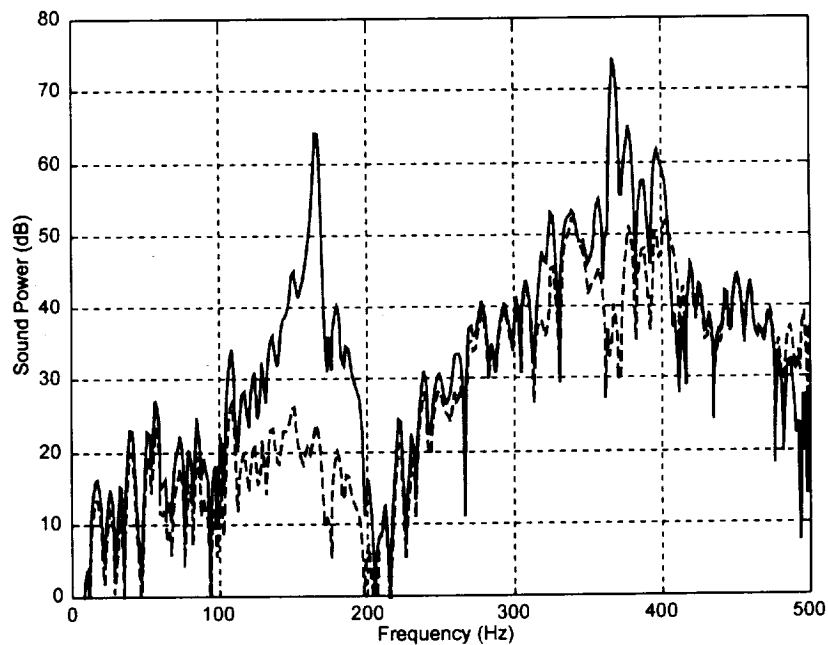


Figure A.1 Predicted Open and Closed Loop Radiated Power for 20° MFC

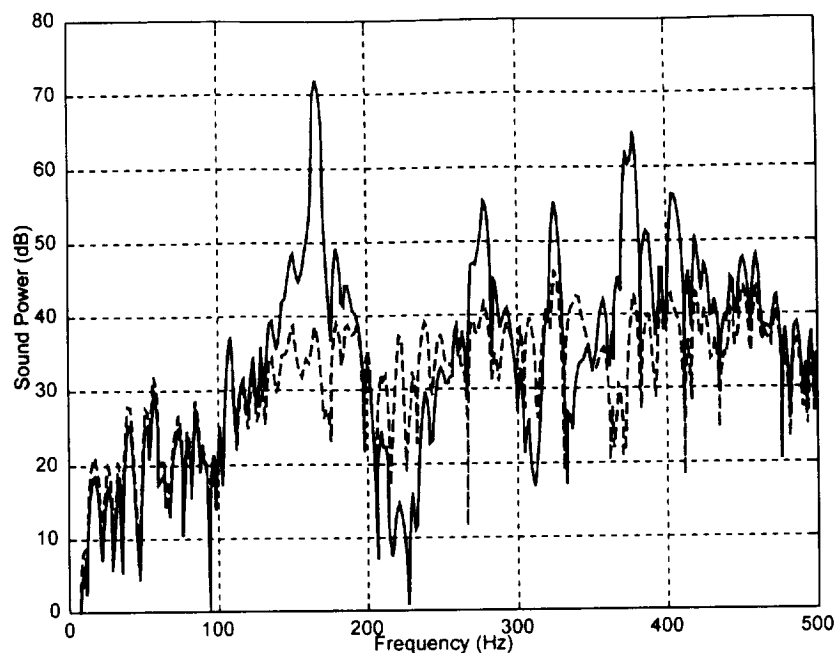


Figure A.2 Predicted Open and Closed Loop Radiated Power for 20° PZT

MFC and PZT results for 35-degree orientation angle are shown in Figures A.3 and A.4, respectively. An overall attenuation of 14.72 dB is achieved for the MFC actuator and the PZT actuator achieves 23.98 dB.

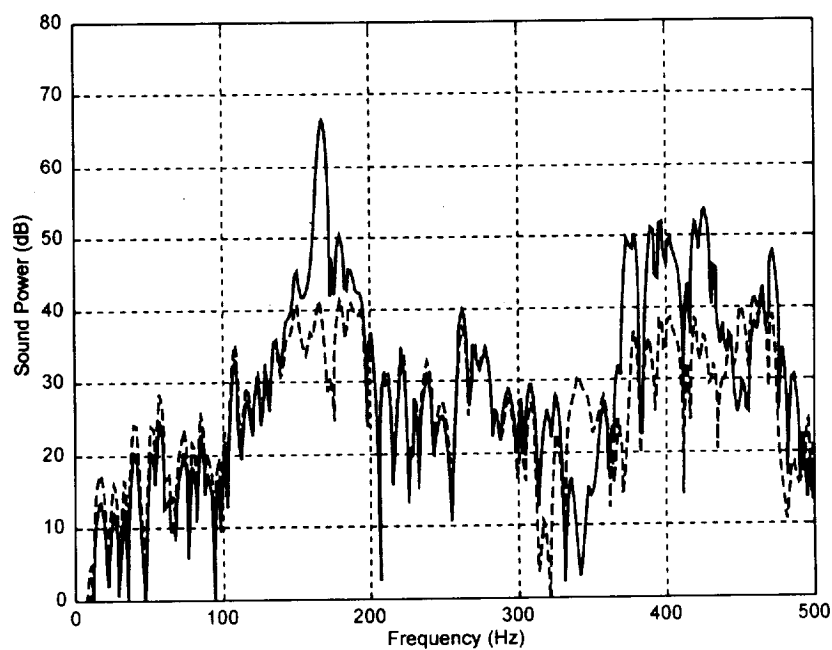


Figure A.3 Predicted Open and Closed Loop Radiated Power for 35° MFC

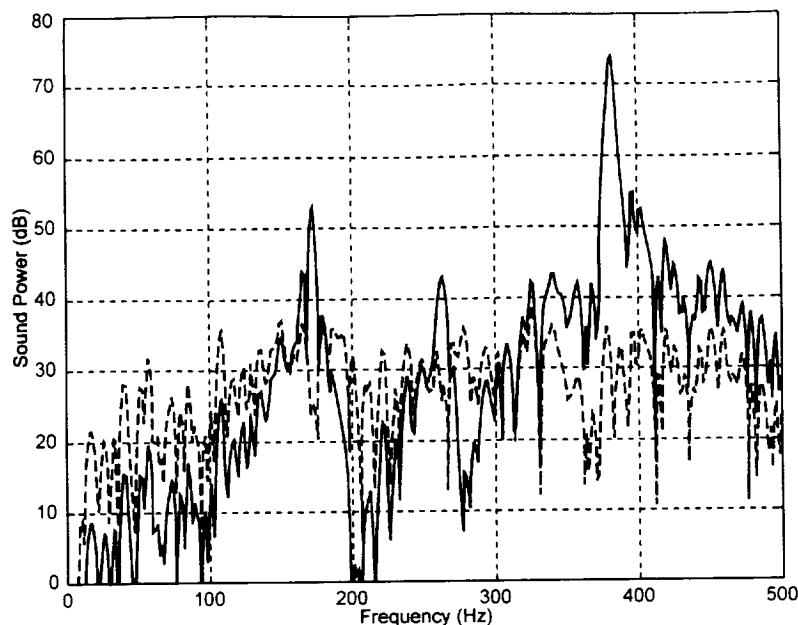


Figure A.4 Predicted Open and Closed Loop Radiated Power for 35° PZT

MFC and PZT results for 45-degree orientation angle are shown in Figures A.5 and A.6, respectively. An overall attenuation of 3.92 dB is achieved for the MFC actuator and the PZT actuator achieves 19.27 dB.

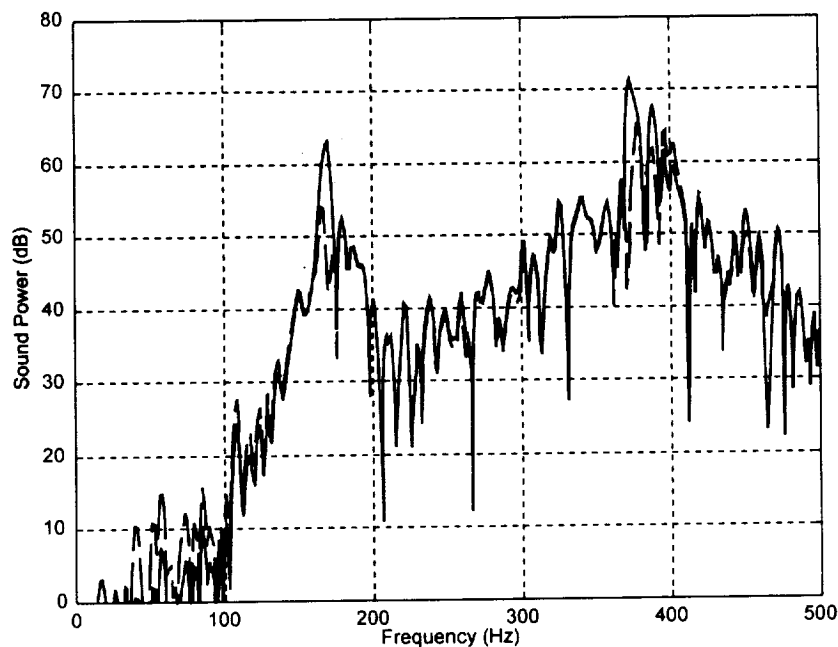


Figure A.5 Predicted Open and Closed Loop Radiated Power for 45° MFC

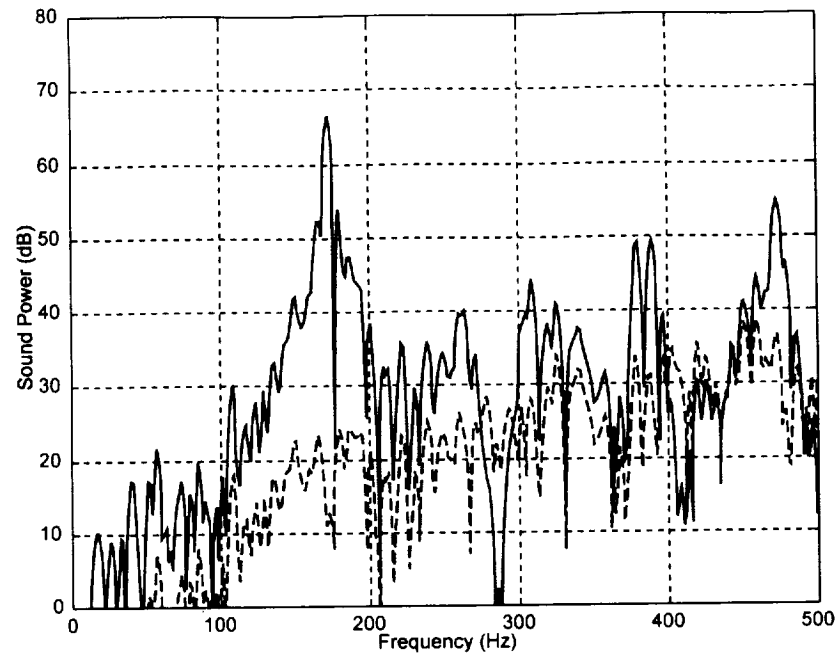


Figure A.6 Predicted Open and Closed Loop Radiated Power for 45° PZT

MFC and PZT results for 50-degree orientation angle are shown in Figures A.7 and A.8, respectively. An overall attenuation of 9.94 dB is achieved for the MFC actuator and the PZT actuator achieves 17.78 dB.

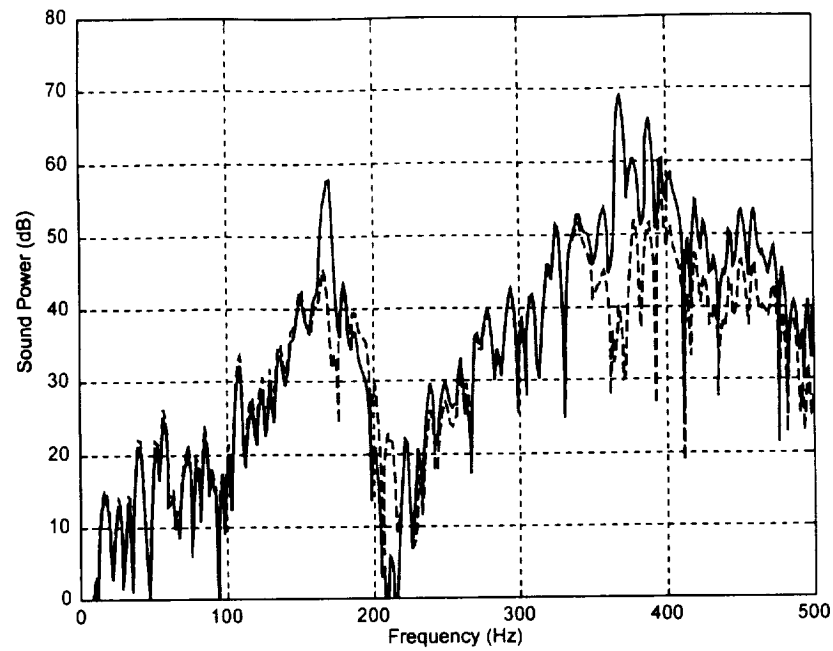


Figure A.7 Predicted Open and Closed Loop Radiated Power for 50° MFC

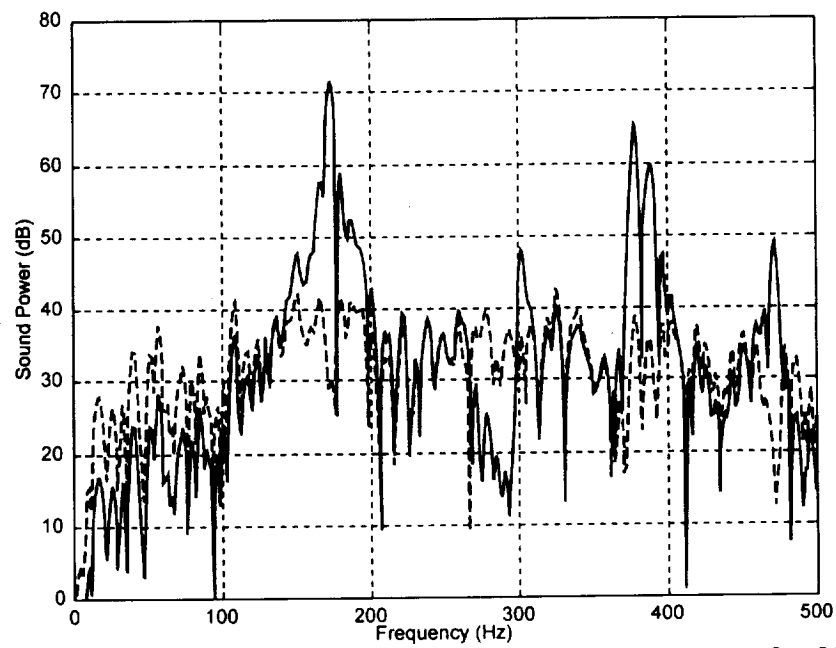


Figure A.8 Predicted Open and Closed Loop Radiated Power for 50° PZT

MFC and PZT results for 60-degree orientation angle are shown in Figures A.9 and A.10, respectively. An overall attenuation of 12.83 dB is achieved for the MFC actuator and the PZT actuator achieves 16.64 dB.

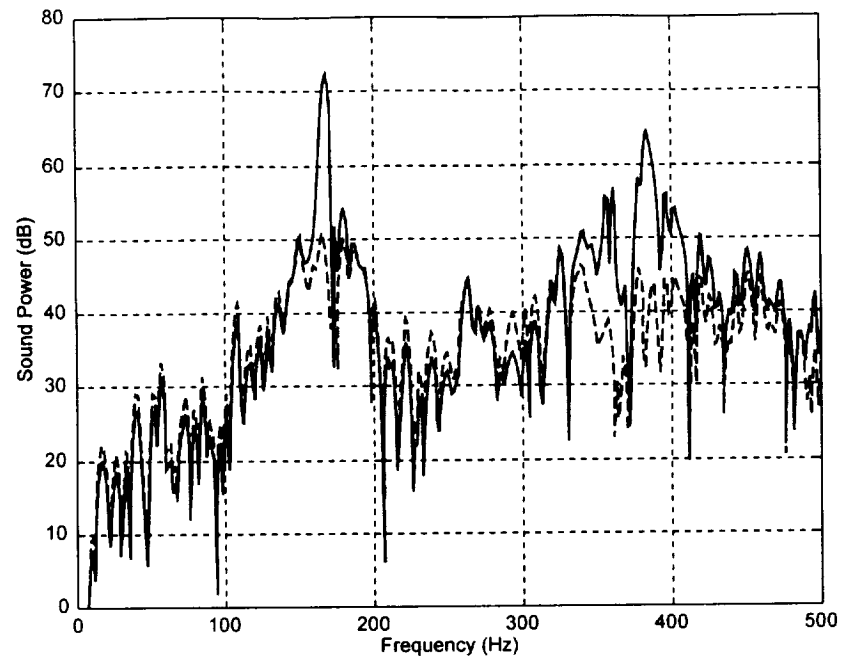


Figure A.9 Predicted Open and Closed Loop Radiated Power for 60° MFC

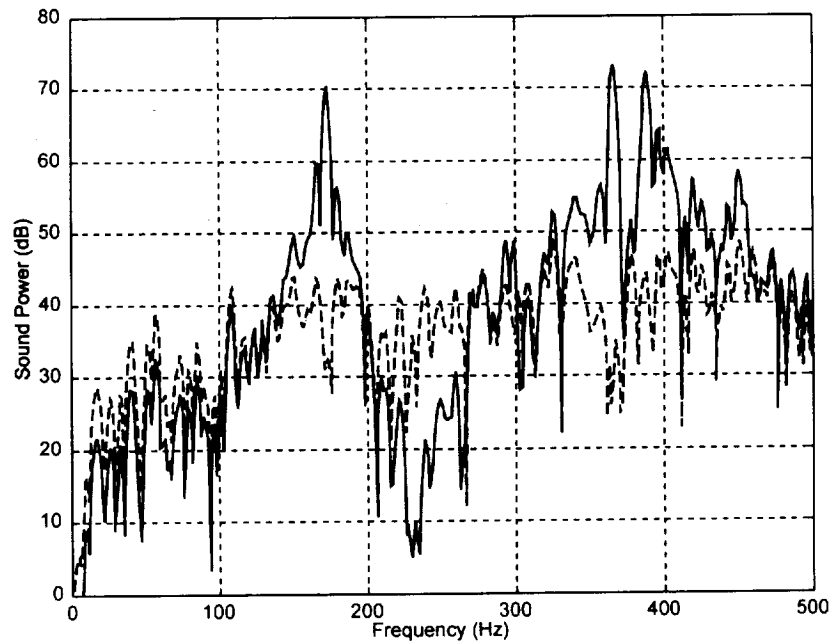


Figure A.10 Predicted Open and Closed Loop Radiated Power for 60° PZT

MFC and PZT results for 70-degree orientation angle are shown in Figures A.11 and A.12, respectively. An overall attenuation of 4.79 dB is achieved for the MFC actuator and the PZT actuator achieves 23.21 dB.

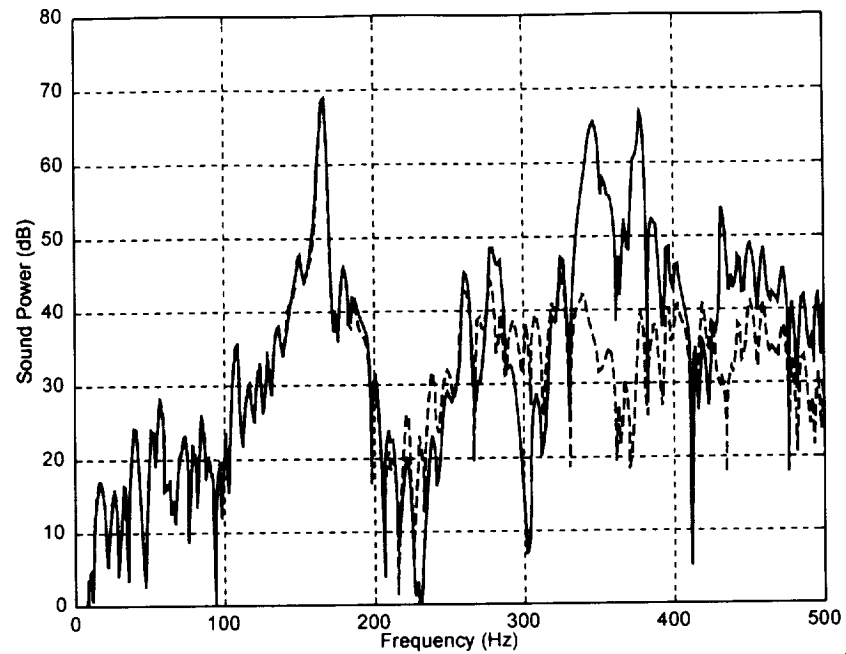


Figure A.11 Predicted Open and Closed Loop Radiated Power for 70° MFC

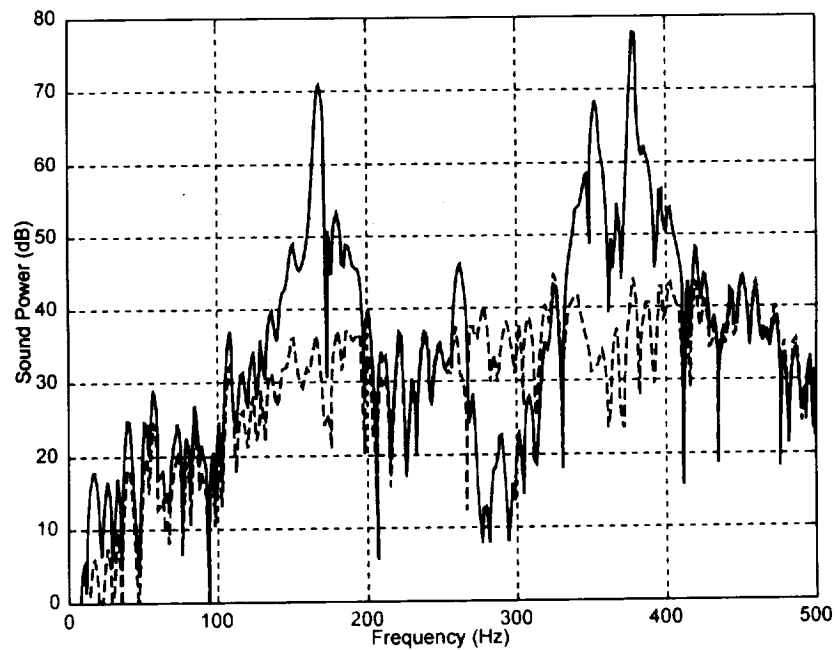


Figure A.12 Predicted Open and Closed Loop Radiated Power for 70° PZT

The simulation data indicates that the MFC actuator does not perform as well as a traditional PZT actuator. Keep in mind, however, that traditional PZT may not be suitable for skewed angle placement on curved panels. Furthermore, when considering active structural noise control a single actuator located at the panel center and skewed is not expected to perform well. To rigorously evaluate MFC actuator performance the finite element model should be modified to facilitate arbitrary actuator placement including orientation angles of $\pm 90^\circ$. Initially, the research objectives were aimed at addressing this concern; however, piezoceramic actuator placement on flat panels became the primary objective of the funding agent. However, to further evaluate MFC performance the finite element model utilized in Chapter VI is modified to incorporate MFC actuators. Since the finite element model utilizes rectangular elements, the MFC orientation angles are limited to $\pm 90^\circ$. Furthermore, the rectangular plate elements do not facilitate curved panel structures.

Flat Panel Simulation

The finite element analysis used to simulate MFC structural acoustic control utilizes a modified rectangular high precision plate element with 24 nodal DOF with an electrical DOF. The finite element model is modified to incorporate MFC actuator electrical and mechanical properties. The simulations are repeated using traditional PZT actuators. The simulation is conducted using the flat panels in Chapter VI referred to as “B” and “revised optimum.” For clarity, the “revised optimum” panel is referred to as panel E. The simulation is identical to the procedure described in Chapter VI for flat

panels. The MFC orientation for panels B and E are depicted in Figures A.13 and A.14, respectively.

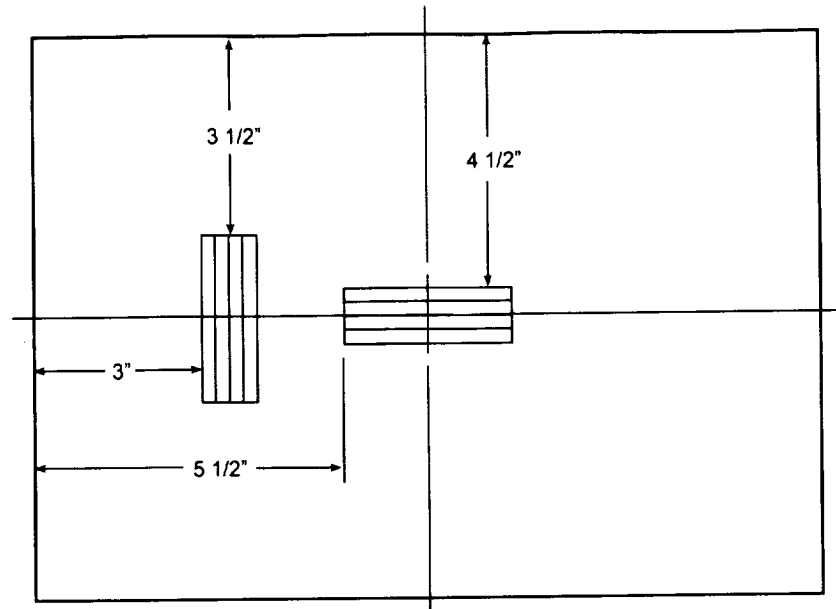


Figure A.13 Panel B MFC Orientation

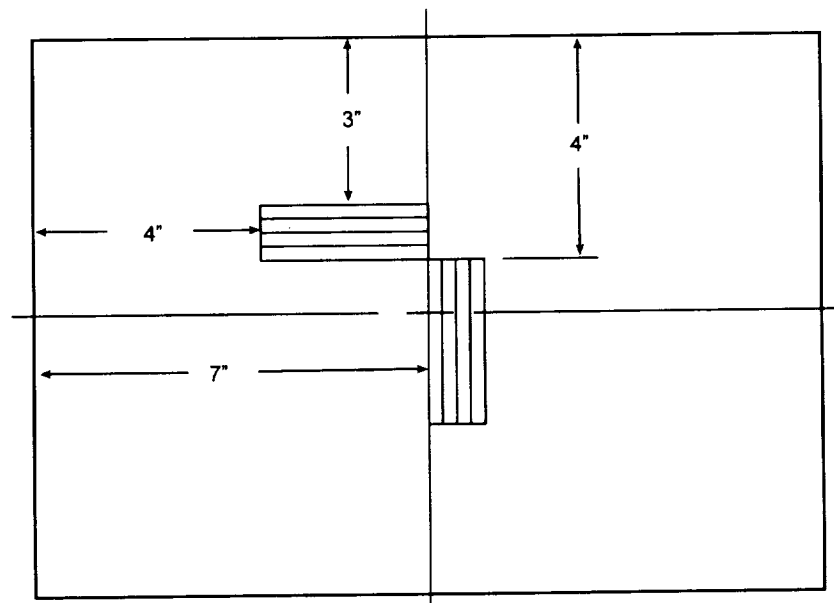


Figure A.14 Panel E MFC Orientation

The open and closed loop sound power for panel B with MFC actuators is shown in Figure A.15. The overall sound power attenuation is 3.96 dB for panel B with MFC. However, the overall sound power attenuation is 3.36 dB for panel B with PZT and is shown in Figure A.16.

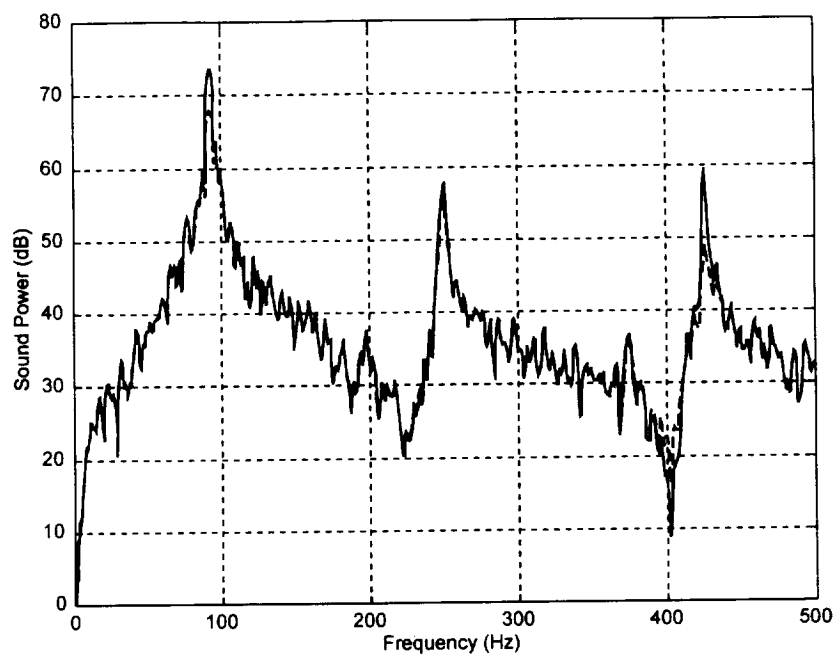


Figure A.15 Open and Closed Loop Sound Power of Panel B with MFC

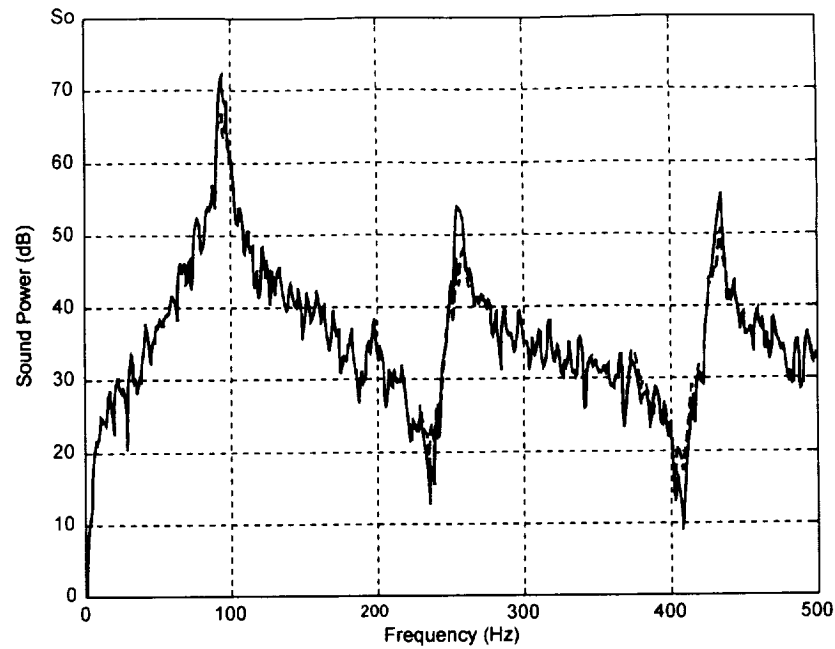


Figure A.16 Open and Closed Loop Sound Power of Panel B with PZT

The open and closed loop sound power for panel E with MFC actuators is shown in Figure A.17. The overall sound power attenuation is 4.68 dB for panel E with MFC. However, the overall sound power attenuation is 4.62 dB for panel E with PZT and is shown in Figure A.18.

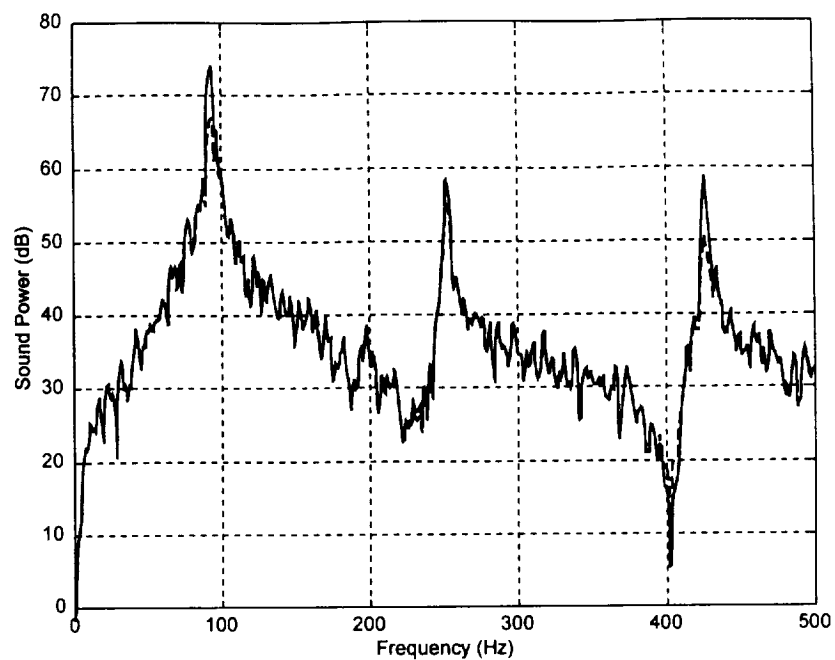


Figure A.17 Open and Closed Loop Sound Power of Panel E with MFC

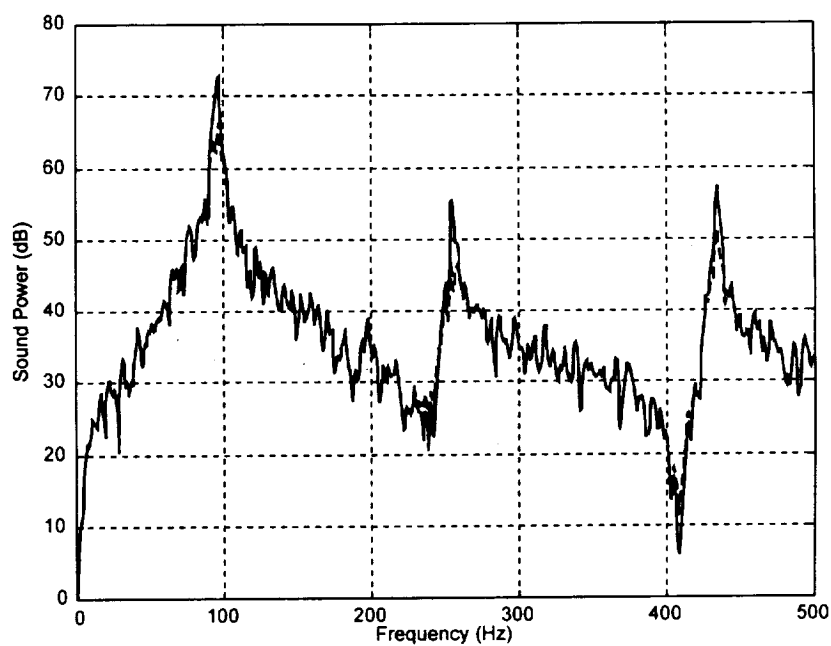


Figure A.18 Open and Closed Loop Sound Power of Panel E with PZT

For flat rectangular panels the two MFC actuators perform slightly better than traditional PZT actuators for structural acoustic noise control. However, a single MFC actuator does not perform as well as the traditional PZT actuator for curved panels. The MFC actuator concept provides increased control authority along one of its principal directions. Therefore, it is anticipated that the MFC actuator concept is best suited for structures requiring induced strains along a particular direction. The simulations provided do not explicitly address structures of this nature. It is recommended that future research address multiple MFC actuators for structural acoustic control of curved panels.

APPENDIX B

Test Instrumentation

PCB Accelerometers Model U352C65

Table B.1 Accelerometer List

Channel	Serial Number
1	19175
2	20027
3	15683
4	20620
5	19215
6	15865
7	15823
8	17876
9	18981
10	19132
11	18711
12	19138
13	19139
14	19134
15	19148

Modal Shop Microphones Model TMS E130P11

Modal Shop Microphone Preamplifier Model TMS 130A10

Table B.2 Microphone List

Channel	Microphone s/n	Preamp s/n
1	5206	5309
2	5220	5294
3	5904	5332
4	5214	5331
5	5217	5312
6	2752	5274

Accelerometer Amplifier

PCB Model 481A s/n 261

Microphone Amplifier

PCB Model 583A s/n 898

Piezoelectric Actuator Amplifier

PCB/AVC Model 790A01 s/n 238

PCB/AVC Model 790A01 s/n 239

Loudspeaker

Altec Lansing Model 817A s/n 01549

Audio Power Amplifier

Carver Model TFM 42 s/n 91810500007

Audio Equalizer

Technics Model SH-8065 s/n mb5402b025

Accelerometer Calibrator

PCB Model 394C06 s/n 1856

B&K Signal Analyzer Model 2032 s/n 1123814